A HI Search for Galaxies Hidden by the Galactic Bulge

Nebiha Bedru Shafi

University of Cape Town
Department of Astronomy

Thesis submitted in partial fulfilment of the requirements for the degree M.Sc. in the Department of Astronomy
as part of the National Astrophysics and Space Science Program
University of Cape Town

February 2008

Abstract

In this thesis, a deep neutral hydrogen (HI) galaxy search for galaxies hidden by the Galactic Bulge is presented. The HI Parkes deep HI Zone of Avoidance (ZOA) survey has been extended towards higher latitudes in the Galactic Bulge region. The surveyed region covers $332° \leq l \leq 36°$ for the region $5° \leq |b| \leq 10°$ and $352° \leq l \leq 24°$ for the region $10° \leq |b| \leq 15°$. Visual inspection of the HI data in the form of three-dimensional data cubes revealed 158 galaxies. The HI parameters of the galaxies were determined using MBSPECT task in the MIRIAD (Sault et al., 1995). Of the 158 galaxies only 65 have previously catalogued multiwavelength counterparts (mostly NIR, optical or HIPASS), the majority of which matched to a single counterpart. The distribution of the detected galaxies on the sky and redshift space are analyzed. A closer inspection of the newly detected galaxies allow identification of new large-scale structures connected with the Great Attractor Wall. These galaxies also provide an improved outline of the Local Void (Tully & Fisher, 1987). The Local Void is seen as an underdense region out to $cz \lesssim 6000$ km s^{-1} extending from $l \sim 345°$ to $45°$ and $b \sim -30°$ to $+45°$. With the newly detected galaxies and previously catalogued galaxies, a new "second parallel arm" to the Norma supercluster (Woudt et.al, 1997) is identified for first time in this HI survey. This "second parallel arm" seems to stretch from the Centaurus cluster Abell 3526 at $(l, b = 32°, +22°)$ down to higher longitudes, crossing the Galactic Plane at $l \sim 345°$ and $cz \sim 4500$ km s^{-1}. We also identified a possible connection between the Norma supercluster and the Ophiuchus cluster (Wakamatsu & Melkan, 1981).

Acknowledgments

I would like to express my deep and sincere gratitude to my supervisor, Professor Renèe Kraan-Korteweg for her supervision and patient guidance. I have greatly benefited from ideas generously lavished on the course of this thesis work. I greatfully acknowledge Professor Lister-Staveley Smith at the University of Western Australia for his generous assistance during HI parametrization. I would like to thank Dr. Kurt van der Heyden for his comments and suggestions for the editing of my thesis. It is a pleasure to acknowledge the encouragement from all the people in the Department of Astronomy. I specially thank Bonita for her invaluable advice and help whenever she could. My thanks go to my office-mates, Ewald and James for being willing to help and sharing knowledge. I also like to thank Paul for his help during observation with IRSF.

I take this opportunity to express my special and profound gratitude to Abdi for being there for me throughout the difficult time. I am grateful to have a person as special as you in my life.

Finally I would like to acknowledge the National Astrophysics and Space Science Program (NASSP) and National Research Foundation (NRF) for funding and supporting this work.

Contents

List of Figures

List of Tables

Chapter 1

Introduction

1.1 The Zone of Avoidance

Optical and near infrared galaxy surveys fail to detect galaxies close to the Galactic Equator and around the Galactic Bulge because of high extinction and star density. This area of incompleteness is known as the "Zone of Avoidance" (ZOA): galaxies seem to avoid this region. It was first named as such by Richard Proctor in 1878 when referring to the distribution of "nebulae" in Sir John Herschel's General Catalog of Nebulae (Herschel, 1864). Edwin Hubble, however, was the first to correctly explain the ZOA as being caused by the light-absorbing dust particles that are distributed throughout the plane of the Milky Way (Hubble, 1936).

Our own Galaxy is a major obstacle in probing the extragalactic Universe: it blocks more than 20% of the optical and about 10% of the infrared sky (see Kraan-Korteweg & Lahav, 2000, for a detailed discussion). The dust in the plane of the Milky Way obscures our view of the extragalactic sky due to absorption of light. In addition, due to increasing stellar crowding, foreground stars cause confusion in the identification of background galaxies close to the plane of the Galaxy. This creates a ZOA which flares up around the Galactic Bulge from about Galactic latitudes of $|b| = 5°$ up to $|b| = 20°$. Although deep optical and infrared surveys partly penetrate this obscured region and allow the identification of some of the galaxies, high extinction in the optical and stellar concentration in the infrared, make the surveys increasingly incomplete.

1.2 Importance of Mapping the Hidden Matter in the ZOA

One of the main objectives of galaxy redshift surveys is to map how luminous matter, observed in the form of galaxies and cluster of galaxies, is distributed in space. Quantifying the three-dimensional distribution of galaxies is important to understand the evolution of galaxies and their environment, to determine the fundamental parameters of cosmology and to understand the past and future histories of the Universe at large scales. Studies of the large-scale distribution of galaxies before the 1970s were limited in resolving the true nature of the Universe due to lack of deep systematic surveys. The development of sensitive detectors and spectrometers at radio, near infrared and optical wavelengths in 1980s made the deeper three dimensional view of galaxy distribution possible. Since then these deep galaxy

redshift surveys have revealed the complex web-like structure of the Universe: galaxies are not distributed randomly in space, but tend to lie in clusters and superclusters linked by filaments surrounding voids (Fairall, 1998).

Moreover, the Milky Way and its neighbouring galaxies (the Local Group) exhibit a peculiar motion with respect to the Cosmic Microwave Background radiation (CMB; Kogut et al., 1993). The irregular distribution of mass surrounding the Local Group (LG) induces peculiar velocity on the LG which is observed as a dipole effect in the CMB. Searching for the convergence of the dipole with distance has also been a critical problem. Analysis of this effect is complicated by a streaming motion toward the "Great Attractor" (GA)–a huge mass overdensity in the direction of Norma supercluster. This streaming motion was detected from the systematic infall pattern of 400 early-type galaxies within $40h^{-1}$ Mpc (Dressler et al., 1987). In addition, it has been suggested that this systematic flow pattern might be influenced by the more distant and massive Shapley Concentration, which is centered on Abell 3558 ($l, b, v = 312°, 31°$, 14 500 km s^{-1}) (Raychaudhury, 1989; Hundson et al., 2004).

In order to understand these complex dynamics it is essential to quantify the distribution of galaxies in the local Universe. However, the incompleteness in the distribution of galaxies close to the Galactic Plane constrains the study of large-scale structures in the nearby Universe and the determination of the peculiar motion of the LG and in the GA. The ZOA has hindered our progress in understanding cosmological issues, such as:

- Determining the true size and extent of nearby large-scale structures. This is difficult because several nearby superclusters are bisected by the Milky Way. For instance, the Local Supercluster, the Perseus-Pisces chain (Chamaraux et al., 1990), the Centaurus Wall (Lahav, 1994) and the Hydra-Antlia filament (Kraan-Korteweg et al., 1994a).

- Measurements of the CMB dipole imply a LG velocity of $V = 622$ km s^{-1} toward the direction of $l = 277°$, $b = 30°$ (Kogut et al., 1996; Bennett et al., 2003). Although this measurement is known to high accuracy, the source of the motion has yet to be absolutely ascertained. According to linear perturbation theory, the LG's peculiar velocity is caused by the surrounding mass inhomogeneities. However, there has been a debate on whether it is a large-scale bulk flow induced by more distant structures, or whether the LG is accelerated by nearby massive structures hidden in the ZOA (Kocevski & Ebeling, 2006).

- A large fraction of the GA lies behind the Milky Way (Woudt, 1998). The precise mass, position and extent of the observed systematic flow of galaxies in this region still remain uncertain. Lynden-Bell et al. (1988) originally estimated the mass of the GA about 5×10^{16} M$_\odot$ with a central peak around $(l, b, v) \sim (307°, +9°, 4350 \pm 350$ km s$^{-1})$. A later study however placed the center of the GA at $(l, b, v) \sim (320°, 0°, 4500$ km s$^{-1})$ (Kolatt et al., 1996). More recently Tonry et al. (2000) determined the core to be located even closer at (289°, +22°, 3200 ± 260 km s^{-1}) with a lower mass of about 8×10^{15} M$_\odot$. Even with the more recent discoveries of clusters in the GA region such as the Norma cluster (Abell 3627; Kraan-Korteweg et al., 1996) and the Centaurus-Crux or CIZA J1324.7-5736 clusters (Woudt, 1998; Ebeling et al., 2002), there is still

disagreement between the observed mass density and the mass originally proposed by Lynden-Bell et al. (1988) (Kocevski & Ebeling, 2006). By observing the distribution of galaxies in this region, fundamental cosmological density parameters such as Ω_o can be constrained (Kraan-Korteweg & Lahav, 2000).

In order to solve these problems several groups have initiated various systematic observing programmes using different methods to uncover the galaxies and their distribution hidden in the ZOA. A brief review of these observational surveys that have been carried out in different wavelengths will be discussed in the next section giving more emphasis on HI surveys, the main interest of this thesis work.

1.3 Multi Wavelengths Surveys of the ZOA

1.3.1 Optical Surveys

In the last two decades systematic deep optical galaxy surveys in the ZOA have uncovered tens of thousands of galaxies that led to identification of various large-scale structures (e.g. Kraan-Korteweg, 2000; Weinberger et al., 1999; Roman et al., 1998; Wakamatsu et al., 1994). These surveys are not biased toward any particular morphological type and achieved a considerable reduction of the ZOA. However, the Galaxy remains opaque at low Galactic latitudes in regions where the optical extinction exceeds 4–5 magnitudes (Kraan-Korteweg & Woudt, 1999). Figure 1.1 (taken from Kraan-Korteweg & Lahav, 2000) shows an Aitoff projection of optically catalogued galaxies (a complete sample) in Galactic coordinates. The ZOA is seen as a broad band void of galaxies.

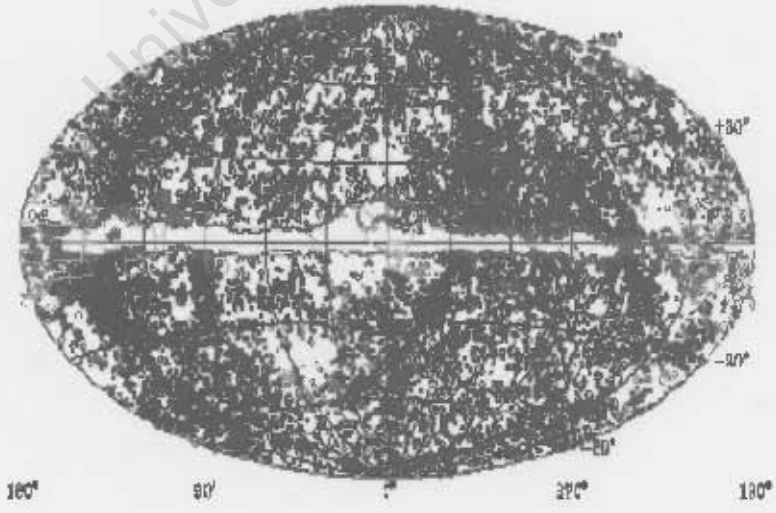

Figure 1.1: Aitoff projection of optical galaxies with extinction-corrected diameter $D^o \geq 1'.3$ in Galactic coordinates. The galaxies are diameter coded. DIRBE extinction contours of $A_B \leq 3^{\rm mag}$ (Schlegel et al., 1998) is superimposed on the distribution. Figure from Kraan-Korteweg & Lahav (2000).

1.3.2 Far Infrared

Surveys in the Far Infrared (FIR) are hardly affected by dust extinction. The Infrared Astronomical Satellite (IRAS) survey has produced a catalog of 250 000 point sources, the IRAS Point Source Catalogue (IRAS PSC; Joint IRAS Science Working Group 1988). The IRAS PSC has been used to identify galaxies behind the Milky Way by following strict criteria based on the relation of fluxes in the different FIR IRAS bands. With the advantage of uniform sky coverage, though dominated by spiral and starburst galaxies, redshift follow-ups for a well-defined sample of galaxies in the ZOA spotted connections of large-scale structures across the ZOA (Takata et al., 1996) including most of the structures discovered by systematic optical surveys. However, cirrus, high source counts of Galactic objects and confusion with these sources made the search incomplete at low Galactic latitudes.

Despite these problems, various near-all-sky ($|b| \geq 5°$) redshift surveys, complete to given flux limits, have been carried out to trace large-scale structure. For instance, the IRAS 1.9 Jy Survey (Strauss et al., 1992) followed by the later extension to a lower, 1.2 Jy flux limit (Fisher et al., 1995) and the deeper PSCz survey complete down to 0.6 Jy (Strauss et al., 2000b) are the major ones. The latter survey was extended to lower latitudes 'Behind The Plane' (BTP) survey (light-gray area of Fig. 1.2). The PSCz survey with BTP has reduced the "IRAS ZOA" significantly. Figure 1.2 (from Saunders et al., 2000a) shows the resulting sky map. The galaxy distribution is still incomplete towards the Galactic Center.

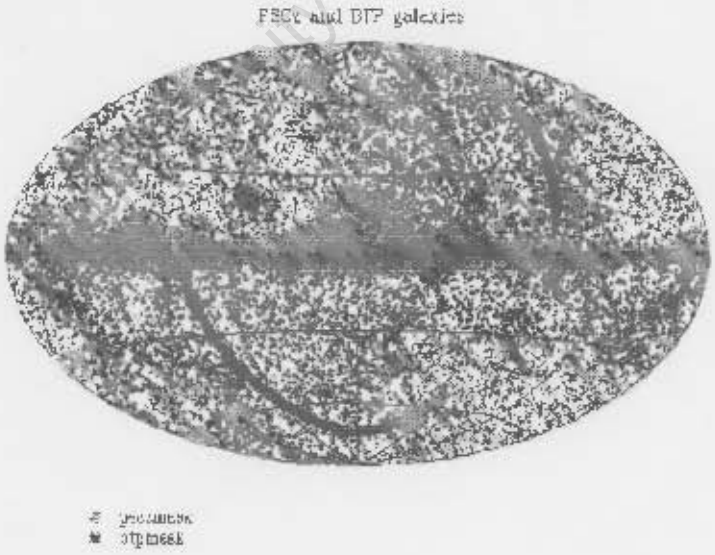

Figure 1.2: The PSCz and BTP IRAS galaxy distribution centred on the Milky Way. The PSCz and BTP incompleteness masks are represented by dark-gray and light-gray respectively. The reduction of incompleteness around the Galactic Equator due to BTP is clearly visible. Figure from (from Saunders et al., 2000a).

1.3.3 Near Infrared

Surveys in the Near Infrared (NIR) have given us a more complete image of the extragalactic sky. In the NIR, confusion with Galactic objects is lower compared to the FIR surveys. NIR surveys have been efficient in revealing galaxies at extinction levels where deep optical searches become increasingly incomplete. This is because the dust extinction is considerably lower in the NIR than in the optical, with the I, J, H and K band extinction being 45%, 21%, 14% and 9% of the optical B band (Schröder et al., 1997). In addition, they are sensitive to early-type galaxies which are missed in IRAS.

Two major systematic NIR surveys: the DEep Near Infrared Southern Sky Survey (DENIS) (Epchtein, 1997) and the 2 Micron All Sky Survey (2MASS) (Jarrett et al., 2000a,b) have been carried out. The 2MASS survey produced the Extended Sources Catalog (2MASX). It contains 1.65 million galaxies (extended sources) in addition to a Point Source Catalog (PSC) containing about 0.5 billion Milky Way stars. Mapping large-scale structures across the ZOA is now possible with the 2MASX (e.g. Jarrett, 2004). Even though NIR surveys can identify galaxies to high extinction levels over $A_B \gtrsim 10^{\rm m}$, Kraan-Korteweg & Jarrett (2005) showed that the Galactic Bulge region, due to high stellar concentration, continues to hide a major part of the extragalactic sky, the so-called "NIR ZOA". They actually found that in this region optical surveys probe the galaxy distribution deeper into the plane than the 2MASX. Figure 1.3 (from Jarrett, 2004) shows an all-sky map of the galaxy distribution color-coded by redshift, (see this paper for a detailed description). The lack of galaxies and large-scale structures close to the Galactic Bulge is clearly visible.

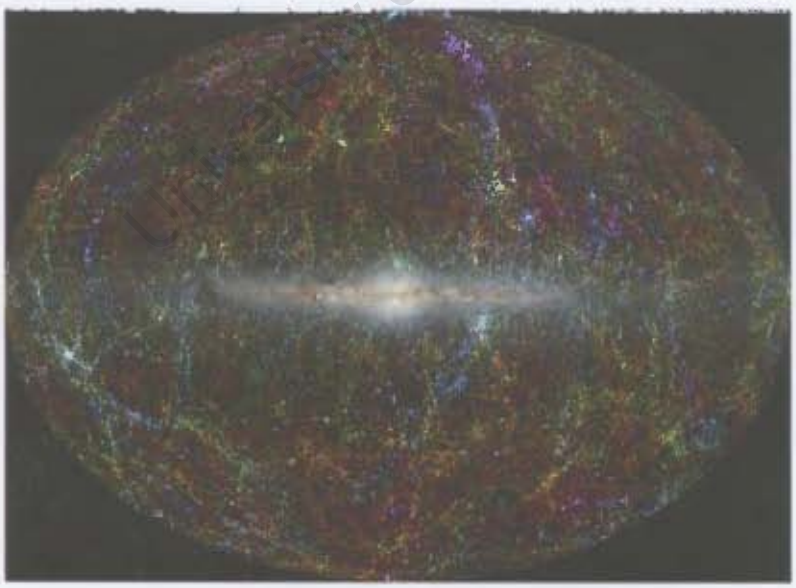

Figure 1.3: An all-sky Aitoff projection of 2MASX sources with $K < 14^{\rm m}$ in Galactic coordinates centered on the Galactic Bulge. The image also includes stars from 2MASS PSC. Figure from Jarrett 2004.

1.3.4 X-ray Surveys

At this wavelength, dust extinction and stellar confusion are not a problem. The Milky Way is transparent to the hard X-ray emission, above 0.5–2.0 keV. As rich clusters are strong X-ray emitters, X-ray surveys provide the best means to search for cluster of galaxies at low Galactic latitude. The X-ray selected cluster surveys such as, the Brightest Cluster Sample (BCS; Ebeling et al., 2000) and the ROSAT (Böhringer et al., 2001) covered most of the extragalactic sky but, both surveys were limited to higher Galactic latitudes, $|b| \sim 20°$. The "Clusters In the Zone of Avoidance" project (CIZA; Ebeling et al., 2002) was the first systematic X-ray search for galaxy clusters behind the Galactic Plane. This project discovered several X-ray clusters at low Galactic latitudes. The previously mentioned CIZA J1324.5-5736, located in the GA region, is among the newly discovered clusters. Despite the fact that an X-ray search for clusters overcomes the problem posed by optical searches, photoelectric absorption by the Galactic hydrogen atoms limits detections close to the Galactic Plane, where the absorbing column density; $N_H \geq 2 \times 10^{21}$ cm^{-2} (Böhringer et al., 2000).

1.3.5 HI-Surveys

The 21-cm line emission of neutral hydrogen (HI) from galaxies has proven to be the most powerful method of revealing galaxies in the most obscured region of the ZOA. HI emission was first detected by Ewen & Purcell (1951). However, Kerr & Hindman (1953) were the first to detect extragalactic HI. Neutral hydrogen emits a photon at a wavelength of 21-cm or at a frequency ~ 1.42 GHz. The emission occurs when atomic hydrogen in the ground state undergoes a hyperfine transition due to the spin-flip transition of proton and electron from parallel to anti-parallel (anti-parallel is a slightly lower energy state). In fact, the transition is so infrequent that it takes a single neutral hydrogen atom on average 11 million years to undergo this transition (Hey, 1971). Nevertheless, the amount of neutral hydrogen in a galaxy is so immense that the emission can be detected.

The Galaxy is fully transparent to the long wavelength of the 21-cm radiation. These photons pass without hindrance through interstellar dust. HI-bearing galaxies can therefore be found quite easily through the detection of their redshifted 21-cm emission. In addition, the signal also provides immediate information on the redshift, contrary to other wavebands, as well as rotational properties of the detected galaxy.

In addition, the HI content of galaxies can give some indication on the morphology of the detected galaxy. Studies of galaxies in the 21-cm line show that galaxies of different morphological type have different HI content. Early-type spirals seem to have lower HI mass than late-type spirals (Shostak, 1978). Moreover, irregular dwarf galaxies are found to be more HI rich than other dwarfs (Carignan, 1999).

The search for galaxies behind the Galactic Plane in the 21-cm line of HI was pioneered by Kerr & Henning (1987). They used the Green Bank 91m radio-telescope to carry out blind observations towards about 1900 pointings in the northern ZOA. Sixteen new spiral galaxies were detected in these observations, a similar detection rate compared to searches in other regions. The Dwingeloo Obscured Galaxies Survey (Kraan-Korteweg et al., 1994b; Henning et al., 1998; Rivers, 2000) is the first systematic HI survey in the most obscured region of the

northern ZOA. It surveyed the northern ZOA ($30° \leq l \leq 220°$, $|b| \leq 5°.25$) for galaxies out to 4000 km s^{-1} with an rms noise of 40 mJy beam^{-1}. A number of galaxies were detected in this survey including the nearby galaxy, Dwingeloo 1 (Kraan-Korteweg et al., 1994b). The survey, however, was limited in both sensitivity and depth.

More sensitive and large-area HI surveys were started in 1997 using the Multibeam receiver on the Parkes 64-m radio telescope (Kraan-Korteweg et al., 1998; Staveley-Smith et al., 1998). The Multibeam (MB) receiver, with 13 beams in a focal plane array (Staveley-Smith 1996), was specifically designed to perform rapid and systematic surveys of large areas. Since then, the various Multibeam HI surveys have uncovered thousands of new galaxies. Leading systematic surveys are:

- The HI Parkes All Sky Survey (HIPASS): it is a blind HI survey of the southern sky from declination (δ) $-90°$ up to $+25°$. It is the largest HI survey carried out thus far. The rms noise of the survey was 13 mJy beam^{-1} covering the velocity range of ~ -1200 to 12,700 km s^{-1}. In this survey 4315 galaxies were catalogued for $\delta < +2°$ (Meyer et al., 2004). In addition, the northern extension of HIPASS ($+2° < \delta < +25°$) produced a catalog of 1002 galaxies (Wong et al., 2006).

- The HI Parkes Deep Zone of Avoidance Survey, with five times longer exposure time than HIPASS, has an rms noise of 6 mJy beam^{-1}. The survey covered a region of $196° \leq l \leq 52°, |b| \leq 5°$ and the same velocity range of -1200 to 12,700km s^{-1} (Henning et al., 2005). The survey has yielded close to a thousand galaxies most of which were previously unknown. Moreover, the northern extension of this survey, $36° \leq l \leq 52°$ and $196° \leq l \leq 212°, |b| \leq 5°$ (Donley et al., 2005) has detected 77 HI galaxies. These surveys have been effective in filling the most opaque part of the ZOA, $|b| \leq 5°$.

1.4 Motivation for the Galactic Bulge Extension to the ZOA Survey

The success of the Parkes ZOA survey in identifying new galaxies and large-scale structures in highly obscured regions in addition to the following scientific motivations, led to an extension of the ZOA towards higher latitudes around the Galactic Bulge.

- Close to the Galactic Bulge the extinction flares up to higher latitudes, $|b| \simeq 20°$ (see Fig.1.4, and Section 1.3.3).

- Dynamically important structures, such as the Local Void (Tully & Fisher, 1987), are partly hidden by the Galactic Bulge. The Local Void is the nearest void to us. It has been suggested that the Local Void may be one of the sources of the origin of motion of the LG with respect to the CMB– the so-called the Local Velocity Anomaly (Faber & Burstein, 1988; Tully & Pierce, 1992). Several attempts have been made to find the actual dimensions of the Local Void (e.g. Nakanishi et al., 1997; Koribalski et al., 2004). However, the actual size and extent of the Local Void has yet to be well-defined. Recently Tully (2007) implies that the Local Void is larger and emptier than previously

thought. Clearly it is crucial to delineate its boundary more precisely to understand the dynamics of the local Universe. By mapping the galaxy distribution around the Bulge using HI surveys, the true dimensions of the Local Void may well be addressed better.

- Another region of interest close to the Galactic Center is the Ophiuchus cluster (Wakamatsu & Malkan, 1981). Wakamatsu et al. (2000) confirmed the presence of several clusters and groups of galaxies around the Ophiuchus cluster implying that it can be classified as a supercluster with a wall connecting the Ophiuchus and Hercules Superclusters. It is also found to be one of the most luminous X-ray clusters in the nearby Universe (Watanabe et al., 2001; Ebeling et al., 2002). From its closeness to the position of the GA, the Ophiuchus Supercluster has also been suggested to play some role in the GA's sphere of influence (Wakamatsu et al., 2005). However, since it is located close to the Galactic Center ($l = 0.°56, b = +9.°27$), a detailed mapping of the supercluster has been hampered by the ZOA.

- Recent HIZOA survey results imply the presence of a wall-like structure parallel to the Centaurus wall that might be part of the GA overdensity (Kraan-Korteweg, 2005). Extending the survey to the Bulge might confirm such a suspected structure.

An extension of the ZOA survey towards the Galactic Bulge (hereafter "the GB extension") has been carried out by the ZOA Multibeam working group for a region $332° \leq l \leq 36°, 5° \leq |b| \leq 10°$ and $352° \leq l \leq 24°, 10° \leq |b| \leq 15°$ in the period 2002 - 2005. Figure 1.5 shows the survey region with various rectangles and galaxies cataloged in other surveys (preliminary data from the HI Parkes deep ZOA, HIPASS, and other wavebands for the relevant velocity range as in LEDA). This thesis consists of a detailed analysis of the resulting data from the survey and the measurement of HI parameters of the galaxy candidates.

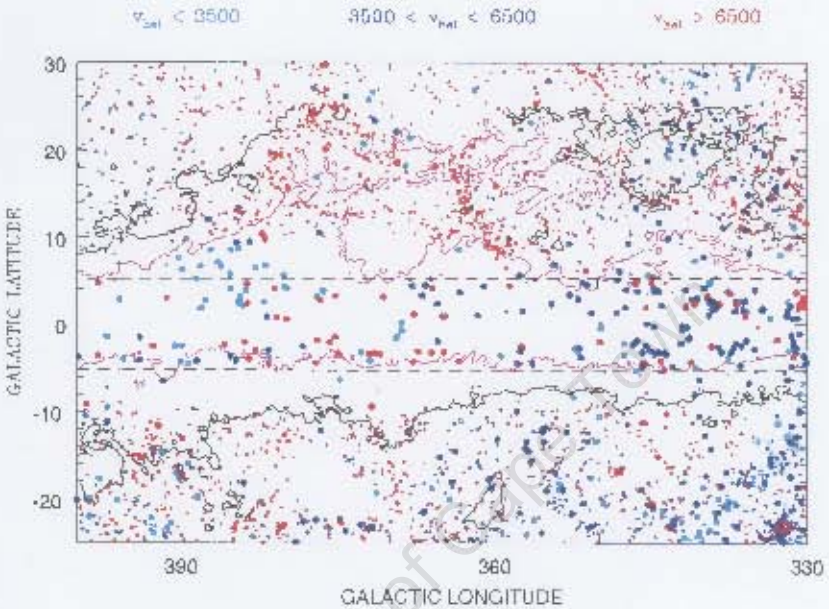

Figure 1.4: Distribution of galaxies cataloged in Lyon-Meudon Extragalactic Database (LEDA) (small dots), with velocities $cv < 12000$ km s^{-1}, HIPASS and ZOA (large dots) with DIRBE extinction contour of $A_B = 1^m$ and 3^m.

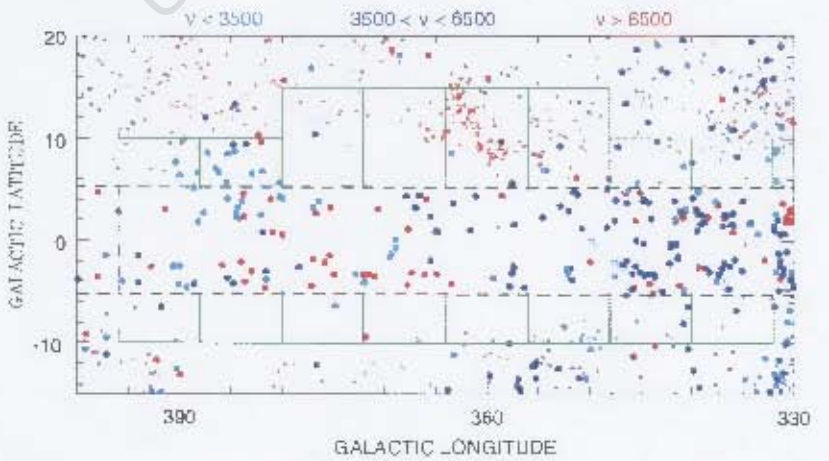

Figure 1.5: The rectangles indicate the GB extension region on the distribution of galaxies with velocities, $cv < 12000$ km s^{-1}, so far catalogued in ZOA survey, HIPASS and LEDA database (Kraan-Korteweg et al., 2005). HI detected galaxies are represented by large dots and galaxies from LEDA (mostly optical) represented by small dots.

1.5 Outline of this Thesis

Chapter 2 of this thesis presents details of the GB extension survey and the search method used for finding galaxies. The visualization tool and galaxy identification process is described in Section 2.2, galaxy selection criteria in Section 2.3 and the HI parametrization in Section 2.4.

Chapter 3 presents the results of the survey. The catalog of galaxy candidates is presented in Section 3.1 and the HI spectra of each candidate can be found in Appendix A. The accuracy of the measured HI parameters is compared with: a) candidates detected twice in the overlapping areas of adjacent data cubes in the GB extension survey itself b) galaxies from HIPASS in the overlapping regions and c) independent search made at the time by a second party for the part of the GB extension survey (Section 3.3). A multi-wavelength counterpart search done for our detections as well as an ongoing NIR follow-up of HI selected galaxy sample using the the Japanese Infrared Survey Facility (IRSF) at the Sutherland observing site of the South African Astronomical Observatory is presented in Section 4.3.

Chapter 4 describes the implications of the GB extension detections for the large-scale structure of the nearby Universe. The detections of GB extension confirmed a number of suspected large-scale structures as well as a new feature in the distribution of galaxies.
The final chapter, Chapter 5, summarizes results and describes the ongoing work.

Chapter 2

Observations and Search Method

2.1 Data Acquisition

The observations of the ZOA GB extension survey were carried out at the Parkes 64-m radio telescope using the Multibeam receiver in much the same setup as for the deep ZOA survey. The Multibeam receiver consists of 13 beams in a focal plane array, each with a beamwidth of 14′.3 (?). It has an average system temperature of 20 K. The correlator has a bandwidth of 64 MHz divided into 1024 channels, giving 13.2 kms^{-1} of channel spacing. It covers a range in redshift space of -1200 $\text{kms}^{-1} < cz < 12,700$ kms^{-1}. The survey parameters are given in Table 2.1

Table 2.1: The Survey Parameters

Parameter	Value
Areal coverage	$332° \leq l \leq 36°, 5° \leq \|b\| l e 10°$ and $352° \leq l \leq 24°, 10° \leq \|b\| \leq 15°$
Velocity coverage	$-1200 < cz < 12,700$ km s^{-1}
Telescope FWHP resolution	14′.3
FWHP resolution in data cube	15′.5
Velocity resolution*	27 kms^{-1}
Integration time	20 min beam^{-1} (on average)
rms noise	$\sim$ 6 mJy beam^{-1}

*After Hanning smoothing.

The observations were made by scanning the telescope across the sky at constant Galactic latitude, in strips of length $\Delta l = 8°$ where each scan was offset by 35′ in latitude (see the scan pattern shown in Figure 2.1). During each scan the rotation angle of the receiver was 15°, with respect to the scan direction, at the midpoint of the scan, to obtain reasonably uniform coverage of the sky. However, there was a small overlap between the fields to achieve complete sampling of the survey region. The foot print of the Multibeam receiver on the sky is $\sim 1°.7$, so that a single scan maps out 8° long and 1°.7 wide strips of Galactic longitude. A

total of 320 scans were made on 16 fields, 8 above and 8 below the Galactic Plane, between latitudes, $-10°$ to $-5°$ in the South, $+5°$ to $+10°$ and $+5°$ to $+15°$ in the North for longitude range of $332° \leq l \leq 36°$ as shown in 1.5. The survey is slightly less deep with 20 scans on average compared to the 25 scans of the ZOA and Northern Extension to the ZOA surveys. The data were bandbpass-corrected, calibrated and Doppler-corrected using the specially

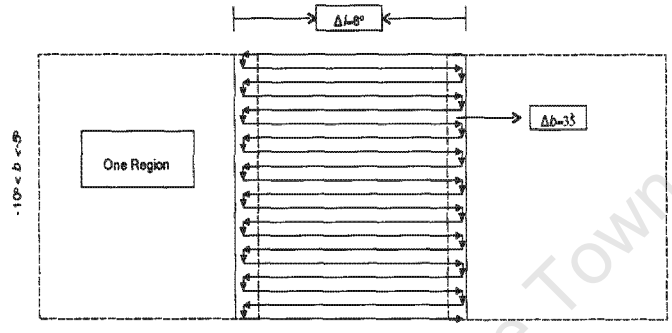

Figure 2.1: Observation mode for a region ($8° \times 5°$) scanned in Galactic longitude 20 times. Adjacent regions extend slightly beyond the boundaries and overlap in Galactic longitude.

developed Astronomical Image Processing System (AIPS) ++ LIVEDATA (Barnes et al., 2001) software tool. The data were then gridded using GRIDZILLA (Barnes et al., 2001) into slightly overlapping cubes of size $8° \times 5°$ and $8° \times 10°$, and pixel size of $4' \times 4'$ and $15'.5$ beam size.

Baseline ripples due to strong continuum emission were removed using the "scaled template method " (Barnes et al., 2001). However, some residual baseline ripples still remain. Hanning smoothing is applied to suppress spectral ringing associated with Galactic HI emission. The Galactic HI emission is strong and contains narrow emission lines which cause ringing in the spectra that decay as n^{-1}, where n is the number of channels away from the narrow line (Barnes et al., 2001). This ringing can affect the data over a large velocity range. Hanning smoothing is a standard procedure used to reduce this effect (see Barnes et al., 2001, for detail). Figure 2.2 shows an example of strong ringing folowed by the same spectra after Hanning smoothing. The resulting data are three dimensional cubes (Right Ascension-Declination, Right Ascension-Velocity and Velocity-Declination).

2.2 Visualization Tool and Galaxy Identification

The three dimensional data cubes were displayed and viewed using KVIS in KARMA (Gooch, 1996), a package for visualization, signal processing and image application. KVIS displays the data in two dimensions and allows the user to step through the third dimension of the cube.

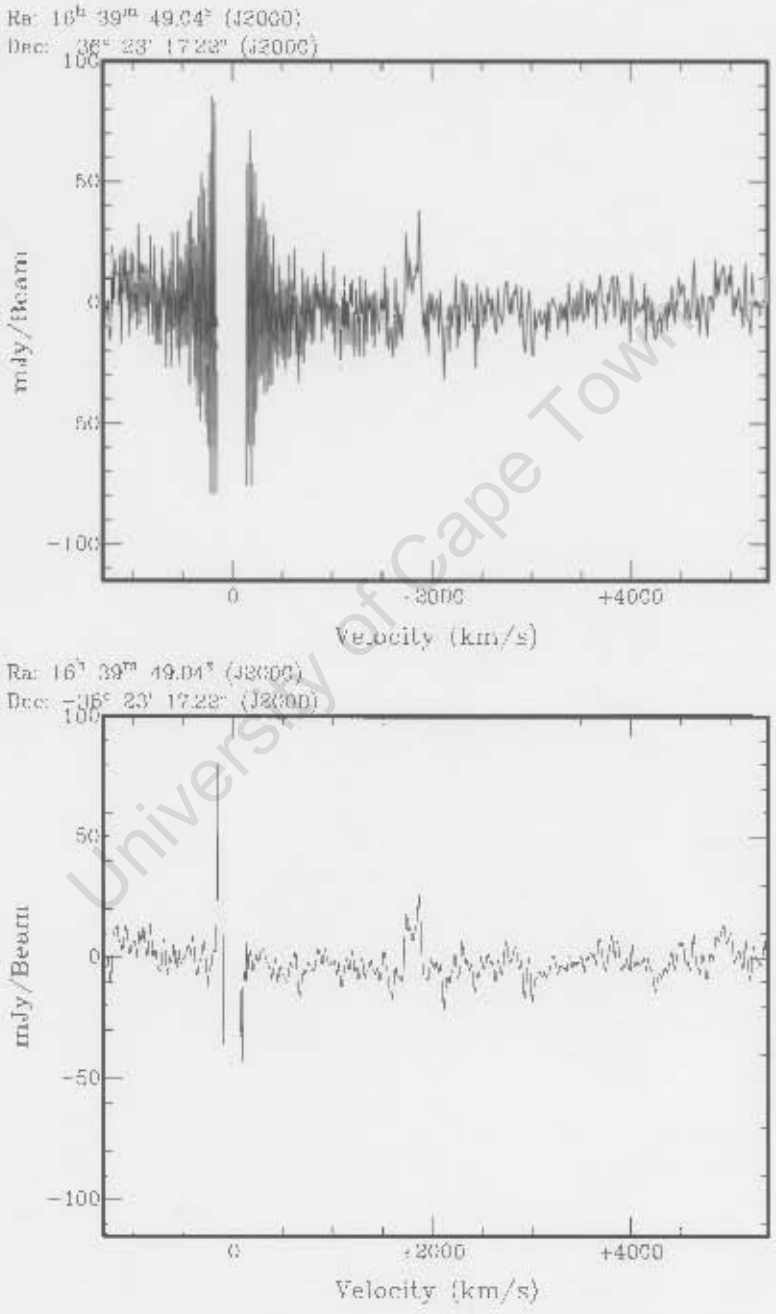

Figure 2.2: The top panel shows a pectrum before Hanning smoothing. The spectrum contains strong Galactic emission near 0 km s^{-1} and extragalactic emission around 1800 km s^{-1}. The bottom panel shows the same spectrum after applying Hanning smoothing.

The search for galaxies is done by visual inspection in the three planes (Right Ascension-Declination, Right Ascension-Velocity and Velocity-Declination) as shown in Figure 2.3. Experiments with automatic galaxy detection algorithms (e.g. MultiFind; Kilborn, 2001) indicated that in the ZOA, with regions of high and variable noise due to continuum sources and Galactic HI, the visual search is more efficient at finding galaxies. A test on the GB extension cubes using even improved galaxy-finding algorithm, Duchamp (Whiting, 2007) also shows that difficulty of detecting galaxies in these region using automatic galaxy finder algorithm (see Appendix A).

The searching of the GB extension data cubes was started after gaining experience of galaxy identification on previously searched ZOA data cubes. According to my systematic procedure, a cube was initially displayed in velocity and declination plane. The next step was setting the intensity scale to 98% (clip the inner 98% of the data value) and the "Pseudo-color" to "grayscale 1" sometimes to "heat". Choosing the "line" profile mode in the view control panel, the cube was searched stepping through Right Ascension axis and a list was made of all candidates parameters. The cube was then displayed in Right Ascension and Declination plane and stepped through velocity axis. A third independent search was also done in Right Ascension and velocity, stepping through Declination, without consulting the two lists made from the other two planes. Finally the three lists were compared for reliablity by checking at the corresponding positions of the possible sources in all three lists. Sources which were visible in only one of the three planes were not included in the final list. A total of 16 data cubes were inspected in this manner. The three display modes of KVIS are shown in Fig. 2.3 along with examples of galaxy candidates and their spectrum profiles in Fig. 2.4.

2.3 Galaxy Selection Criteria

In order to obtain a uniform list of HI detections, the selection of galaxy candidates was based on the following criteria. A detection:

- must be clearly visible above the noise level which is about 4 times the cube rms noise. This is typically $\sim$ 6 mJy beam^{-1} as measured using the MIRIAD task IMSTAT in regions free from detectable sources. That means, a detection should have a minimum peak flux density of about 25 mJy beam $^{-1}$,
- must have a spatial extent of three or more pixels,
- must be visible over two or more velocity planes.

Note that galaxies that lie in the velocity range of $V \leq \pm 250$ kms^{-1}, i.e., within or close to the Galactic HI emission, are likely to be missed as their emission will be overshadowed by the strong flux of the Galactic HI. Moreover, galaxies that are close to radio continuum sources may not be found because of residual baseline ripples. In addition, one possible candidate within the velocity range, $V < +340$ kms^{-1}, is also excluded in the final catalog as confusion with High Velocity Clouds (HVCs; see Putman et al., 2002) makes galaxy identification

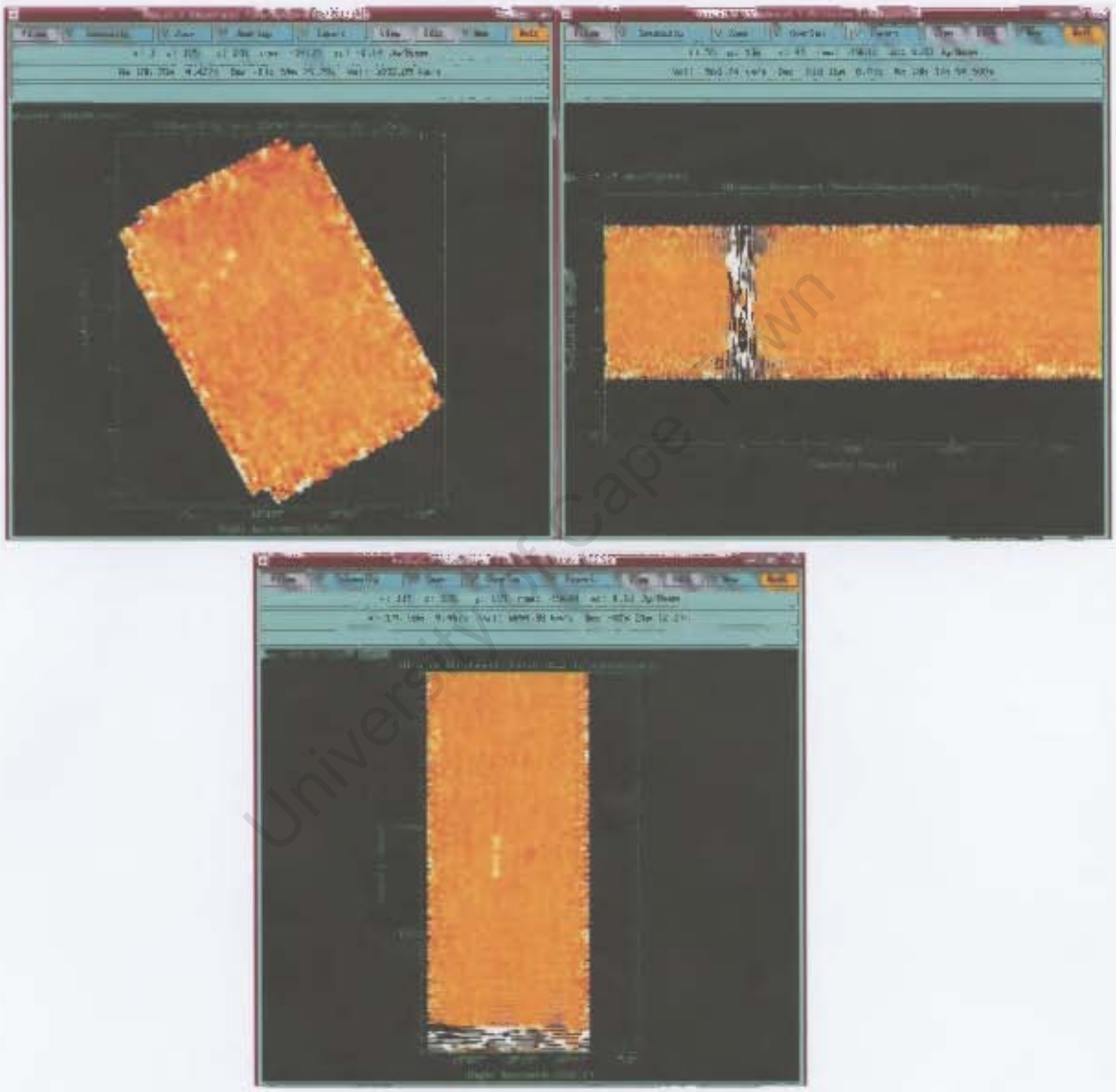

Figure 2.3: The top-left panel shows a Right Ascension - Declination plane of the cube Z024N in a single velocity channel with galaxies visible as higher intensity blobs. The top right panel shows Velocity - Declination plane at the Right Ascension of one of the galaxies visible in the left panel. The Galactic HI is visible as vertical feature in this plane at ~ 0 km s^{-1}. The lower panel shows the Right Ascension - Velocity plane at Declination of one of the galaxies in the top-left panel. The galaxy has quite broad velocity width.

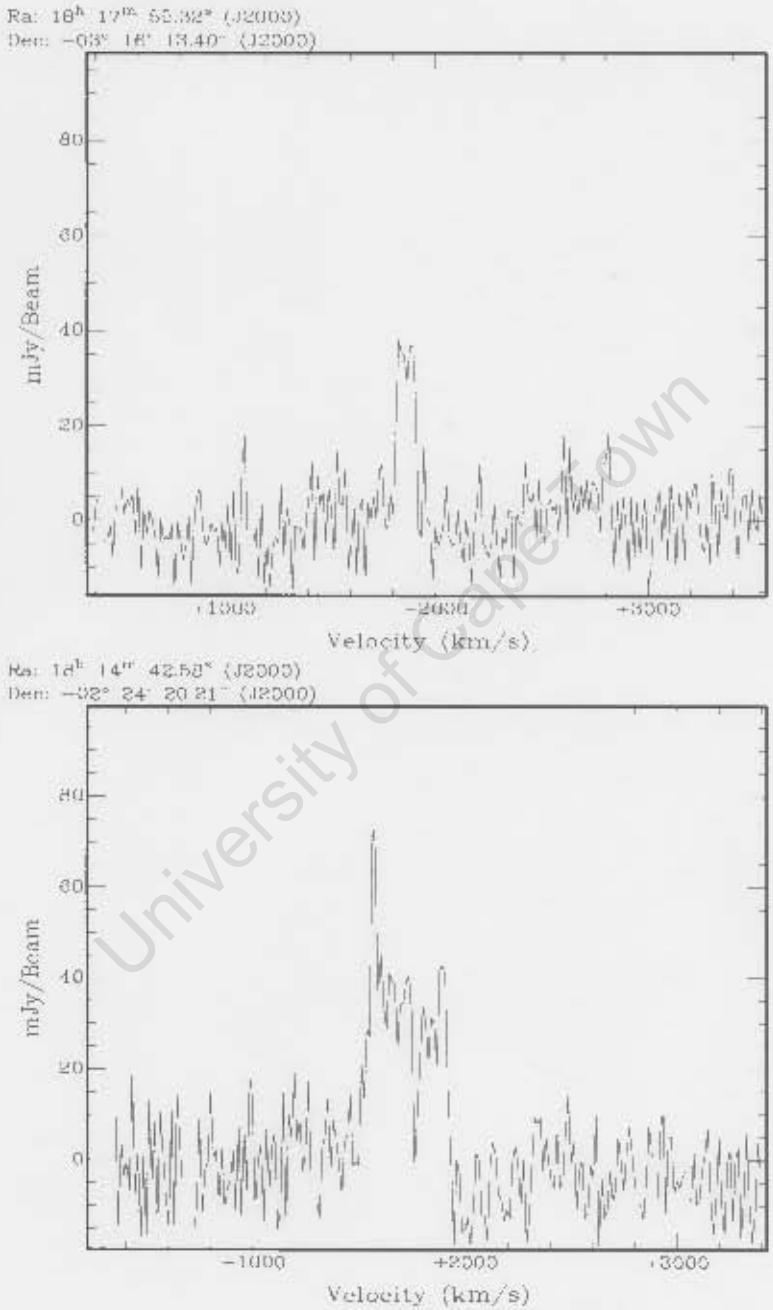

Figure 2.4: The profiles of two of the detections in Fig. 2.3. The top panel shows a normal narrow profile for the source shown in the top-right panel of Fig 2.3. In the lower panel a profile of a broad, possibly two neighbouring sources, is evident for the detection shown in the lower panel of Fig. 2.3.

difficult.

As visual inspection may be subjective, the search will be done by three independent searchers producing an independent list of galaxy candidates (same as for the ZOA and northern extension surveys). These will then be cross-checked by a neutral person. For the GB extension cubes a second search by collaborators in the University of Western Australia was made for half of the data (8 cubes) at the time of this thesis. This independent list of galaxy candidates (see Section 3.2) will be used for comparison with the list produced in this thesis work.

2.4 HI Parametrization

2.4.1 Measured HI parameters

The HI parameters of a galaxy signal were determined in a semi-automatic manner. The first step was to measure preliminary positions and velocities visually by reading them off the interactive KVIS display window. A script developed by L. Staveley-Smith[1] (the same script used for previous Parkes HI ZOA surveys), which uses a modified version of the MBSPECT task in the MIRIAD software package (Sault et al., 1995), was applied for measuring the HI parameters, where the fitting programme reads the measured preliminary parameters from an input file. The central positions were determined by spatially fitting a Gaussian of interactively specified width to the velocity-integrated plane. These positions were then used to produce an integrated spectrum (see Appendix A). Care was taken in choosing the width of the Gaussian to ensure that it is wide enough to not remove the observed noise of the spectrum artificially. A first-order base line was fitted to each spectral profile. However, for most of the detections, a first-order fit was unrealistic because of the strong baseline ripples. In such cases, higher order baseline were used. The velocity widths at 20% and 50% of the peak flux density were also measured. The heliocentric velocity was taken to be the central velocity at the 50% of the profile's peak flux density. Examples illustrating baseline-fitted spectra with their resulting parameters are shown in Fig. 2.5 and Fig. 2.6.

The extent of the HI emission of most of the detections in the GB extension is less than $15'.5$, the angular resolution of the gridded data. This means that they can be treated as point sources. For these sources a region of size $28'$ around the source is analyzed. In some cases, where sources are marginally extended, a region of size $12'$ and $20'$ was used to remove the flux contributions from neighbouring sources.

2.4.2 Derived HI parameters

The global HI parameters were obtained in a straightforward way. The distance to a galaxy candidate was determined from the Hubble law based on the velocity of the galaxy in the Local Group standard rest frame,

$$D = \frac{V_{LG}}{H_0} \tag{2.1}$$

[1]University of Western Australia

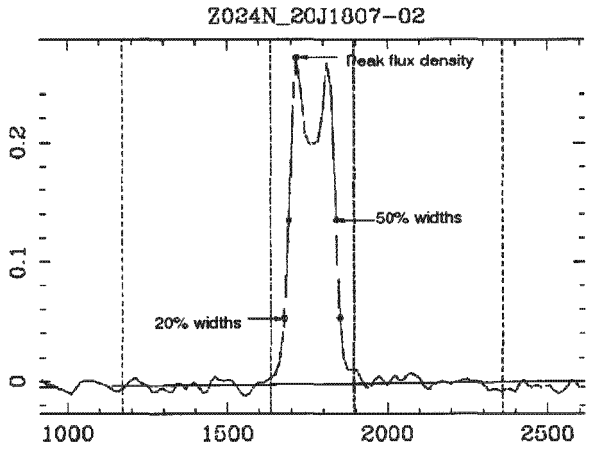

Figure 2.5: Example spectrum after baseline fitting. The locations of peak flux density, S_p, and 50% and 20% widths, W_{50} and W_{20} respectively, are shown. The inner dotted lines indicate the velocity range over which the candidate profile was measured, whereas the outer dotted lines indicate the region over which the baseline was fitted.

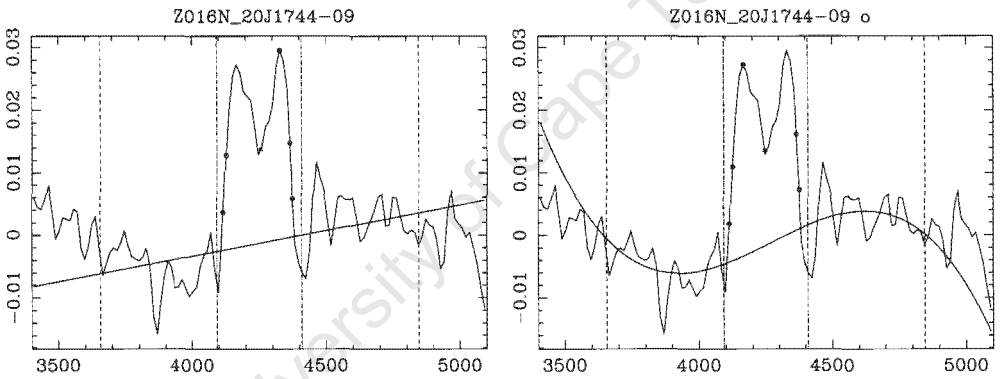

Figure 2.6: Example of cases where fitting first-order baseline was unsuccessful. First-order (left) and third-order (right) fitted baselines. The third-order fitting seem to be more realistic.

where V_{LG} is the Local Group velocity (in km s^{-1}) corrected for the motion of the Sun in the Galaxy and the Galaxy in the Local Group. It is derived using the IAU convention: $V_{LG} = V_{hel} + 300sin(l)cos(b)$, where V_{hel} is the heliocentric velocity, l and b are Galactic longitude and latitude, H_0 is the Hubble constant. All velocities mentioned in this thesis are in the optical ($v = cz$) convention and a Hubble constant of H_0= 75 km s^{-1} Mpc^{-1} is used throughout.

The other derived parameter is the HI mass. It is derived from:

$$M_{HI} = 2.356 \times 10^5 D^2 \int S dv M_\odot \tag{2.2}$$

assuming that the galaxy is fully transparent. S is the measured spatially integrated flux in Jy kms^{-1}, D is the distance to the galaxy candidate in Mpc. The integral is over the velocity width of the galaxy (in km s^{-1}) and $M_\odot$ is the mass of the Sun.

Chapter 3

3.1 Results

Applying the search method described in the previous chapter, a list of 158 galaxy candidates has been produced for the final catalog. Because adjacent data cubes slightly overlap in Galactic longitude, 13 candidates appeared twice in neighboring cubes. Choosing a position matching limit of 5 arcmin and 25 km s^{-1}, double detections were removed from the final list. The candidate located within a well-defined region of a cube, i.e., within $\Delta l = \pm 4°$ of the central longitude of the data cube, was chosen for the final catalog (see Table 3.3 for the HI parameters of double detections).

To generate a consistent list of galaxies, all galaxy candidates should be inspected by an adjudicator, who will make the final decision whether a candidate is to be included in the final catalog. This was possible for part of the survey that was independently examined by the second party, i.e., for 8 cubes over the longitude range of 336° to 0° out of the 16 cubes. P.A. Henning [2], adjudicator of the ZOA and northern extension cubes, has inspected these cubes. Of 113 candidates listed in this region, 94 are accepted as a real galaxies. The other part of the survey has not been searched by an independent party yet. A complete adjudication will be done in the near future when the other 8 cubes ($8° \leq l \leq 32°$) are examined by a second person. Based on my experience and the HI parameters, I regard 59 as real and 5 as probable galaxies from the remaining 8 cubes.

The 19 candidates in the first 8 cubes that were not accepted by the adjudicator are listed in Table 3.1. All of them have very low peak flux density. Some were discarded as they could be the top of a baseline ripple (for example the candidate with HI spectrum shown in the left panel of Fig. 3.1). Some have been discarded because of wobbly baselines, like the candidate shown in the right panel of Fig.3.1, and a few have been thrown out as high noise. Although they are not included in our list, some of them could turn out to be real, yet this can not be confirmed without further data.

The columns of Table 3.1 contain the following information:

Columns 1 & 2: Equatorial coordinates (J2000) ;
Columns 3 & 4: Galactic coordinates corresponding to the source position;
Column 5: Peak flux density;
Columns 6 & 7: Minimum and maximum velocities of the width of signal respectively.

[2]Institute for Astrophysics, University of New Mexico

Table 3.1: Discarded galaxy candidates

R.A. (J2000) h m s	Dec. (J2000) deg ′ ″	l deg	b deg	F_p mJy beam^{-1}	V_{low} km s^{-1}	V_{high} km s^{-1}
15 53 35	−42 10 45	335.30	8.96	30	7093	7572
16 08 38	−41 38 45	337.78	7.50	32	7544	7875
16 18 45	−37 34 29	342.05	9.08	32	4419	4850
16 23 50	−28 38 43	349.39	14.50	27	7592	8082
16 27 50	−37 40 32	343.24	7.72	34	4407	4682
16 28 34	−35 12 34	345.16	9.30	37	3645	3853
16 33 02	−27 23 42	351.74	13.82	35	4648	4866
16 40 41	−35 22 58	346.70	7.34	25	3778	3891
16 44 12	−34 57 35	347.50	7.07	38	4820	5065
16 46 13	−31 02 43	350.80	9.26	25	9275	9670
16 47 46	−29 18 44	352.38	10.10	25	5984	6371
16 51 02	−26 26 26	355.12	11.33	25	7630	8251
16 52 51	−32 46 26	350.35	7.08	25	7849	8066
16 53 42	−31 14 12	351.67	7.90	27	2956	3189
16 54 54	−30 41 58	352.26	8.03	27	6991	7555
16 57 26	−53 59 43	334.28	−6.84	25	2678	2877
17 42 42	−49 49 02	341.76	−10.35	35	9533	9908
18 07 01	−37 09 01	355.09	−7.97	28	2820	3002
18 07 21	−41 37 05	351.12	−10.11	29	8075	8523

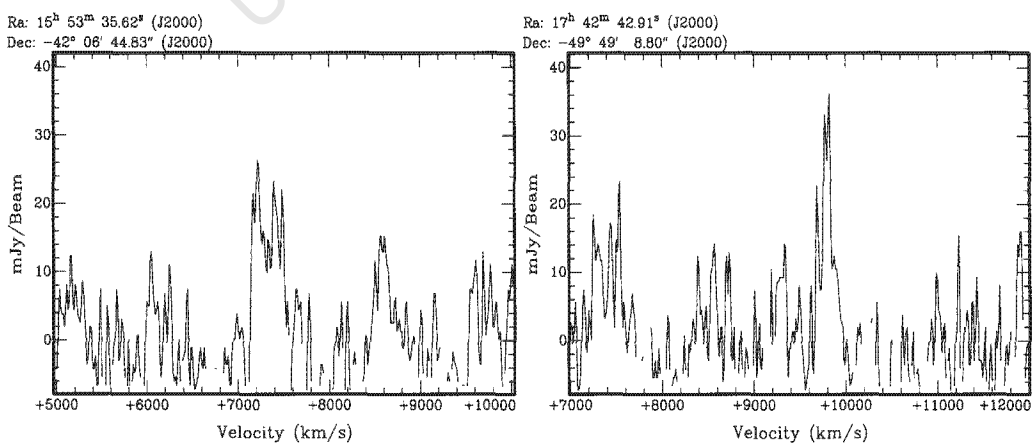

Figure 3.1: Examples of spectrum profiles of discarded galaxy candidates . Left panel: candidate at RA=$15^h53^m35^s$ and Dec=$-42°06'44''$. Right panel: candidate at RA= $17^h42^m42^s$ and Dec=$-49°49'08''$.

3.2 The Catalog

The HI properties of the 158 galaxies are given in Table 3.2. The entries in the table contain the following information:
Column 1: Source name, which is given as JXXXX ± YY, where XXXX is the source RA in hours (h) and minutes (m) and YY is the source Dec in degrees (deg) following standard nomenclature. The letters (A or B) are added to distinguish close sources with the same source name;
Columns 2 & 3: Equatorial coordinates (J2000) of the candidate. This is the Gaussian-fitted position of the source (see Section 2.4.1);
Columns 4 & 5: Galactic coordinates;
Column 6: Heliocentric velocity. This is the central velocity measured from the 50% of the profile's peak flux density;
Column 7 & 8: Velocity width at 50%, and at 20% of the peak flux density (see Section 2.4.1);
Column 9: Integrated HI flux;
Column 10: Velocity corrected to the LG rest frame (as described in Section 2.4.2);
Column 11: Distance to the galaxy candidate derived from equation 2.1 (see Section 2.4.2);
Column 12: Logarithm of the HI mass as determined from equation 2.2 (see Section 2.4.2).

The HI spectra of the candidates are shown in Appendix A. All the detection profiles show one of the common velocity profiles of a galaxy, i.e, a double horn profile of an edge-on spiral galaxy, a flat top profile of a face-on spiral galaxy, or a Gaussian profile of an irregular galaxy.

Table 3.2: HI Parameters

Source name	RA (J2000) h m s	Dec (J2000) deg ′ ″	l deg	b deg	V_{hel} km s^{-1}	W_{50} km s^{-1}	W_{20} km s^{-1}	S Jy km s^{-1}	V_{LG} km s^{-1}	D Mpc	log M_{HI} ($M_\odot$)
J1538-44	15 38 23.17	-44 26 33.5	331.69	8.91	3455	144	176	7.80	3708	49.4	9.65
J1539-44	15 39 29.20	-44 31 04.3	331.80	8.73	3434	224	246	9.13	3649	48.6	9.71
J1546-42	15 46 53.12	-42 21 20.1	334.22	9.61	4637	172	192	3.56	4361	58.2	9.45
J1549-46	15 49 16.21	-46 50 07.6	331.72	5.85	775	38	62	2.10	513	6.8	7.37
J1556-42	15 56 57.62	-42 34 10.8	335.53	8.26	5755	86	120	5.56	5686	75.8	9.88
J1603-43	16 03 30.96	-43 15 40.3	335.98	6.95	5946	159	175	3.04	5986	79.8	9.66
J1604-41	16 04 44.91	-41 43 35.4	337.19	7.94	4743	200	447	12.18	4765	63.5	10.06
J1607-43	16 07 22.93	-43 13 57.3	336.53	6.50	4605	209	235	4.40	4498	59.9	9.57
J1610-38	16 10 31.28	-38 20 26.0	340.34	9.67	4503	142	179	4.83	4251	56.7	9.70
J1616-40	16 16 07.96	-40 02 04.3	339.94	7.70	4438	344	378	15.71	4466	59.5	10.12
J1617-38	16 17 24.03	-38 10 59.7	341.43	8.84	4452	58	146	3.12	4241	56.5	9.37
J1620-39	16 20 30.47	-39 36 24.3	340.84	7.41	2380	88	113	7.54	2509	33.4	9.33
J1621-36	16 21 06.14	-36 08 38.4	343.42	9.75	4447	370	447	42.23	4684	62.4	10.59
J1623-40	16 23 43.37	-40 39 03.4	340.53	6.24	4805	43	75	2.56	5088	67.8	9.44
J1624-42	16 24 52.51	-42 26 43.7	339.39	4.83	2222	165	215	22.58	2225	29.7	9.59
J1626-40	16 26 48.12	-40 48 53.6	340.82	5.70	4755	236	253	5.78	5006	66.7	9.78
J1628-29	16 28 05.26	-29 06 23.6	349.69	13.50	4180	426	448	7.53	4033	53.8	9.71
J1629-26	16 29 46.93	-26 45 13.1	351.75	14.79	5143	334	392	7.05	5162	68.8	9.90
J1630-30	16 30 16.37	-30 33 46.2	348.90	12.17	4109	207	291	8.09	4057	54.1	9.75
J1631-28	16 31 46.53	-28 05 53.7	351.02	13.57	4188	243	289	9.68	4067	54.2	9.83
J1632-28	16 32 04.22	-28 05 32.3	351.06	13.52	4104	518	563	14.57	3981	53.1	9.99
J1632-29A	16 32 35.48	-29 30 34.9	350.05	12.50	4066	55	83	2.42	3775	50.3	9.16
J1632-29B	16 32 46.45	-29 23 08.1	350.17	12.55	4827	282	305	6.70	4529	60.4	9.76
J1634-27	16 34 09.00	-27 37 04.8	351.74	13.49	4231	99	119	3.36	4210	56.1	9.40
J1635-33	16 35 33.26	-33 46 56.5	347.22	9.19	3927	65	87	2.82	3636	48.5	9.19
J1636-26	16 36 10.38	-26 10 22.7	353.17	14.09	4109	239	263	8.12	4124	54.9	9.76
J1637-35	16 37 40.87	-35 55 31.2	345.89	7.45	3719	70	95	3.20	3756	50.1	9.28
J1639-28	16 39 05.99	-28 57 37.5	351.43	11.79	6256	236	265	5.92	6166	82.2	9.97
J1639-36	16 39 56.48	-36 22 23.9	345.86	6.81	1813	175	210	4.75	1885	25.1	8.85
J1640-35	16 40 27.03	-35 20 06.5	346.71	7.41	3878	84	105	1.69	3994	53.3	9.05
J1641-24	16 41 54.79	-24 55 13.1	355.02	13.89	8344	413	513	10.52	8342	111.2	10.49
J1642-29	16 42 01.15	-29 10 38.8	351.68	11.16	2578	148	200	5.27	2569	34.2	9.16
J1642-37	16 42 45.70	-37 31 42.3	345.35	5.63	2643	162	192	6.54	2590	34.5	9.26
J1643-29	16 43 03.60	-29 39 30.5	351.45	10.68	6286	185	246	3.69	6323	84.3	9.79
J1643-30	16 43 13.93	-30 56 16.2	350.48	9.83	6788	224	270	7.39	7059	94.1	10.19
J1643-54	16 43 23.09	-54 02 34.7	332.93	-5.28	5206	191	211	4.25	5194	69.2	9.68
J1644-55	16 44 27.04	-55 29 49.7	331.92	-6.35	5114	441	482	23.62	4849	64.6	10.37
J1644-27	16 44 29.41	-27 23 26.3	353.44	11.88	8301	157	317	6.38	8533	113.8	10.29
J1648-31	16 48 35.58	-31 55 46.1	350.44	8.31	6691	150	186	6.81	6822	90.9	10.12
J1648-54	16 48 19.55	-54 26 01.8	333.10	-6.09	4654	282	305	5.76	4681	62.0	9.72
J1649-35	16 49 40.43	-35 10 08.8	348.07	6.08	3526	189	218	9.70	3704	49.4	9.75

Table 3.2–Continued

Source name	RA (J2000) h m s	Dec (J2000) deg ′ ″	l deg	b deg	V_{hel} km s^{-1}	W_{50} km s^{-1}	W_{20} km s^{-1}	S Jy km s^{-1}	V_{LG} km s^{-1}	D Mpc	log M_{HI} ($M_\odot$)
J1650-32	16 50 32.84	-32 20 03.1	350.39	7.74	6948	309	401	7.95	6913	92.2	10.20
J1651-22	16 51 58.03	-22 23 35.0	358.53	13.66	5859	105	151	3.87	5911	78.8	9.75
J1652-28	16 52 09.15	-28 19 27.8	353.78	9.98	7718	351	431	12.52	7478	99.7	10.47
J1652-32	16 52 25.39	-32 50 43.5	350.24	7.11	8206	53	142	1.40	8003	106.7	9.57
J1653-32	16 53 16.70	-32 39 15.5	350.51	7.09	8592	153	188	4.90	8389	111.8	10.16
J1653-24	16 53 44.95	-24 43 14.9	356.89	11.91	8372	108	159	4.13	8146	108.6	10.06
J1653-35	16 53 59.76	-35 30 28.4	348.36	5.19	6364	154	270	11.52	6411	85.5	10.30
J1654-35	16 54 04.36	-35 34 46.5	348.32	5.13	6365	179	270	11.78	6412	85.5	10.31
J1654-56	16 54 24.19	-56 23 27.4	332.12	-7.99	4912	149	339	7.50	4943	65.9	9.89
J1657-27	16 57 54.91	-27 27 04.9	355.27	9.51	6330	99	125	3.84	6409	85.5	9.82
J1658-21A	16 58 02.90	-21 17 54.0	0.30	13.19	5983	279	357	11.92	6055	80.7	10.26
J1658-21B	16 58 22.28	-21 35 32.1	0.11	12.95	5959	233	268	8.92	5988	79.8	10.13
J1658-30	16 58 41.78	-30 38 22.5	352.82	7.43	2796	165	203	4.48	2897	38.6	9.20
J1658-32	16 58 57.05	-32 40 53.1	351.23	6.13	8418	150	193	7.77	8243	109.9	10.34
J1701-19	17 01 53.69	-19 19 09.0	2.49	13.62	7272	231	263	2.42	7362	98.2	9.74
J1702-52	17 02 20.06	-52 50 55.7	335.65	-6.73	4445	110	147	8.08	4575	61.0	9.85
J1702-27	17 02 25.98	-27 50 11.7	355.57	8.48	4546	107	141	3.78	4641	61.9	9.53
J1703-18	17 03 24.62	-18 55 23.4	3.04	13.56	6134	107	172	3.53	6151	82.0	9.75
J1703-23	17 03 17.75	-23 49 02.3	358.96	10.72	6006	72	89	1.80	5945	79.3	9.43
J1703-26	17 03 12.01	-26 40 16.5	356.62	9.04	8623	94	179	2.90	8901	118.7	9.98
J1704-20	17 04 14.00	-20 23 37.1	1.92	12.55	9779	117	158	2.64	10060	134.1	10.05
J1704-33	17 04 39.17	-33 11 21.4	351.55	4.88	6204	169	193	6.61	6189	82.5	10.03
J1705-21	17 05 01.72	-21 55 12.3	0.77	11.51	10213	54	180	3.71	10315	137.5	10.22
J1705-24	17 05 59.16	-24 43 10.5	358.59	9.69	6150	146	202	6.68	6025	80.3	10.01
J1705-27	17 05 32.20	-27 07 58.1	356.56	8.35	8247	81	121	2.79	8389	111.8	9.92
J1705-29	17 05 35.71	-29 41 43.8	354.49	6.81	2676	179	200	16.68	2803	37.4	9.74
J1706-21	17 06 35.27	-21 19 20.4	1.48	11.56	9005	159	202	5.76	9165	122.2	10.31
J1707-24	17 07 38.59	-24 49 57.1	358.72	9.32	8461	132	171	2.90	8298	110.6	9.92
J1708-22	17 08 15.84	-22 49 32.5	0.46	10.37	9841	141	174	3.53	9763	130.2	10.15
J1708-25	17 08 25.54	-25 45 16.2	358.07	8.64	8726	501	550	7.94	8742	116.6	10.41
J1708-31	17 08 37.12	-31 20 33.9	353.54	5.31	7141	216	246	6.69	7308	97.4	10.18
J1708-56	17 08 48.37	-56 34 52.6	333.17	-9.69	4671	101	122	3.42	4624	61.6	9.49
J1711-47	17 11 40.04	-47 35 35.0	340.78	-4.79	2190	232	278	20.51	2214	29.5	9.62
J1712-25	17 12 01.08	-25 46 44.3	358.52	7.96	6328	352	458	8.64	6316	84.2	10.16
J1712-15	17 12 27.60	-15 06 35.7	7.54	13.93	2937	206	317	4.51	2995	39.9	9.23
J1716-15	17 16 27.88	-15 45 04.0	7.53	12.77	8523	315	396	4.84	8801	117.3	10.20
J1718-27	17 18 05.11	-27 52 10.5	357.58	5.65	6294	61	396	8.85	6166	82.2	10.15
J1719-45	17 19 46.83	-45 52 28.4	343.00	-4.94	5804	254	287	5.62	5768	76.9	9.89
J1719-48	17 19 13.18	-48 47 36.6	340.53	-6.51	4061	112	134	4.09	4337	57.8	9.51
J1720-15	17 20 48.22	-15 40 09.8	8.19	11.94	9296	115	178	3.69	9526	127.0	10.15
J1722-11	17 22 38.65	-11 49 56.0	11.75	13.63	4899	308	374	8.10	4793	63.9	9.89

Table 3.2 –Continued

Source name	RA (J2000) h m s	Dec (J2000) deg ′ ″	l deg	b deg	V_{hel} km s^{-1}	W_{50} km s^{-1}	W_{20} km s^{-1}	S Jy km s^{-1}	V_{LG} km s^{-1}	D Mpc	log M_{HI} ($M_\odot$)
J1723-45	17 23 25.27	-45 28 31.4	343.69	-5.24	6572	182	219	6.86	6429	85.7	10.07
J1726-14	17 26 28.34	-14 27 37.9	9.98	11.44	8362	147	331	4.25	8294	110.6	10.09
J1727-18A	17 27 18.88	-18 47 14.2	6.38	8.95	346	107	156	5.98	320	4.3	7.41
J1727-18B	17 27 56.22	-18 57 08.6	6.32	8.73	4181	188	222	4.22	4172	55.6	9.49
J1727-49	17 27 46.40	-49 26 37.3	340.77	-8.04	3940	208	233	9.38	3885	51.8	9.77
J1729-11	17 29 51.99	-11 02 36.6	13.40	12.53	8271	145	165	2.78	8492	113.2	9.92
J1732-43	17 32 21.21	-43 15 28.3	346.43	-5.35	2500	125	215	10.62	2635	35.1	9.49
J1732-15	17 32 25.31	-15 57 42.8	9.46	9.43	8122	162	176	2.33	8132	108.4	9.81
J1733-09	17 33 18.71	-09 33 00.8	15.15	12.58	5502	138	244	3.81	5660	75.5	9.71
J1733-17	17 33 53.03	-17 44 55.8	8.11	8.19	8680	159	200	2.69	8585	114.5	9.92
J1734-44	17 34 03.26	-44 32 45.3	345.51	-6.30	5821	231	261	5.99	5800	77.3	9.93
J1734-16	17 34 23.66	-16 45 21.1	9.03	8.61	1417	65	88	2.29	1338	17.8	8.23
J1734-13	17 34 24.69	-13 36 41.6	11.75	10.25	7817	308	402	7.81	7965	106.2	10.32
J1734-18	17 34 57.69	-18 18 57.1	7.76	7.67	8308	99	139	2.45	8363	111.5	9.86
J1736-44	17 36 15.32	-44 17 12.6	345.94	-6.50	6475	173	203	3.46	6579	87.7	9.80
J1736-47	17 36 46.93	-47 50 36.0	342.94	-8.45	5882	339	365	9.87	5962	79.5	10.17
J1739-51	17 39 28.78	-51 04 02.6	340.36	-10.48	3806	137	161	6.90	3677	49.0	9.59
J1741-08	17 41 21.91	-08 33 23.7	17.06	11.37	10544	253	316	4.68	10438	139.2	10.33
J1744-09	17 44 06.62	-09 21 15.3	16.70	10.38	4245	238	260	5.87	4390	58.5	9.68
J1749-15	17 49 21.58	-15 20 45.8	12.12	6.26	7454	291	426	10.02	7324	97.7	10.35
J1750-11	17 50 50.03	-11 58 16.8	15.24	7.64	4612	206	226	3.47	4640	61.8	9.50
J1753-12	17 53 59.13	-12 50 36.8	14.86	6.54	4249	232	271	6.55	4466	59.5	9.74
J1757-04	17 57 57.12	-04 03 33.2	23.10	9.96	1730	72	106	1.93	1960	26.1	8.49
J1758-04	17 58 58.23	-04 36 28.3	22.73	9.48	6172	99	150	5.24	6374	84.9	9.95
J1759-10	17 59 08.89	-10 03 51.5	17.93	6.81	11939	74	110	2.79	11734	156.4	10.21
J1800-03	18 00 17.92	-03 59 41.1	23.44	9.48	4276	227	348	12.01	4573	60.9	10.02
J1803-03	18 03 13.41	-03 01 17.9	24.66	9.30	3616	175	214	8.46	3752	50.0	9.70
J1803-06	18 03 54.74	-06 39 59.6	21.50	7.42	8893	256	302	4.49	8953	119.4	10.18
J1804-03	18 04 50.21	-03 20 03.5	24.57	8.79	1785	42	62	2.01	1914	25.5	8.49
J1807-02	18 07 12.40	-02 50 05.9	25.30	8.51	1766	146	173	36.76	1736	23.1	9.67
J1807-42	18 07 16.23	-42 49 30.6	350.03	-10.66	3238	135	161	7.73	3334	44.4	9.56
J1807-06	18 07 18.74	-06 34 21.9	21.99	6.72	3297	134	154	4.03	3298	43.9	9.26
J1807-08	18 07 40.02	-08 36 33.2	20.23	5.67	3491	187	486	28.48	3732	49.8	10.22
J1810+01	18 10 17.75	+01 36 11.4	29.64	9.88	1860	74	196	4.51	2124	28.3	8.93
J1810 –01	18 10 36.87	–01 02 25.6	27.31	8.59	2121	140	166	3.43	1955	26.0	8.74
J1812 –06	18 12 45.74	–06 20 45.3	22.83	5.63	5736	236	310	6.62	5558	74.1	9.93
J1814 –02	18 14 31.40	–02 27 10.6	26.50	7.07	1739	377	417	19.04	1946	25.9	9.48
J1814 –35	18 14 38.80	–35 28 22.8	357.32	-8.56	591	40	71	2.05	733	9.8	7.66
J1815 –02	18 15 20.32	–02 51 12.9	26.24	6.70	1790	308	340	11.46	2035	27.1	9.30
J1815 –28	18 15 30.83	–28 01 43.5	4.04	-5.26	8752	349	456	11.24	8630	115.1	10.54
J1816 –36	18 16 56.30	–36 12 54.9	356.86	-9.31	5541	248	270	5.32	5826	77.7	9.88
J1816+04	18 16 31.00	+04 25 12.4	32.91	9.78	2000	317	337	3.85	1719	22.9	8.68

Table 3.2–Continued

Source name	RA (J2000) h m s	Dec (J2000) deg ′ ″	l deg	b deg	V_{hel} km s^{-1}	W_{50} km s^{-1}	W_{20} km s^{-1}	S Jy km s^{-1}	V_{LG} km s^{-1}	D Mpc	log M_{HI} ($M_\odot$)
J1817 –04	18 17 09.62	–04 05 35.9	25.35	5.72	3080	105	146	3.59	3135	41.8	9.17
J1817 –32	18 17 31.74	–32 08 20.8	0.59	-7.56	953	85	263	3.51	1002	13.4	8.17
J1817 –03	18 17 50.94	–03 17 07.2	26.15	5.95	1873	86	107	3.38	2114	28.2	8.80
J1819 –01A	18 19 02.93	–01 07 20.8	28.22	6.68	2965	172	196	5.41	2981	39.7	9.30
J1819+01	18 19 20.68	+01 10 16.8	30.30	7.67	2582	113	141	10.02	253	33.8	9.43
J1819 –01B	18 19 47.87	–01 38 50.3	27.83	6.28	3051	190	221	7.19	3177	42.4	9.48
J1820+07	18 20 33.25	+07 55 32.6	36.55	10.45	3704	303	341	21.91	3847	51.3	10.13
J1822 –35	18 22 38.90	–35 39 19.9	357.9	-10.09	5604	542	575	22.68	5661	75.5	10.48
J1823+03	18 23 04.87	+03 24 07.5	32.74	7.86	8791	63	89	2.50	8790	117.2	9.91
J1823+00	18 23 23.65	+00 16 30.2	29.97	6.36	2910	130	149	11.10	2613	34.8	9.50
J1824 –34	18 24 25.69	–34 12 09.8	359.38	-9.77	4901	335	360	5.58	4634	61.8	9.70
J1824 –01A	18 24 31.71	–01 55 36.9	28.13	5.10	6204	200	226	6.47	6220	82.9	10.02
J1824 –01B	18 24 59.59	–01 27 41.0	28.60	5.21	2865	354	382	27.31	2819	37.6	9.96
J1826+03	18 26 37.54	+03 04 25.7	32.85	6.92	2956	80	130	3.70	3195	42.6	9.20
J1826+01	18 26 38.55	+01 33 33.9	31.49	6.23	2764	143	166	4.03	2786	37.1	9.12
J1826 -33	18 26 47.59	–33 43 19.7	0.04	-10.01	5900	315	380	11.43	5890	78.5	10.22
J1827+04	18 27 53.34	+04 07 14.0	33.93	7.11	2107	75	172	1.88	2226	29.7	8.59
J1828+02	18 28 22.36	+02 44 01.1	32.74	6.38	6670	48	152	2.92	6959	92.8	9.77
J1828 –33	18 28 27.42	–33 10 44.7	0.69	-10.08	721	49	87	2.47	569	7.6	7.53
J1829+01	18 29 42.86	+01 41 26.6	31.96	5.60	10313	99	139	3.25	10434	139.1	10.17
J1830 –27	18 30 37.15	–27 49 21.9	5.77	-8.13	8114	114	179	5.48	8154	108.7	10.18
J1831 –31	18 31 57.80	–31 45 24.2	2.32	-10.12	5992	426	462	12.65	5823	77.6	10.25
J1833+03	18 33 27.36	+03 35 14.8	34.08	5.63	5257	244	265	5.98	5366	71.5	9.86
J1834 –30	18 34 19.14	–30 45 42.3	3.45	-10.15	440	45	74	3.79	509	6.8	7.61
J1836 –20	18 36 14.77	–20 00 19.7	13.39	-5.77	1668	54	73	2.53	1859	24.8	8.56
J1839 –17	18 39 25.42	–17 33 31.5	15.92	-5.34	10791	207	416	7.51	10753	143.4	10.56
J1841 –18	18 41 18.08	–18 59 48.9	14.83	-6.39	1670	159	181	15.16	1899	25.3	9.36
J1846 –23	18 46 42.93	–23 05 37.9	11.68	-9.32	9147	79	99	2.33	9379	125.1	9.93
J1856 -16	18 56 11.85	–16 36 13.0	18.57	-8.51	8953	172	218	4.82	9003	120.0	10.21
J1859 –10	18 59 10.95	–10 03 13.3	24.82	-6.27	10212	302	376	5.05	10121	134.9	10.34
J1901 –04	19 01 49.81	–04 29 21.5	30.11	-4.35	1525	131	164	17.17	1627	21.7	9.28
J1909 –05	19 09 40.23	–05 05 48.6	30.45	-6.37	8811	269	337	4.44	8566	114.2	10.13
J1917 –00	19 17 41.13	–00 39 43.4	35.34	-6.14	11339	284	333	6.10	11129	148.4	10.50
J1922 –05	19 22 10.28	–05 31 14.7	31.48	-9.34	9340	426	445	5.24	9320	124.3	10.28
J1923 –01	19 23 33.52	–01 37 57.6	35.15	-7.89	10095	163	235	4.68	10101	134.7	10.30

The columns of Table 3.3 contain the following information: Column 1: The name of the cube where the galaxy is found;
Column 2: Source name;
Columns 3 & 4: Equatorial coordinates (J2000) of the candidate;
Columns 6 & 7: Galactic coordinates;
Column 8: Heliocentric velocity;
Column 9 & 8: Velocity width at 50%, and at 20% of the peak flux density;
Column 10: Integrated HI flux;
Column 11: Velocity corrected to the LG rest frame;
Column 12: Distance to the galaxy candidate;
Column 13: Logarithm of the HI mass.

Table 3.3: Doubly detected GB extension galaxies

Cube name	Source name	RA (J2000) h m s	Dec (J2000) deg ′ ″	l deg	b deg	V_{hel} km s^{-1}	W_{50} km s^{-1}	W_{20} km s^{-1}	S Jy km s^{-1}	V_{LG} km s^{-1}	D Mpc	log M_{HI} ($M_\odot$)
Z344N_20	J1610-38	16 10 31.28	−38 20 26.0	340.33	9.66	4503	142	179	4.83	4251	56.7	9.56
Z336N_20	J1610-38*	16 10 25.00	−38 21 33.3	340.30	9.67	4478	118	191	6.68	4231	56.4	9.70
Z336N_20	J1616-40	16 16 07.96	−40 02 04.3	339.93	7.69	4438	344	378	15.71	4466	59.6	10.12
Z344N_20	J1616-40*	16 16 16.46	−40 03 59.3	339.93	7.65	4439	337	369	13.40	4475	59.7	10.05
Z344N_20	J1620-39	16 20 30.47	−39 36 24.3	340.84	7.40	2380	88	113	7.54	2510	33.5	9.30
Z336N_20	J1620-39*	16 20 14.19	−39 36 04.7	340.81	7.44	2382	78	102	8.15	2500	33.3	9.33
Z344N_20	J1624-42	16 24 52.51	−42 26 43.7	339.38	4.83	2222	165	215	22.58	2225	29.7	9.67
Z336N_20	J1624-42*	16 24 48.87	−42 28 05.0	339.36	4.82	2219	166	200	18.97	2221	29.6	9.59
Z344N_20	J1649-35	16 49 40.43	−35 10 08.8	348.06	6.08	3526	189	218	9.70	3704	49.4	9.75
Z352N_20	J1649-35*	16 49 57.16	−35 10 25.7	348.09	6.03	3520	1867	210	5.86	3689	49.2	9.52
Z352N_20	J1654-35	16 54 04.36	−35 34 46.5	348.31	5.12	6365	179	270	11.78	6412	85.5	10.31
Z344N_20	J1653-35*	16 53 59.76	−35 30 28.4	348.36	5.18	6364	154	270	11.52	6412	85.5	10.30
Z344S_20	J1711-47	17 11 40.04	−47 35 35.0	340.78	−4.79	2190	232	278	20.51	2214	29.5	9.62
Z336S_20	J1711-47*	17 11 51.35	−47 35 11.4	340.80	−4.81	2190	231	256	27.26	2221	29.6	9.75
Z344S_20	J1727-49	17 27 46.40	−49 26 37.3	340.76	−8.04	3940	208	233	9.38	3885	51.8	9.77
Z336S_20	J1727-49*	17 27 49.03	−49 23 55.9	340.80	−8.02	3935	227	291	13.96	3885	51.8	9.95
Z344S_20	J1739-51	17 39 28.78	−51 04 2.6	340.36	-10.48	3806	137	161	6.90	3677	49.0	9.59
Z336S_20	J1739-51*	17 39 25.58	−51 02 37.0	340.38	−10.46	3804	118	147	6.80	3670	48.9	9.58
Z024N_20	J1807-08	18 07 35.80	−08 37 48.4	20.20	5.67	3467	228	271	23.16	3707	49.4	10.12
Z016N_20	J1807-08*	18 07 40.02	−08 36 33.2	20.22	5.66	3491	187	486	28.48	3732	49.8	10.22
Z032N_20	J1819-01A	18 19 02.93	−01 07 20.8	28.22	6.68	2965	172	196	5.41	2981	39.7	9.30
Z024N_20	J1819-01*	18 19 10.19	−01 11 08.8	28.17	6.62	2974	168	202	6.49	3002	40.0	9.39
Z032N_20	J1824-01B	18 24 59.59	−01 27 41.0	28.60	5.20	2865	354	382	27.31	2819	37.6	9.96
Z024N_20	J1825-01*	18 25 05.93	−01 26 48.3	28.62	5.19	2867	345	364	31.14	2819	37.6	10.02
Z008S_21	J1846-23	18 46 42.93	−23 05 37.9	11.67	-9.32	9147	79	99	2.33	9379	125.1	9.93
Z016S_20	J1846-23*	18 46 48.19	−23 05 27.6	11.68	−9.33	9143	89	110	3.38	9373	125.0	10.09

* Galaxies that are found outside of the region, $\Delta l = \pm 4^\circ$ of the data cube.

3.3 Accuracy of HI Parameters

To evaluate the accuracy of the measured HI parameters: position, velocity and integrated flux of the GB extension galaxies, comparisons were made with a) the HI parameters of the GB extension candidates that are detected twice b) corresponding candidates found from the existing independent search of 8 of the data cubes, and c) with the HI parameters of the galaxies also found in HIPASS.

3.3.1 Positional Accuracy

A positional comparison was made between the candidates that were detected twice. Fig. 3.2 shows the comparison between the position of the 13 doubly detected candidates, where RA_1 and Dec_1 are the RA and Dec of the candidate found within the well-defined region of a cube (i.e., within $\Delta l = \pm 4°$ of central longitude), RA_2 and Dec_2 are the RA and Dec of the corresponding candidate in the neighbouring cubes ($\Delta l > \pm 4°$) respectively. The position of each candidate is found to be almost a perfect match with the corresponding candidate. The mean offset and corresponding standard deviation for the RA and Dec measurements of the 13 doubly detected candidates are:

$$\Delta\text{RA} = 0.39 \text{ arcmin}, \sigma = 1.56 \text{ arcmin}$$

and

$$\Delta\text{Dec} = 0.32 \text{ arcmin}, \sigma = 2.04 \text{ arcmin}$$

The difference between the measured positions of the candidates is quite small, actually less than the $4'$ pixel size of the data cubes.

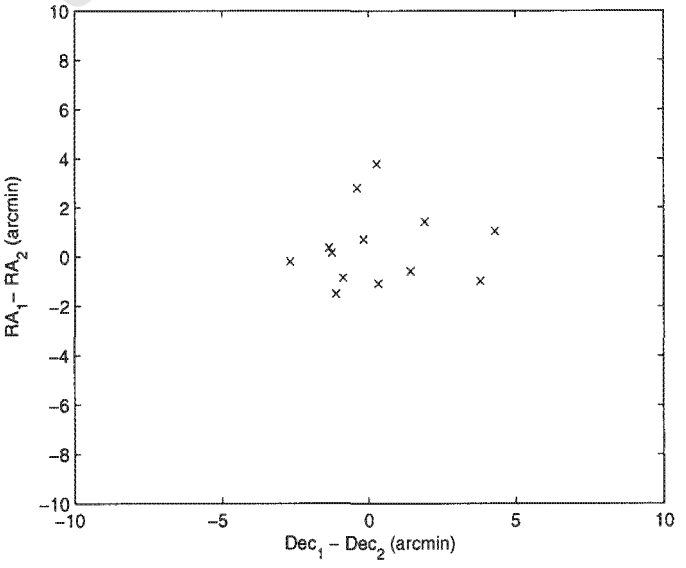

Figure 3.2: The offset in RA and Dec for the the 13 doubly detected GB extension candidates.

The positional comparison with the corresponding HI parameters obtained from the independent search made by P. Buckland while at the University of Western Australia is shown in Fig. 3.3, where RA_{uct} and Dec_{uct} are the RA and Dec of the candidates obtained from my search, whereas RA_{uwa} and Dec_{uwa} are the RA and Dec of the corresponding candidate in the list made by the second searcher. Although the comparison was made only for half of the data, i.e., over the longitude range of 336° to 0°, it will provide a good indication of the quality of the measurements made for all data cubes. The mean offset and standard deviation for the RA and Dec measurements of the 91 candidates found in the 8 data cubes searched by both of us are:

$$\Delta\text{RA} = 0.16 \text{ arcmin}, \sigma = 1.12 \text{ arcmin}$$

and

$$\Delta\text{Dec} = 0.05 \text{ arcmin}, \sigma = 0.99 \text{ arcmin}$$

The results show a very good agreement between the measurements of the two lists. It is actually better than the previous comparison of double detections, which is understandable as the latter galaxies always lie outside of the well-defined region of the data cube, hence the measuremnts have larger uncertainity.

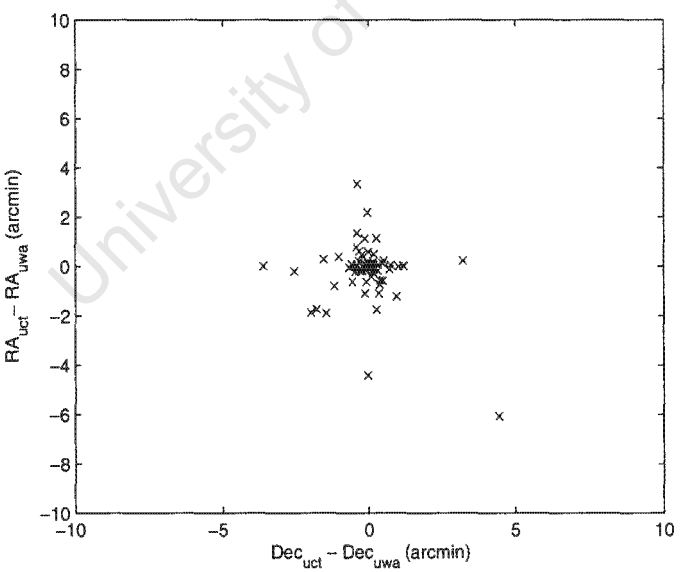

Figure 3.3: The difference in positions, RA and Dec, for the two independent measurements of galaxies of the GB extension candidates.

The accuracy in measuring the position of the GB detections was also compared with values found in the HIPASS Catalog (HICAT) (Meyer et al., 2004) for 29 common detections, mostly nearby galaxies due to the lower sensitivity of HIPASS. The difference in position between the HIPASS galaxies and the GB extension detections is shown in Figure 3.4, where RA_{GB} and Dec_{GB} are the RA and Dec of the GB extension candidates, and RA_{HIPASS} and

$\mathrm{Dec_{HIPASS}}$ are the RA and Dec of the HIPASS counterparts for the GB extension candidates respectively. A satisfactory agreement for the measurements of the HI position is found with a mean offset and corresponding standard deviation of

$$\Delta\mathrm{RA} = 0.31 \text{ arcmin}, \sigma = 2.03 \text{ arcmin}$$

and

$$\Delta \text{ Dec} = 0.61 \text{ arcmin}, \sigma = 2.22 \text{ arcmin}$$

This compares well to the HIPASS positional error of ~3 arcmin (Barnes et al., 2001).

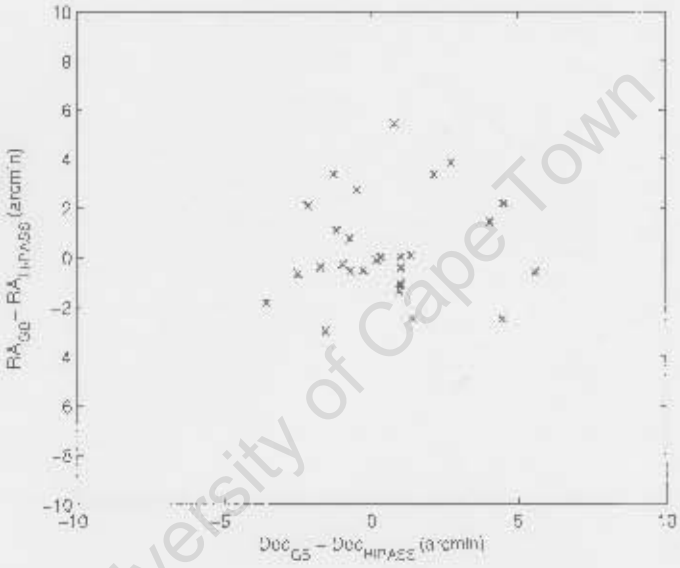

Figure 3.4: The difference in positions, RA and Dec, for the GB extension candidates and their HIPASS counterparts.

3.3.2 Accuracy in Measuring V_{hel}

The comparison between the heliocentric velocities of the 13 doubly detected candidates is given in Fig. 3.5 where V_1, the heliocentric velocity of a candidate found within the well defined region of the cube, is plotted against the difference between V_1 and the heliocentric velocity of the corresponding candidate in the neighboring cube. The mean offset and standard deviation are:

$$\Delta V = -2.75 \text{ km s}^{-1}, \sigma = 11.8 \text{ km s}^{-1}$$

Applying a linear-least square method, the following equation

$$\Delta V = (0.0004 \pm 0.0002)V_1 - (4.39 = 8.45) \text{ km s}^{-1}$$

can be fitted to the data, with a standard deviation of 12.3 km s^{-1}, confirming that the two velocities match very well and there seems to be no significant trend.

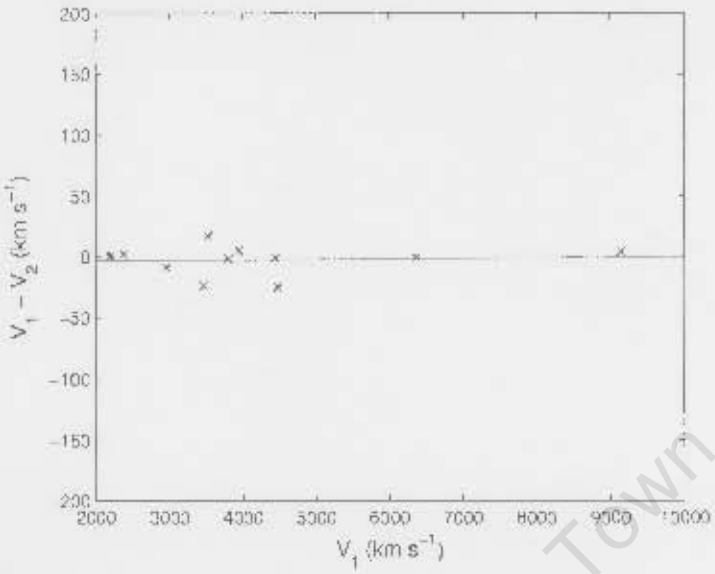

Figure 3.5: The difference between the heliocentric velocities of the GB extension candidates detected in adjacent data cubes. The agreement between the two measurements is excellent.

In Fig. 3.6 the difference in heliocentric velocities of the galaxies identified by the second searcher is illustrated with mean offset and standard deviation of

$$\Delta V = -12.1 \text{ km s}^{-1}, \text{ and } \sigma = 26.9 \text{ km s}^{-1}$$

A line with equation

$$\Delta V = (-0.0016 \pm 0.0014) V_{\rm hel} - (4.8 \pm 7.8) \text{ km s}^{-1}$$

was fitted to the values, with a standard deviation of 26.7 km s^{-1}. No significant trend is seen, although the scatter is a bit larger compared to the previous comparison of doubly detected galaxies.

The comparison of the GB galaxies velocities with HIPASS shows a similar behaviour despite the difference in depth of the two surveys. This is shown in Fig. 3.7. The mean offset and standard deviation are:

$$\Delta V = -4.1 \pm 2.2 \text{ km s}^{-1}, \sigma = 28.8 \text{ km s}^{-1}$$

A line with equation

$$\Delta V = (0.0006 \pm 0.002) V_{\rm GB} - (4.7 + 2.11) \text{ km s}^{-1}$$

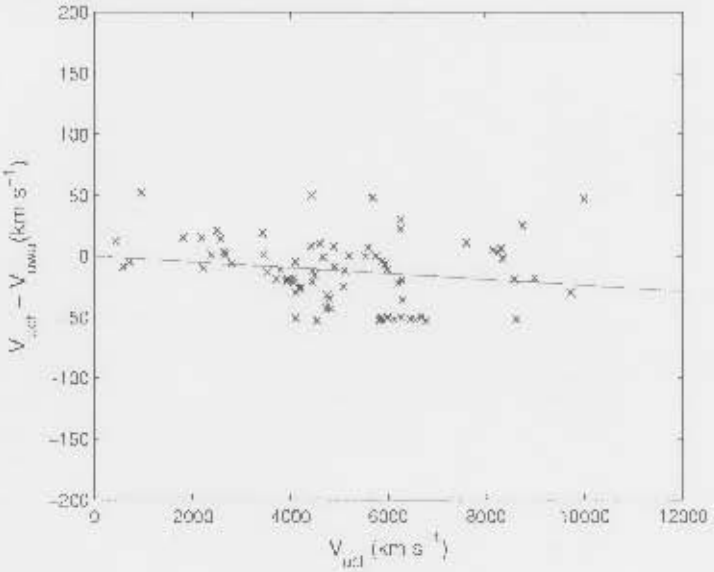

Figure 3.6: The difference between heliocentric velocities of the candidates from the two independent searches. The scatter is very low compared to velocity pixel.

was fitted to the data, with a standard deviation of 29.3 km s^{-1}.

3.3.3 Accuracy in Measuring S_{int}

As a further check on the accuracy of the measured HI parameters of the GB extension galaxies, a comparison was made between the measured integrated flux of doubly detected candidates. Figure 3.8 shows the result of the comparison, where S_1 and S_2 are the integrated fluxes for the galaxies found in the well defined region of the cube and the corresponding integrated flux of the candidated in the neighbouring cube respectively. The mean offset and standard deviation are:

$$\Delta S_{int} = 1.18 \text{ Jy km s}^{-1}, \sigma = 3.27 \text{ Jy km s}^{-1}$$

A linear regression yields

$$S_{2int} = (1.27 \pm 0.13) S_{2int} - (2.00 + 1.71) \text{ Jy km s}^{-1}$$

This has a standard deviation of 2.85 Jy km s^{-1}. The observed larger scatter is because these galaxies (with S_{2int}) are close or outside the border of the data cube. Hence, they have larger uncertainties. This evident in the higher flux measurements for S_{2int} compared to S_{1int} due to higher noise in S_{2int}.

The comparison of integrated flux obtained from the two independent searches is shown in Fig. 3.9. The mean offset and corresponding standard deviation are:

$$\Delta S_{int} = 0.85 \text{ Jy km s}^{-1}, \sigma = 0.84 \text{ Jy km s}^{-1}$$

A straight line with equation

$$S_{int\,\mathrm{uwa}} = (0.99 \pm 0.015) S_{int\,\mathrm{uct}} - (0.021 \pm 0.15) \text{ Jy km s}^{-1}$$

was fitted to the values, with a standard deviation of 0.85 Jy km s^{-1}, which is not significantly different from the scatter and the mean offset.

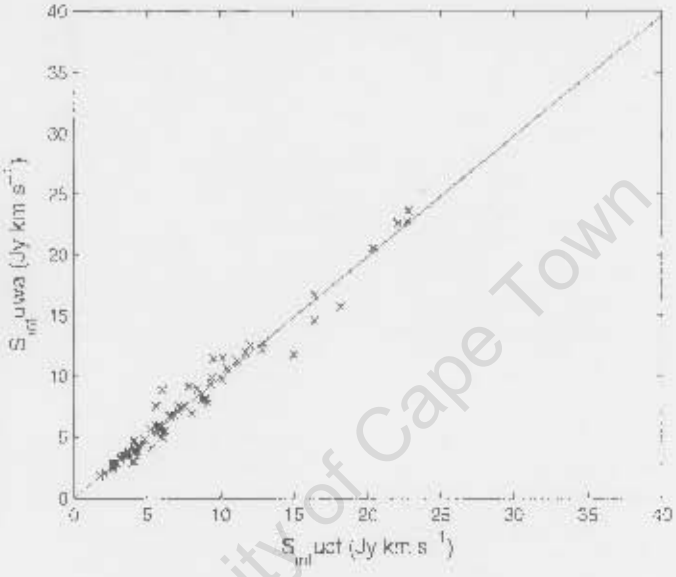

Figure 3.9: Integrated flux measured for the GB candidates obtained from independent searches. A very good agreement is observed between the two measurements.

Lastly Fig. 3.10 displays the comparison of the integrated flux from the GB extension versus HIPASS. The GB extension contains sources with peak flux density lower than HIPASS, which is expected as the survey has better sensitivity. The mean offset and standard deviation of

$$\Delta S_{int} = 0.86 \text{ Jy km s}^{-1}, \sigma = 2.9 \text{ Jy km s}^{-1}$$

The linear regression

$$S_{int\,\mathrm{HIPASS}} = (0.89 \pm 0.08) S_{int\,\mathrm{GB}} + (2.02 + 0.98) \text{ Jy km s}^{-1}$$

has a standard deviation of 2.9 Jy km s^{-1}. No trend is observed except a larger scatter due to higher noise levels in HIPASS.

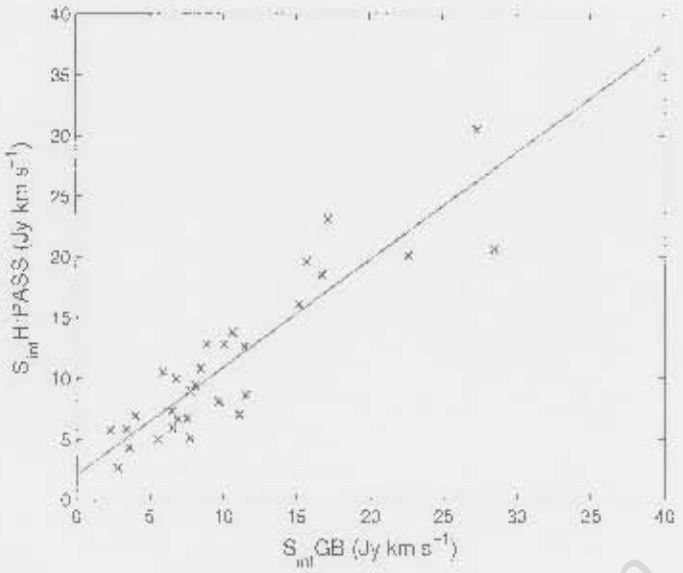

Figure 3.10: Integrated flux from the GB extension and HIPASS surveys. The observed larger scatter is due to higher noise levels in HIPASS data.

3.4 Multiwavelength Counterparts

3.4.1 Counterpart Search

For every GB extension detection, a counterpart search has been made in HICAT (Meyer et al., 2004; Wong et al., 2006) and NASA's Extragalactic Database (NED). The search used both position and velocity information to identify detections within a search radius of 8′ for HI and $\sim$ 4′ for optical and infrared counterparts. In the optical and infrared cases all possible counterparts were visually inspected for their morphology to determine the most likely counterpart. For 65 of our galaxies, multiwavelength counterparts listed in NED with matching redshifts were found. The majority of these galaxies matched to a single counterpart. Sixteen, optical and infrared, galaxies had a catalogued galaxy within the search radius, but had no redshift information available. However, based on their separation and morphology, they are listed as possible counterparts. In Table 3.5 the results of the counterpart search is presented.

In summary, 30 of the 158 candidates have HI counterparts, 29 HIPASS (Meyer et al., 2004; Wong et al., 2006) and 1 HIZSS (Henning et al., 2000). Twenty-two have 2MASS counterparts (Jarrett et al., 2000a), 3 have IRAS counterparts (IRAS PSC;Joint IRAS Science Working Group 1988) and 24 have optical counterparts, ESO (Lauberts, 1982) and UGC (Nilson, 1973).

The spatial distribution of galaxies with multiwavelength counterparts is shown in Fig. 3.12, where solid triangle represent galaxies with both optical and infrared counterparts, open triangles represent galaxies with infrared counterparts only, and open squares represent galaxies with optical counterparts only. Galaxies with with HI counterparts are shown as solid circles while galaxies with no counterparts are given as open circles. Extinction countours of

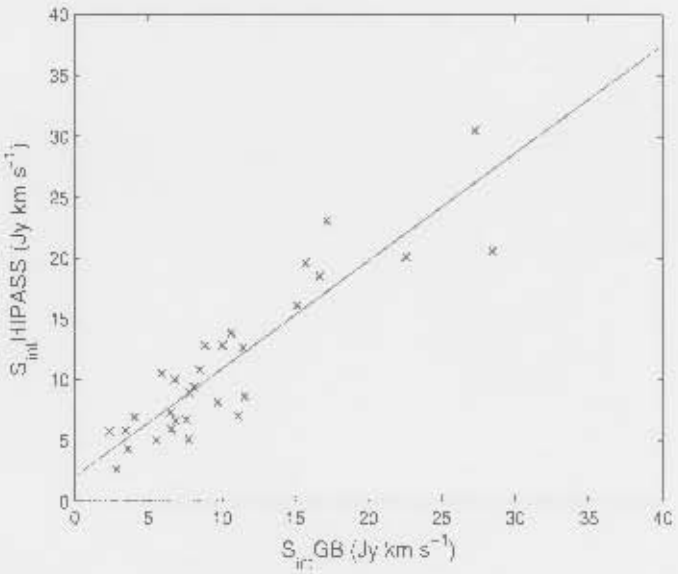

Figure 3.10: Integrated flux from the GB extension and HIPASS surveys. The observed larger scatter is due to higher noise levels in HIPASS data.

3.4 Multiwavelength Counterparts

3.4.1 Counterpart Search

For every GB extension detection, a counterpart search has been made in HICAT (Meyer et al., 2004; Wong et al., 2006) and NASA's Extragalactic Database (NED). The search used both position and velocity information to identify detections within a search radius of 8′ for HI and ∼ 4′ for optical and infrared counterparts. In the optical and infrared cases all possible counterparts were visually inspected for their morphology to determine the most likely counterpart. For 65 of our galaxies, multiwavelength counterparts listed in NED with matching redshifts were found. The majority of these galaxies matched to a single counterpart. Sixteen, optical and infrared, galaxies had a catalogued galaxy within the search radius, but had no redshift information available. However, based on their separation and morphology, they are listed as possible counterparts. In Table 3.5 the results of the counterpart search is presented.

In summary, 30 of the 158 candidates have HI counterparts, 29 HIPASS (Meyer et al., 2004; Wong et al., 2006) and 1 HIZSS (Henning et al., 2000). Twenty-two have 2MASS counterparts (Jarrett et al., 2000a), 3 have IRAS counterparts (IRAS PSC;Joint IRAS Science Working Group 1988) and 24 have optical counterparts, ESO (Lauberts, 1982) and UGC (Nilson, 1973).

The spatial distribution of galaxies with multiwavelength counterparts is shown in Fig. 3.12, where solid triangle represent galaxies with both optical and infrared counterparts, open triangles represent galaxies with infrared counterparts only, and open squares represent galaxies with optical counterparts only. Galaxies with with HI counterparts are shown as solid circles while galaxies with no counterparts are given as open circles. Extinction countours of

$A_B = 1^{mag}$ and 3^{mag} from DIRBE/IRAS data (Schlegel et al., 1998) are superposed on the plot.

Surprisingly, there were six HIPASS galaxies that were not recovered in this deeper HI survey (J1652-29, J1704-29, J1756-05, J1802-39, J1809-05, and J1912-03). These were followed up by a renewed inspection of the position of the galaxies in the relevant GB extension data cubes as well as on the Online Digitized Sky Survey (DSS2) images. The HI parameters of these galaxies are given in Table 3.4 as presented in HICAT. Their HI spectra from the HIPASS Public Data Relase is shown in Fig. 3.11 together with the corresponding spectrum found in our GB data cubes search. From our close inspection of the spectrum around these galaxies the following conclusions have been made:

HIPASS J1652-29

- HI Spectrum: a narrow peak is visible in HIPASS. Various negative peaks of equal strength are also visible in the spectrum. The HIPASS signal at $V = 5784$ and $\Delta V \approx 130$ km s^{-1}, is not recovered in the GB extension. Moreover, nothing is visible in DSS except the heavy star crowding in the region.
- Conclusion: "False" detection.

HIPASS J1704-29

- HI Spectrum: shows a narrow peak $V \sim 5800$ and $\Delta V \approx 150$ km s^{-1} in both HIPASS and GB extension. The signal is still too weak in the GB extension for it to be classified as a likely galaxy candidate. Nothing is seen on DSS2.
- Conclusion: it could be classified as a probable galaxy.

HIPASS J1756-05

- HI Spectrum: the signal $V = 9173$ and $\Delta V \approx 250$ km s^{-1} is not clear except the wiggly baseline in both cases.
- Conclusion:"False" detection.

HIPASS J1802-39

- HI Spectrum: this $V = 552$ and $\Delta V \approx 220$ km s^{-1} is not convincing in HIPASS. Looking at the spectrum in the GB extension it could be top ripple. Nothing is seen on DSS2 either, except the heavy star crowding.
- Conclusion:"False" detection.

HIPASS J1809-05

- HI Spectrum: no peak is visible in both cases for the HIPASS galaxy at $V = 2933$ km s^{-1}.
- Conclusion:"False" detection.

HIPASS J1912-03

- HI Spectrum: a narrow peak is visible at $V = 5755$ and $\Delta V \approx 300$ km s^{-1} in HIPASS which could probably be a galaxy. A weak signal is confirmed by the GB extension data. Moreover, on DSS2 red, a clear face-on spiral galaxy is visible.
- Conclusion:"Real" detection.

The general conclusion is that, of the six HIPASS galaxies one is "Real" detection, and one could be possible galaxy. The rest seem to be "false" detections.

Table 3.4: HI parameters of the six HIPASS galaxies

HIPASS Name	RA (J2000)	Dec (J2000)	l deg	b deg	V_{hel} (km s^{-1})	$W_{50\%}$ (km s^{-1})	$W_{20\%}$ (km s^{-1})	S (Jy km s^{-1})	
J1652–29	16 52 10.5	–29 28 35	352.8645	9.2569	5784	96.5	110.0	2.4	(f)
J1704–29	17 04 48.3	–29 49 53	354.2731	6.8673	5794	78.3	129.5	7.6	(p)
J1756–05	17 56 41.2	–05 12 29	21.9227	9.6913	9173	208.3	283.8	13.1	(f)
J1802–39	18 02 38.1	–39 37 13	352.4872	–8.3892	552	129.3	222.9	6.0	(f)
J1809–05	18 09 46.5	–05 50 40	22.9254	6.5248	2933	191.6	320.0	6.6	(f)
J1912–03	19 12 27.8	–03 57 01	31.7994	-6.4739	5755	230.0	293.8	8.6	(r)

(f) false, (p), possible and (r) real detections.

Table 3.5 which lists the possible multiwavelength counterparts contains the following information:

Column 1: Source name;

Column 2 & 3: Equatorial coordinates (J2000) ;

Column 4: Extinction, $E(B-V)$, from DIRBE/IRAS 100 μ m extinction maps (Schlegel et al., 1998);

Column 5: Possible HI counterpart registered in NED;

Column 6,9,12: Offset between the position of the GB candidate and the counterpart;

Column 7,10,13: The difference in velocity, $\triangle V = V_{GB} - V_{counterpart}$;

Column 8: Possible optical counterpart as given in NED;

Column 11: Possible 2MASS counterpart as given in NED;

Column 14: Possible IRAS counterpart as given in NED.

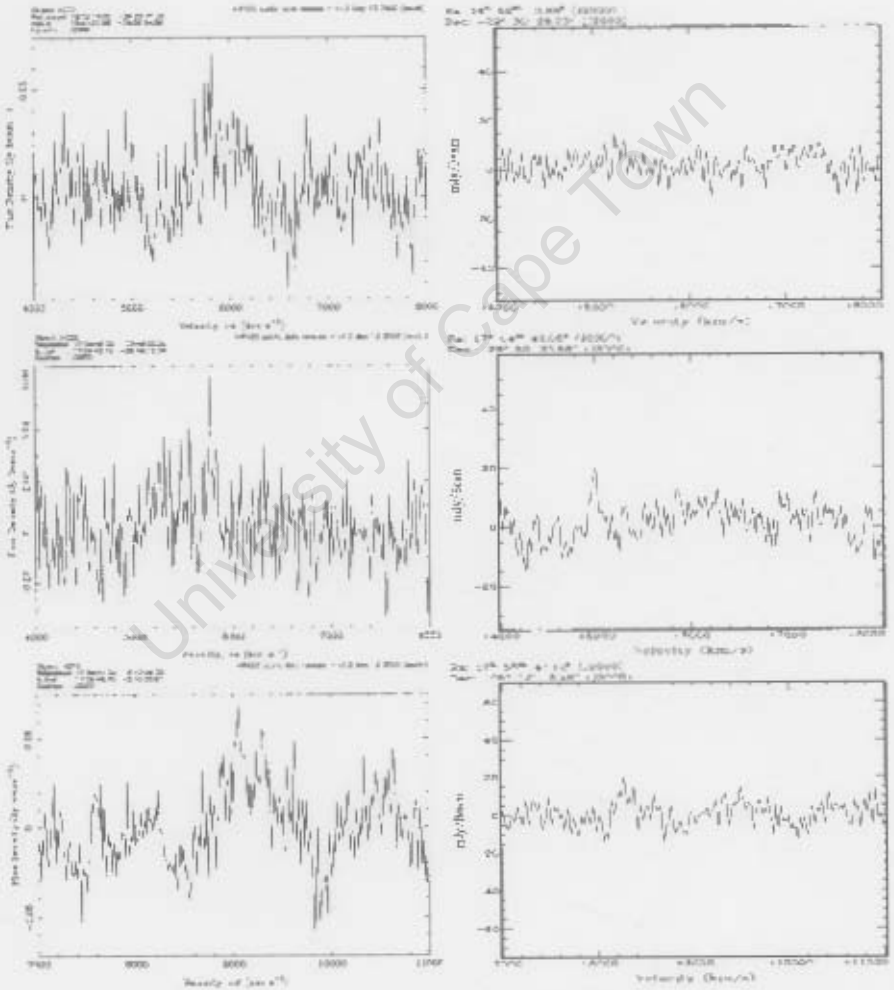

Figure 3.11: The HI spectra of the six HIPASS galaxies that were not identified in the GB extension survey. The left panels shows HI spectrum from HIPASS data, whereas the right panels present the corresponding spectrum from the GB extension data.

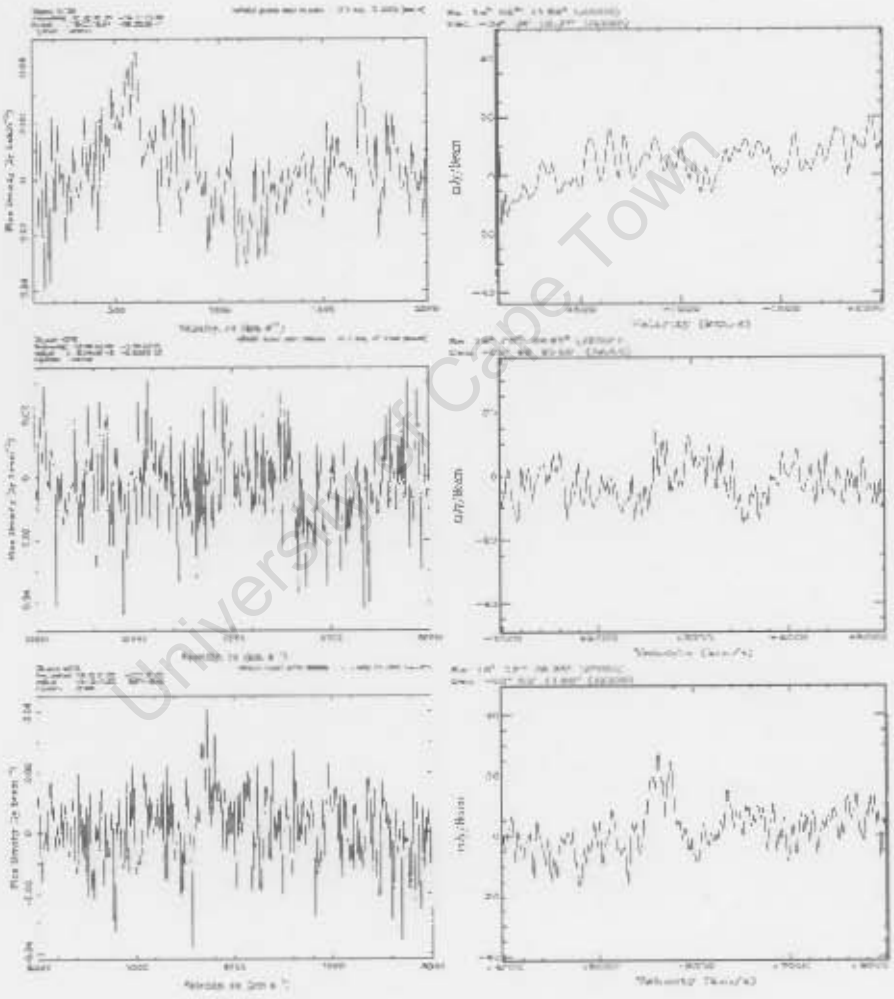

Figure 3.11– Continued

Table 3.5: Possible Multiwavelength Counterparts

Source name	RA. (J2000)	Dec. (J2000)	$E(B-V)$	HI	Sep. (arcmin)	Optical	Sep. (arcmin)	2MASX	Sep. (arcmin)	IRAS	Sep. (arcmin)
J1538-44	15 38 23.17	−44 26 33.5	0.35	...	...	ESO 274- G 019	2.3	J15382201-4427568*	1.4	...	...
J1546-42	15 46 53.12	−42 21 20.1	0.34	...	...	ESO 329- G 019	1.8	...	...	...	...
J1549-46	15 49 16.21	−46 50 07.6	0.64	HIPASS J1548-46	4.8	...	...	...	5.3	...	...
J1556-42	15 56 57.62	−42 34 10.8	0.87	HIPASS J1557-42	1.4	...	...	J15565765-4234517*	0.7	...	...
J1616-40	16 16 07.96	−40 02 04.3	0.99	HIPASS J1616-40	1.1	...	...	J16161676-4003142*	2.0	...	...
J1620-39	16 20 30.47	−39 36 24.3	0.84	HIPASS J1620-39	4.7	...	...	...	...	...	...
J1621-36	16 21 06.14	−36 08 38.4	0.65	...	...	ESO 390- G 004	0.9	...	...	...	...
J1624-42	16 24 52.51	−42 26 43.7	1.22	HIPASS J1624-42	2.9	...	...	...	...	...	...
J1628-29	16 28 05.26	−29 06 23.6	0.44	...	...	ESO 452- G 003	1.0	...	...	...	...
J1630-30	16 30 16.37	−30 33 46.2	0.36	...	...	ESO 452- G 004	2.2	J16300522-3033542	2.4	...	...
J1631-28	16 31 46.53	−28 05 53.7	0.64	...	...	ESO 452- G 005	1.4	J16313752-2805243*	2.0	...	...
J1632-28	16 32 04.22	−28 05 32.3	0.67	...	...	ESO 452- G 007	1.7	...	...	...	...
J1632-29B	16 32 46.45	−29 23 08.1	0.48	...	...	ESO 452- G 008	2.2	...	...	...	...
J1635-33	16 35 33.26	−33 46 56.5	0.51	HIPASS J1635-33	1.8	...	...	...	...	...	...
J1636-26	16 36 10.38	−26 10 22.7	0.52	...	...	ESO 517- G 011	1.9	J16360656-2610126*	0.9	...	...
J1639-28	16 39 05.99	−28 57 37.5	0.38	...	...	ESO 452- G 010	1.4	J16390239-2901289*	4.2	...	...
J1642-37	16 42 45.70	−37 31 42.3	0.86	HIPASS J1642-37	3.5	...	...	...	...	...	...
J1643-30	16 43 13.93	−30 56 16.2	0.42	...	...	ESO 452- G 014	0.9	...	4.8	...	
J1644-55	16 44 27.04	−55 29 49.7	0.35	...	...	ESO 179- G 012	0.8	J16441750-5529172*	1.4	16406-5525*	2.6
J1649-35	16 49 40.43	−35 10 08.8	0.93	HIPASS J1649-35	0.9	...	...	...	...	...	....
J1652-28	16 52 09.15	−28 19 27.8	0.28	...	...	ESO 453- G 007	1.6	...	...	...	...
J1658-21A	16 58 02.90	−21 17 54.0	0.28	...	...	ESO 586- G 006	1.7	...	...	...	...
J1658-32	16 58 57.05	−32 40 53.1	0.47	HIPASS J1658-32	1.7	...	...	...	...	...	...
J1702-27	17 02 25.98	−27 50 11.7	0.33	...	...	ESO 453- G 015	1.8	J17023181-2750389*	1.4	...	...
J1702-52	17 02 20.06	−52 50 55.7	0.39	HIPASS J1702-52	3.0	WKK 7863[c]	1.8	...	...	...	...
J1705-29	17 05 35.71	−29 41 43.8	0.43	HIPASS J1705-29	2.4	...	...	...	...	...	...
J1705-24	17 05 59.16	−24 43 10.5	0.42	...	...	...	...	J1705573-244055*	2.3	...	...
J1706-21	17 06 35.27	−21 19 20.4	0.52	...	...	...	...	J17063120-2117314	3.6	...	...
J1708-25	17 08 25.54	−25 45 16.2	0.46	...	...	ESO 519- G 003	2.7	J17082540-2543541*	1.4	...	...
J1711-47	17 11 40.04	−47 35 35.0	0.71	HIPASS J1711-47[a]	0.9	...	...	...	...	...	...
J1712-15	17 12 27.60	−15 06 35.7	0.39	...	...	...	...	J17122939-1503328	3.1	...	...
J1712-25	17 12 01.08	−25 46 44.3	0.49	...	...	ESO 519- G?009	4.1	...	...	...	...
J1716-15	17 16 27.88	−15 45 04.0	0.37	...	...	...	...	J1716205-154249[2]	2.8	...	...
J1720-15	17 20 48.22	−15 40 09.8	0.45	...	...	...	...	J17205126-1540542	1.0	...	...
J1723-45	17 23 25.27	−45 28 31.4	0.48	HIPASS J1723-45	4.0	...	...	...	...	...	...
J1726-14	17 26 28.34	−14 27 37.9	0.53	...	...	...	...	J17262140-1426537	1.8	...	...
J1727-49	17 27 46.40	−49 26 37.3	0.23	...	...	ESO 228- G?004	0.5	...	...	...	...
J1729-11	17 29 51.99	−11 02 36.6	0.57	...	...	...	...	J17293946-1105308	4.2	...	...
J1732-43	17 32 21.21	−43 15 28.3	0.55	HIPASS J1732-43	1.0	...	...	...	...	17289-4313	1.8
J1733-09	17 33 18.71	−09 33 00.8	0.87	...	...	...	...	J17332166-0929143	3.8	...	...

Table 3.5–Continued

Source name	RA. (J2000)	Dec. (J2000)	$E(B-V)$	HI	Sep. (arcmin)	Optical	Sep. (arcmin))	2MASX	Sep. (arcmin)	IRAS	Sep. (arcmin)
J1739-51	17 39 28.78	–51 04 02.6	0.17	HIPASS J1739-51	3.1	...	...	...	...	...	...
J1744-09	17 44 6.62	–09 21 15.3	0.87	HIPASS J1743-09	2.5	...	...	J17440232-0921440*	1.2	...	...
J1803-03	18 03 13.41	–03 01 17.9	1.52	HIPASS J1803-02	4.1	...	...	...	1.4	...	...
J1804-03	18 04 50.21	–03 20 03.5	1.85	HIPASS J1805-03	5.8	...	...	...	...	...	...
J1807-42	18 07 16.23	–42 49 30.6	0.11	HIPASS J1806-42	6.1	...	...	...	...	...	...
J1807-02	18 07 12.40	–02 50 05.9	1.61	...	...	...	...	J18071027-0249517	0.6	...	...
J1807-06	18 07 18.74	–06 34 21.9	1.57	HIPASS J1807-06	3.2	...	...	...	...	...	...
J1807-08	18 07 40.02	–08 36 33.2	1.36	HIPASS J1807-08	0.3	...	...	...	...	...	...
J1810+01	18 10 17.75	+01 36 11.4	0.43	...	...	UGC 1113	1.4	...	...	...	...
J1810-01	18 10 36.87	–01 02 25.6	1.15	HIPASS J1810-01	4.8	...	...	...	...	...	...
J1814-02	18 14 31.40	–02 27 10.6	2.05	...	...	...	...	J18142795-0225052	2.3	...	...
J1815-02	18 15 20.32	–02 51 12.9	2.20	HIPASS J1815-02	3.6	...	...	...	...	18128-0254*	3.5
J1817-04	18 17 09.62	–04 05 35.9	1.31	HIPASS J1817-04	1.5	...	...	...	...	...	...
J1819-01A	18 19 02.93	–01 07 20.8	1.12	HIPASS J1819-01	3.7	...	...	...	...	...	...
J1819+01	18 19 20.68	+01 10 16.8	0.90	HIPASS J1819+01	2.5	...	...	2MFGC 14333[b]	0.9	...	...
J1822-35	18 22 38.90	–35 39 19.9	0.14	...	...	ESO 395-G002	2.9	...	...	...	...
J1823+00	18 23 23.65	+00 16 30.2	1.55	HIPASS J1823+00	1.9	...	...	J18232745+0016314	0.9	...	...
J1824-34	18 24 25.69	–34 12 09.8	0.37	...	...	ESO 395- G 004	1.3	...	...	...	...
J1824-01A	18 24 59.59	–01 27 41.0	1.48	HIPASS J1824-01	0.6	...	...	...	...	...	...
J1831-31	18 31 57.80	–31 45 24.2	0.15	...	...	ESO 457- G 015	2.3	...	...	...	..
J1841-18	18 41 18.08	–18 59 48.9	0.49	HIPASS J1841-18	3.1	...	...	...	...	...	...
J1846-23	18 46 42.93	–23 05 37.9	0.43	HIPASS J1847-23	5.4	CGMW 4-3021[d]	2.9	...	...	...	...
J1901-04	19 01 49.81	–04 29 21.5	0.72	HIZSS 109	0.7	...	...	...	...	...	...

* There is no enough information to decide whether this really is counterpart.
[a] In addition to HIPASS counterpart listed here a HIZSS galaxy, HIZSS 106 is also fond at a separation of 1.0′ and $\triangle V = 5$ km s^{-1}.
[b] Identification of the galaxy from The 2MASS-selected Flat Galaxy Catalog (2MFGC; Mitronova et al. (2004)).
[c] Identification of the galaxy in the catalogue of Woudt and Kraan-Korteweg (WKK; 1998).
[d] Identification of the galaxy in the Catalog of Galaxies Behind the MIlky Way (CGMW; Roman et al., 1998). [2] In the 2MASX incremental release (2MASXi).

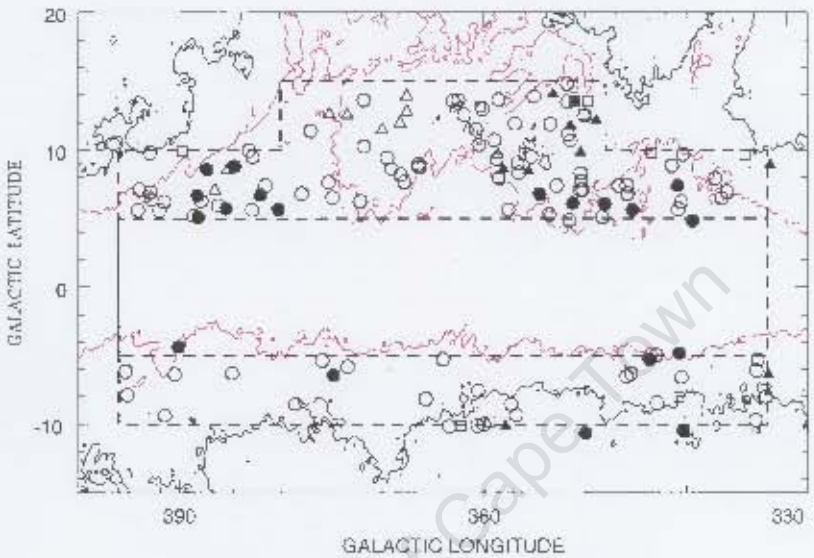

Figure 3.12: Spatial distribution of galaxies with multiwavelength counterparts. Galaxies with no counterparts are represented by open circles. Solid circles represent galaxies with HI counterparts, solid triangles represent galaxies with both optical and infrared counterparts, open triangles represent galaxies with infrared counterparts only and open squares represent galaxies with optical counterparts only. DIRBE extinction contours of $A_B = 1^m$ and 3^m are superimposed on the plot.

3.4.2 NIR Imaging of the Deep HI galaxy Sample

A systematic follow up for HI selected galaxies in the ZOA has begun using the Japanese Infrared Survey Facility (IRSF) at the Sutherland observing site of the South African Astronomical Observatory. The IRSF is a 1.4 m altazimuth Cassegrain telescope. The camera used has the Simultaneous-3color InfraRed Imager for Unbiased Surveys (SIRIUS). The images taken are in the J (1.26μm), H (1.63μm), and Ks (2.14μm) bands with a field of view of $7'.7 \times 7'.7$ (Nagayama et al., 2003). SIRIUS has an array of three 1024 × 1024 pixel HgCdTe detectors (HAWAII) arrays (Hodapp et al., 1996).

Motivation of the NIR Survey

Although the HI content of our galaxies has been studied, no information is available at other wavebands. A NIR imaging of these galaxies will allow us to determine their morphology and luminosity. Studying the characterstics of galaxies located around and in the Local Void particularly is important in order to verify if there is any relation between their properties

and the surrounding galaxy density.

In addition, for surveys close to the Galactic Plane the need of observations that can probe deeper than current existing surveys such as 2MASS is invaluable. The SIRIUS camera on the IRSF has the following advantages over the other NIR surveys:

- SIRIUS has a pixel scale of 0.45 arcseconds per pixel compared to the 2 arcsecond per pixel of the 2MASS, our data is more resolved by a factor of ~ 4.5.
- A typical ten minute exposure in SIRIUS probes to fainter limiting magnitudes than existing NIR surveys. This makes the IRSF an ideal instrument for surveys close to the Galactic Plane.

3.4.3 Observations

As part of the ongoing NIR ZOA survey, we performed a NIR observation for selected galaxies from the GB extension detections from 13 to 24 April 2007. Twenty-five dithered 24-second exposures were taken on the position of each galaxy, resulting in a total exposure time of 600 seconds in each of the three bands with a dithering step of 15 arcseconds between each exposure. The seeing varied between $\sim 0.''8$ and $1''.8$. In Table 3.6 the HI parameters of the observed galaxies with DIRBE extinction values (Schlegel et al., 1998) and the seeing during the observation is presented.
Details of the image processing procedure and data analysis can be found in James Tagg[3] thesis.

NIR Counterparts

Here we only looked at the rough color images to look for possible counterparts. Of the pointed observations towards the 31 HI detected galaxies, 6 galaxies have been detected, of which 5 are detected in the NIR for the first time. All of the detected galaxies are massive spairals except one very low mass galaxy. Figures 3.13, 3.14 and 3.15 show the J-H-K_s composite images of the detected galaxies with the HI parameters of the GB possible counterparts. The entries in Table 3.6 contain the following:
Column 1: Object name;
Columns 2 & 3: Equatorial coordinates (J2000) of the observed galaxies, Columns 4 & 5: Galactic coordinates;
Column 6: Extinction, $E(B-V)$, from DIRBE/IRAS 100 μ m extinction maps (Schlegel et al., 1998);
Column 7: Heliocentric velocity;
Column 8: Velocity width at 20% of the peak flux density;
Column 9: Integrated HI flux;
Column 9: Logarithm of the HI mass Column 10: Seeing;
Column 11: Flag noting (nd) for new NIR detection and (d) previously detected source.

[3]M.Sc student in the astronomy department, UCT.

Table 3.6: NIR observation specification of HI-galaxy candidates

Object name	R.A. (J2000) h m s	Dec. (J2000) deg ′ ″	l deg	b deg	$E(B-V)$	V_{hel} (km s^{-1})	W_{20} (km s^{-1})	S (Jykm s^{-1})	log M_{HI} ($M_\odot$)	Seeing (arcsecond)	Flag
J1604 -41	16 04 44.91	–41 43 35.4	337.19	7.94	0.77	4743	447	12.18	10.06	1.04	nd
J1610 -38	16 10 31.28	–38 20 26.0	340.34	9.67	0.73	4503	179	4.83	9.70	1.04	
J1620 -39	16 20 30.47	–39 36 24.3	340.84	7.41	0.83	2380	113	7.54	9.33	1.13	
J1623 -40	16 23 43.37	–40 39 03.4	340.53	6.24	1.17	4805	75	2.56	9.44	1.13	
J1624 -42	16 24 52.51	–42 26 43.7	339.39	4.83	1.06	2222	215	22.80	9.59	1.13	
J1629 -26	16 29 46.93	–26 45 13.1	351.75	14.79	0.48	5143	392	7.05	9.90	1.13	
J1642 -29	16 42 01.15	–29 10 38.8	351.68	11.16	0.30	2578	200	5.27	9.16	1.31	
J1643 -54	16 43 23.09	–54 02 34.7	332.93	-5.28	0.33	5206	211	7.30	9.68	1.71	
J1653 -35	16 53 59.76	–35 30 28.4	348.36	5.19	1.01	6364	270	17.60	10.30	1.71	
J1658 -30	16 58 41.78	–30 38 22.5	352.82	7.43	0.41	2796	203	4.48	9.20	1.35	
J1704 -33	17 04 39.17	–33 11 21.4	351.55	4.88	0.52	6204	193	7.00	10.03	1.71	
J1705 -27	17 05 32.20	–27 07 58.1	356.56	8.35	0.32	8247	121	2.79	9.92	1.13	
J1708 -31	17 08 37.12	–31 20 33.9	353.54	5.31	0.68	7141	246	6.69	10.18	0.99	
J1711 -47	17 11 40.04	–47 35 35.0	340.78	-4.79	1.76	2190	278	17.40	9.62	1.76	
J1719 -45	17 19 46.83	–45 52 28.4	343.00	-4.94	0.55	5804	287	5.62	9.89	1.76	
J1734 -16	17 34 23.66	–16 45 21.1	9.03	8.61	0.45	1417	88	2.29	8.23	0.81	
J1736 -47	17 36 46.93	–47 50 36.0	342.94	-8.45	0.24	5882	365	9.87	10.17	1.49	nd
J1749 -15	17 49 21.58	–15 20 45.8	12.12	6.26	0.66	7454	426	10.02	10.35	0.81	
J1757 -04	17 57 57.12	–04 03 33.2	23.10	9.96	1.18	1730	106	1.93	8.49	0.95	
J1807 -08	18 07 40.02	–08 36 33.2	20.23	5.67	1.35	3491	486	28.48	10.22	1.35	
J1814 -02	18 14 31.40	–02 27 10.6	26.50	7.07	2.04	1739	417	19.04	9.48	1.04	d
J1817 -03	18 17 50.94	–03 17 07.2	26.15	5.95	1.94	1873	107	3.38	8.80	0.86	
J1817 -32	18 17 31.74	–32 08 20.8	0.59	-7.56	0.25	953	263	3.51	8.17	1.26	
J1819 -01A	18 19 02.93	–01 07 20.8	28.22	6.68	1.12	2965	196	5.41	9.30	0.86	nd
J1824 -01B	18 24 31.71	–01 55 36.9	28.13	5.10	1.85	6204	226	6.47	10.02	1.22	nd
J1826+01	18 26 38.55	+01 33 33.9	31.49	6.23	1.47	2764	166	4.03	9.12	0.90	
J1826+03	18 26 37.54	+03 04 25.7	32.85	6.92	0.73	2956	130	3.70	9.20	0.90	
J1827+04	18 27 53.34	+04 07 14.0	33.93	7.11	0.39	2107	172	1.88	8.59	0.99	
J1828 -33	18 28 27.42	–33 10 44.7	0.69	-10.08	0.17	721	87	2.47	7.53	1.35	nd
J1836 -20	18 36 14.77	–20 00 19.7	13.39	-5.77	0.39	1668	73	2.53	8.56	1.08	
J1901 -04	19 01 49.81	–04 29 21.5	30.11	-4.35	0.80	1525	164	17.17	9.28	1.31	

Source name	l deg	b deg	$E(B-V)$	V_{hel} (km s^{-1})	W_{20} (km s^{-1})	S (Jy km s^{-1})	log M_{HI} ($M_\odot$)
J1604-41	337.19	7.94	0.77	4743	447	12.18	10.06

Source name	l deg	b deg	$E(B-V)$	V_{hel} (km s^{-1})	W_{20} (km s^{-1})	S (Jy km s^{-1})	log M_{HI} ($M_\odot$)
J1736-47	342.94	-8.45	0.24	5882	365	9.87	10.17

Figure 3.13: $J-H-K_s$ composite images of J1604-41(top) [2'.5 × 2'.5] and J1736-47 (bottom) [2'.5 × 2'.5].

Source name	l deg	b deg	$E(B-V)$	V_{hel} (km s^{-1})	W_{20} (km s^{-1})	S (Jy km s^{-1})	log M_{HI} ($M_\odot$)
J1814-02	26.50	7.07	2.04	1739	417	19.04	9.48

Source name	l deg	b deg	$E(B-V)$	V_{hel} (km s^{-1})	W_{20} (km s^{-1})	S (Jy km s^{-1})	log M_{HI} ($M_\odot$)
J1819-01A	28.22	6.68	1.12	2965	196	5.41	9.30

Figure 3.14: J-H-K_s composite image of J1814-02 (top; [1′.7×1′.7] and 1819-01 (bottom) [2′.7×2′.7].

Source name	l deg	b deg	$E(B-V)$	V_{hel} (km s^{-1})	W_{20} (km s^{-1})	S (Jy km s^{-1})	log M_{HI} ($M_\odot$)
J1824-01B	28.13	5.16	1.85	6204	226	6.47	10.02

Source name	l deg	b deg	$E(B-V)$	V_{hel} (km s^{-1})	W_{20} (km s^{-1})	S (Jy km s^{-1})	log M_{HI} ($M_\odot$)
J1828-33	0.69	-10.08	0.17	721	87	2.47	7.53

Figure 3.15: J-H-K_s composite image of J1824-01B (top) [1′.3 × 1′.3] and J1823-33 (bottom) [0′.5 × 0′.5].

Chapter 4

Implications for the Nearby Large-Scale Structure

Although the number of galaxies discovered in this survey is not very high, some large-scale structures became apparent in our data. The two dynamically important large-scale structures, the Local Void and the Ophiuchus supercluster could be outlined in further detail. While the Local Void exposed itself as under-dense region, Ophiuchus at larger distance stood out as an overdensity with possible connection to the GA and Norma cluster. Moreover, the presence of a "second arm" to the Norma supercluster parallel to the GA-Wall has been revealed in this data.

The resulting large-scale structure plots and detailed discussions on the distribution of our detections are presented in the following sections. Previously catalogued galaxies from different surveys have sometimes been included for comparison as well as for tracing large-scale structure adjacent to our survey area.

4.1 The Distribution of the GB Extension Galaxies

4.1.1 Distribution along Galactic latitude

The distribution of the GB extension galaxies as a function of Galactic latitudes is shown in Fig. 4.1. Of the 158 detections, 39 lie in the region $-10° \leq b \leq -5°$, 83 in the region $5° \leq b \leq 10°$ and 36 in the $10° < b \leq 15°$, with a number density, $n \approx 0.12$, 0.26 and 0.23 deg^{-2} respectively. This implies higher densities of galaxies in the regions $5° \leq b \leq 10°$ and $10° < b \leq 15°$ compared to the strips below the Galactic Plane (see also Fig. 4.11). The overdensity at positive latitudes is partly due to the large-scale structures, such as the new "second arm" of the Norma supercluster and the Ophiuchus cluster (see also Figs. 4.18 and 4.19).

In Fig. 4.2 the distribution along Galactic latitude is combined and compared with the HI Parkes Deep ZOA Survey (here after HIZOA) preliminary catalog[4], and the HIPASS galaxies(Meyer et al., 2004; Wong et al., 2006) in the same GB extension region. The GB

[4]Kraan-Korteweg 2008, private communication

extension galaxies are represented by solid histograms while HIZOA and HIPASS galaxies are represented by dotted and filled histograms respectively. The detection rate of the HIZOA and GB extension is almost equal except that the GB extension to higher latitudes, $10° < b \leq +15°$, is done only for the region $352° \leq l \leq 24°$, i.e. 4 central cubes out of 8 for the positive latitudes. A fairly flat distribution is found throughout for HIPASS detection rate. The GB extension detections clearly outnumber the HIPASS galaxies (as expected since it has 5 times longer integrations). In these HI surveys, galaxies seem to be detected in the Galactic Bulge region with hardly dependence on latitude apart from the small dip in the distribution of the HIZOA detections between $l \sim -2°$ and $+1°$ which is due to high number of continuum sources in the Galactic Bulge region (Kraan-Korteweg, 2005).

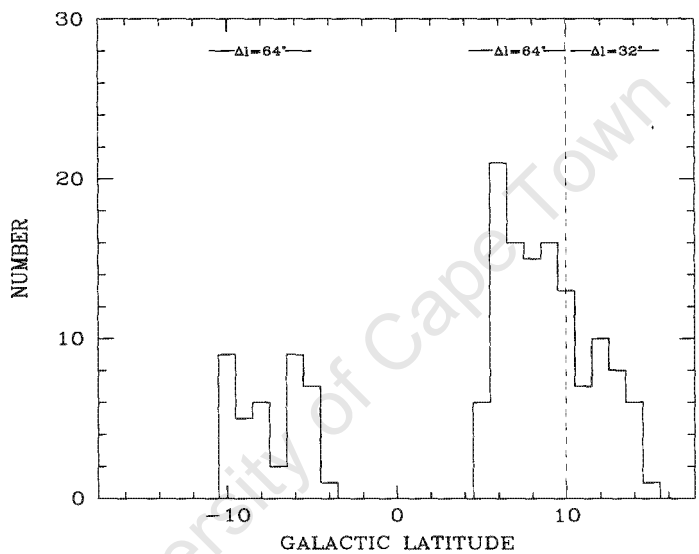

Figure 4.1: Distribution of galaxies and candidates detected in the GB extension survey as a function of Galactic latitude. The vertical dashed line shows the GB extension towards higher latitudes performed only for the region $352° \leq l \leq 24°$.

4.1.2 Distribution along Galactic longitude

Figure 4.3 shows the distribution of the GB extension galaxies as a function of Galactic longitude. The solid histogram shows the number density for the latitude strips $5° \leq |b| \leq 10°$ over the longitude range $332° < l < 36°$ $(-38° < l < 36°)$. The detection rate at higher latitude, $10° < b \leq 15°$ over the longitude $352° \leq l \leq 24°$ $(-8° \leq l \leq 24°)$ is shown by the dashed histogram. A higher number density is found in the region $-30° < l < 0°$ (see Fig. 4.11).

The distribution is compared with the HIZOA (dotted histogram) and HIPASS (filled histogram) detections in Fig. 4.4, The detections are subdivided in sequence of increasing latitudes from $b = -10°$ to $15°$ in steps of $\Delta b = 5°$ (Note that $|b| \leq 5°$ is out of the GB extension coverage). The effect of the large-scale structures is clearly evident in these histograms. The underdensity in the lower latitudes is even more conspicuous in the bottom

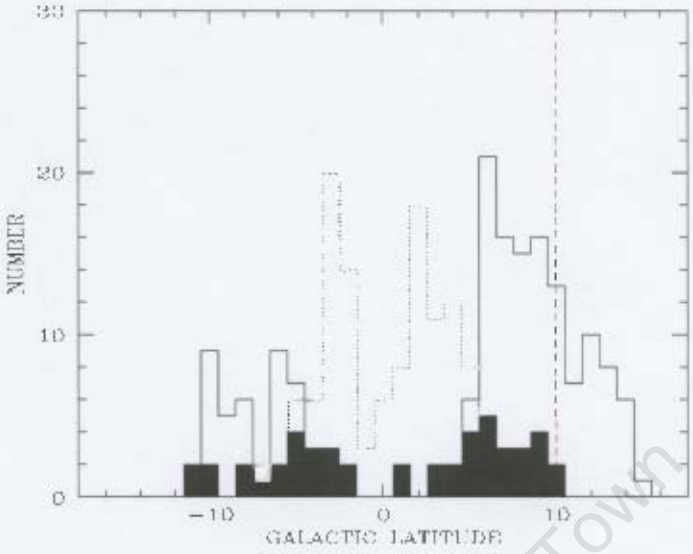

Figure 4.2: Distribution of the GB extension galaxies (solid histogram) as well as galaxies in HIZOA (dotted histogram) and HIPASS in our survey area (filled histogram) as function of Galactic latitude. The GB extension towards higher latitudes is again shown by vertical dashed line.

panel of Fig. 4.4. In the region $|b| \leq 5^\circ$ the number of galaxies increased dramatically with HIZOA. A higher number density around in the region $l \sim -25^\circ$ to $-15^\circ(335^\circ - 345^\circ)$ is seen with a prominent peak around $-20^\circ(340^\circ)$ due to the GA overdensity adjacent to the survey region. The distribution of the GB extension galaxies in the region $5^\circ < b < 10^\circ$ (second upper histogram) shows a large dip in the region between $l \sim 0^\circ$ and 20°, dividing the fairly uniform distribution into $l < 0^\circ$ and $l > 20^\circ$. The relative higher fraction of detections on the left side of this histogram of the HIPASS galaxies indicates that galaxies found in $l \sim 25^\circ$ to 35° are nearby galaxies as HIPASS is shallower, hence more sensitive to nearby galaxies (see Figs. 4.5 and 4.12). In the upper panel of this same Fig. 4.4 the GB extension galaxies stand out. No HIPASS galaxy is found in the region $l < 0^\circ$ in this latitude range of our survey region. This implies that the distinct peak around 0° is due to a concentration of galaxies at larger distance. In general, we see a strong variation in the number of GB extension galaxies in these histograms which can be explained by large-scale structure. The overdensity in the region $-30^\circ < l < 0^\circ$ ($330^\circ < l < 360^\circ$, see also Fig. 4.11) region seem to be related with the excess mass found in the GA region and the Ophiuchus superchuster (see Section 4.3.3). On the other hand, due to the Local Void located around the region $l \sim 0^\circ - 40^\circ$, the detection rate in this region is lower (see Section 4.3.1 for further discussion). The variation is also visible in HIZOA.

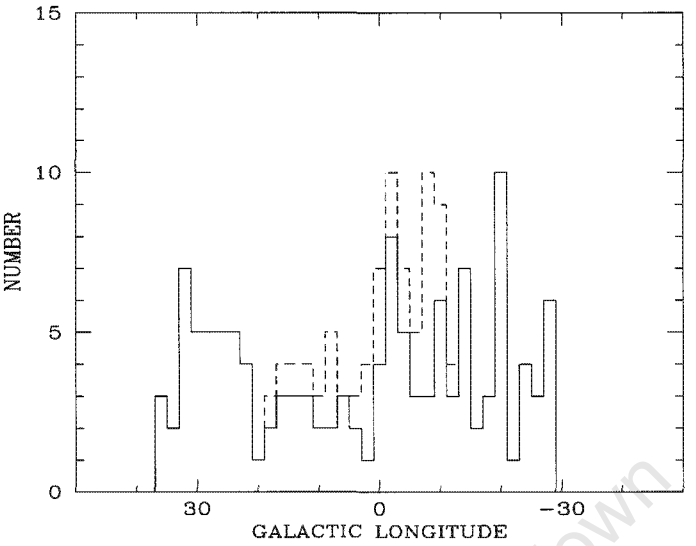

Figure 4.3: Distribution of galaxies detected in the GB extension survey as a function of Galactic longitude. The number of galaxies found in $5° \leq |b| \leq 10°$ and $332° < l < 60°$ $(-28° < l < 36°)$ is shown by the solid histogram and the dashed histogram includes the number of galaxies in the region $10° < b \leq 15°$ over the longitude $352° \leq l \leq 24°$ $(-8° \leq l \leq 24°)$.

4.1.3 HI Velocity Distribution

The heliocentric velocity distribution of the GB extension galaxies is shown in Fig. 4.5 (solid histogram). The lower filled histogram shows the velocity distribution of the HIPASS galaxies in our survey region. The detection rate is as expected lower in the shallower HIPASS. Although the main concentration of the GB extension galaxies (74 %) is in the velocity range of 2000 to 9000 km s^{-1}, detections are found out to 12,000 km s^{-1}. This upper limit corresponds to the cut off limit of the deep HI Parkes ZOA surveys. The velocity distribution of both the HIZOA and NE survey are shown for comparison (see Fig. 4.6 and Fig. 4.1.3). Again, the effect of the nearby large-scale structures is clearly visible in the histogram with a strong dip for $V < 2000$ km s^{-1} and prominent peaks near 4000, 6000 and 8500 km s^{-1}. While the nearby dip is due the Local Void, the GA overdensity ($\sim$ 4000 km s^{-1}) and the Ophiuchus supercluster ($\sim$ 8500 km s^{-1}) are responsible for the higher number density in the corresponding regions. The peak around 6000 km s^{-1} seems to be due to the presence of a filament crossing the Norma cluster pointing to the Ophiuchus cluster. This is discussed in further detail on Section 4.3. In Fig. 4.6 the HIZOA ($212° \leq l < 332°$) is used to compare the velocity distribution. The GB extension histogram shows a much lower density of nearby galaxies compared to HIZOA due to the influence of the Local Void. Otherwise the velocity distribution out to $V < 8000$ km s^{-1} is quite similar. Above this velocity the above mentioned peak at $\sim$ 8500 km s^{-1} in the GB extension distribution is new and highly significant.

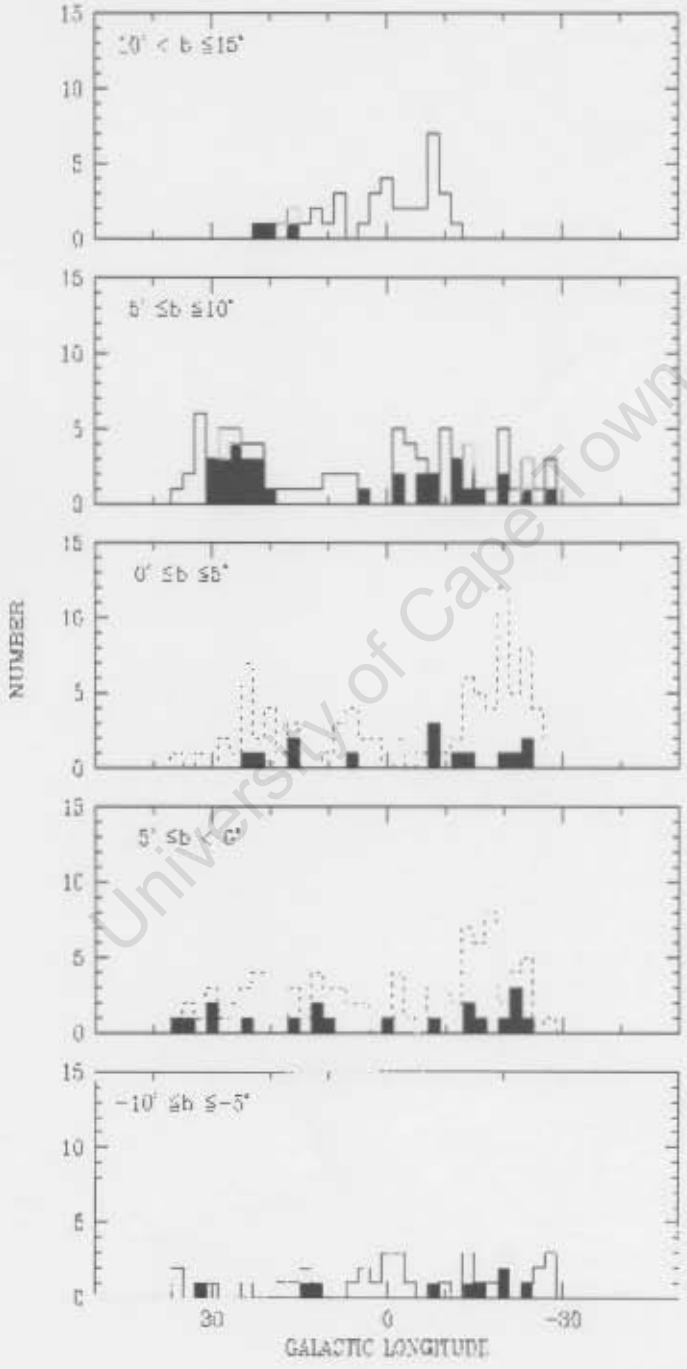

Figure 4.4: The distribution of the CB extension galaxies (solid histogram), HIZOA (dotted histogram) and HIPASS in our survey region (filled histogram) along the Galactic longitude in sequence of increasing latitudes marked at the left corner of each histogram.

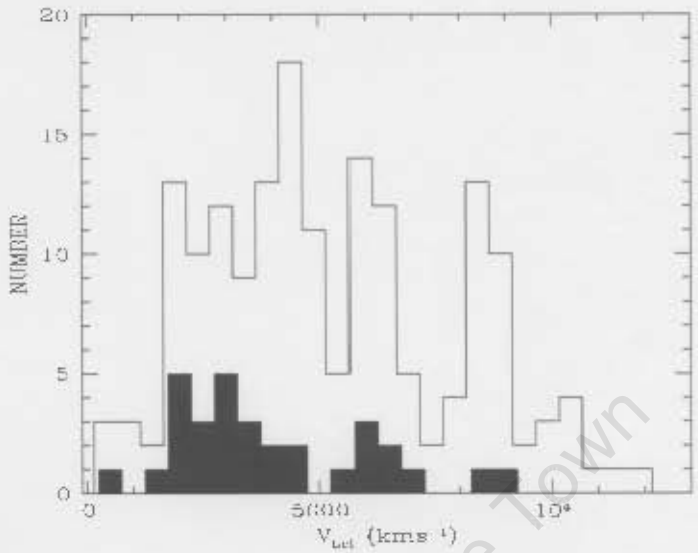

Figure 4.5: Velocity distribution of galaxies detected in the CB extension survey (solid histogram). The lower filled histogram shows the velocity distribution of HIPASS.

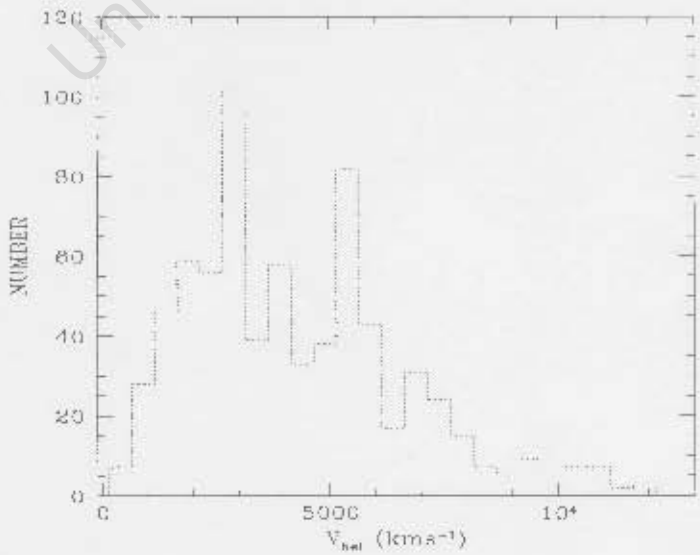

Figure 4.6: Velocity distribution of galaxies in the preliminary HIZOA catalog[4].

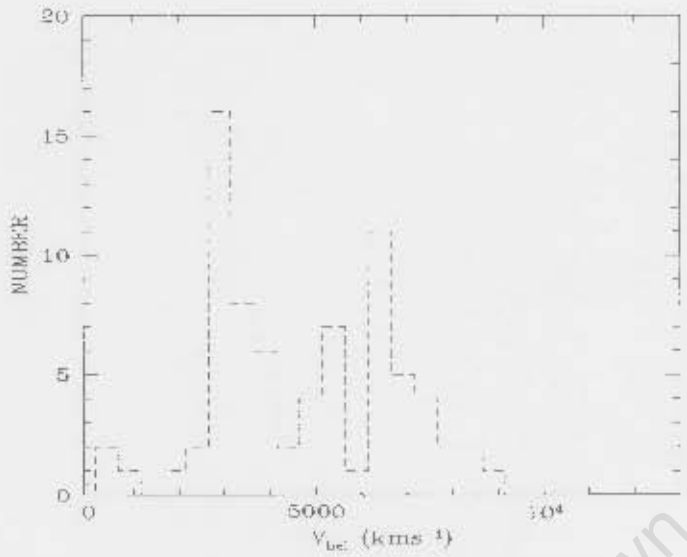

Figure 4.7: Velocity distribution of galaxies in NE.

4.1.4 HI Mass Distribution

Figure 4.8 shows the HI mass distribution of the GB extension detections. The galaxies range from 2.3×10^7 $M_\odot$ to 3.8×10^{10} $M_\odot$ in HI mass, with the majority between 1×10^9 $M_\odot$ and 3×10^{10} $M_\odot$. The mean HI mass is 8.8×10^9 $M_\odot$. For comparison, the HI mass distribution of galaxies detected in HIZOA and NE, are shown in Fig. 4.9and Fig. 4.10 respectively. The preliminary HIZOA has a mean HI mass of 3.0×10^9 $M_\odot$. The mean HI mass of the NE was 4.3×10^9 $M_\odot$ (Donley et al., 2005). The higher mean HI mass of the GB extension is most likely due to the detection of so many galaxies at large distances in combination with the lack of nearby galaxies due to the prominence of the Local Void in this area. For instance, a 5σ detection with $\Delta W_{20} = 200$ km s^{-1} at 8500 km s^{-1} has about 1.8×10^{10} HI mass. This implies the presence of massive galaxies around the Ophiuchus supercluster.

The Lowest Mass Galaxies

Only five sources in the GB extension have HI masses below 10^8 $M_\odot$. Of these only one was previously known in HIPASS. The galaxies with the lowest HI masses are J1549-46 (or HIPASS J1548-46, Meyer et al., 2004), J1727-18A, J1814-35, J1828-33 and J1834-30 (see Section 4.2 for their HI parameters).

The Highest Mass Galaxy

The highest mass galaxy detected in the GB extension is J1621-36, having $\sim 3.9 \times 10^{10}$ $M_\odot$ of HI mass with a velocity of 4447 km s^{-1}. It is an HI counterpart of the optical galaxy, ESO 390-G004 (Lauberts, 1982).

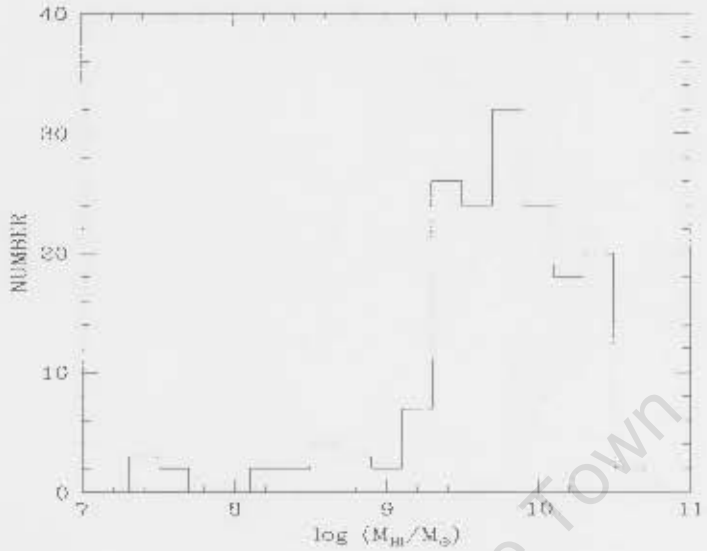

Figure 4.8: HI mass distribution of galaxies detected in the GB extension survey. The mean HI mass is 8.8×10^9 $M_\odot$.

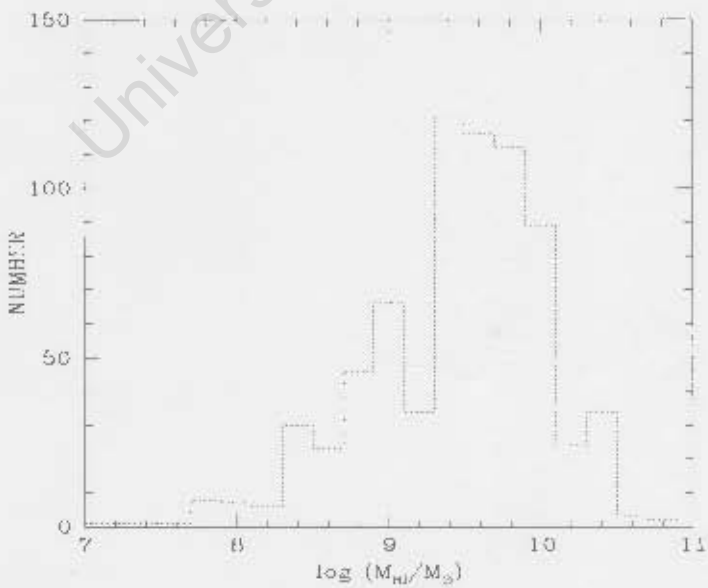

Figure 4.9: HI mass distribution of galaxies in HIZOA with preliminary mean HI mass of 3.0×10^9 $M_\odot$.

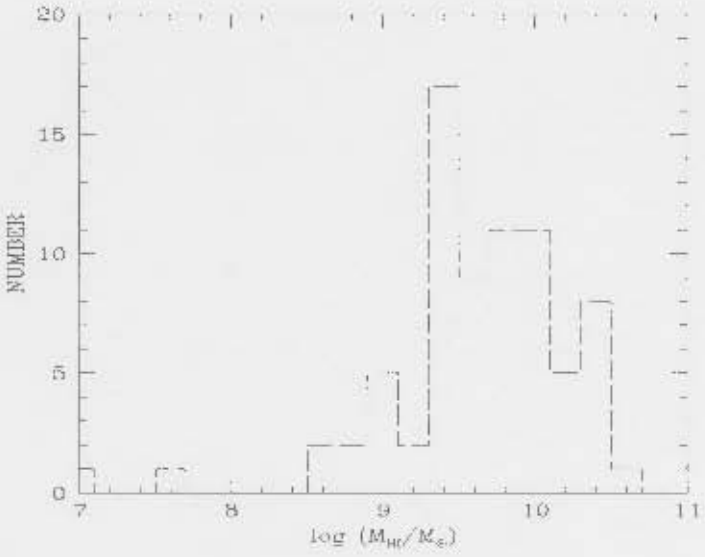

Figure 4.10: HI mass distribution of galaxies in NE with the mean HI mass of 4.3×10^9 $M_{\odot}$ (Donley et al., 2005).

4.1.5 Distribution in Space

The spatial distribution of the HI detected galaxies in the GB extension survey is shown in Fig. 4.11. The survey region is defined by the dashed lines. Overall a higher density of detections is found above the Galactic Plane ($n \approx 0.24$ deg^{-2}) compared to the detections below the Galactic Plane ($n \approx 0.12$ deg^{-2}). Even higher concentration of galaxies is found around $l \sim 345^{\circ}(-15^{\circ})$ to 0° and $b \geq 5^{\circ}$ followed by a region devoid of galaxies around $l \sim 0^{\circ}$ to 10°. The region $b \leq -5^{\circ}$ is generally underdense (see also Fig. 4.1).

Figure 4.12 shows the distribution of galaxies in the GB extension survey in Galactic coordinates superimposed on previously catalogued galaxies from HIPASS (Meyer et al., 2004; Wong et al., 2006). The GB survey region is again defined by dashed lines. From this plot we can see that the majority of HIPASS galaxies are as expected found at lower velocities, $cz \leq 3000$ km s^{-1} with some indication of structures out to 7000 km s^{-1}. Furthermore, an extermely low number of HIPASS galaxies has been detected in the most opaque part of the ZOA, $-5^{\circ} \leq b \leq +5^{\circ}$. However, when we look at the distribution of galaxies in Fig. 4.13, where next to the GB extension detections, the galaxies from HIPASS and the deep HIZOA and NE surveys have been displayed, that part of the ZOA has been filled by the deep HI surveys. The lower detection rate of HIPASS is also continued in our survey region, where only 29 HIPASS galaxies are found compared to the 129 GB extension detections.

In order to have a complete image of the spatial distribution of galaxies around our survey region, galaxies in the LEDA[5] with known velocities in the velocity range of our survey, i.e., $1200 < cz < 12700$ km s^{-1}, have been included in Fig. 4.14. Several large-scale structures can be seen around $l \sim 336^{\circ} - 360^{\circ}$ (-24° to 0°) followed by an underdense region around $l \sim 350^{\circ}$ 40° (-10° to 40°). Details of the observed features in this figure are discussed in Section 4.3.

[5]it is not a uniform sample over the regarded area

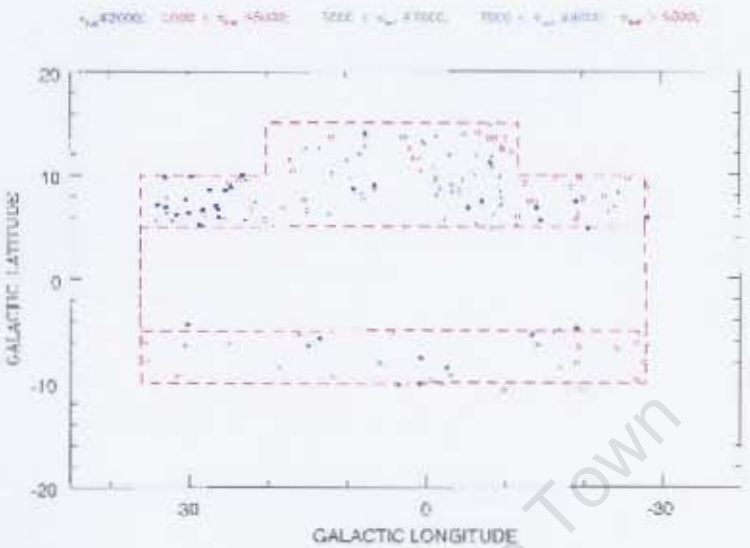

Figure 4.11: Distribution of galaxies detected in GB extension in Galactic coordinates colour coded according to their velocities. Blue filled circles: $v_{hel} \leq 3000$; magenta open circles: $3000 < v_{hel} \leq 5000$; green filled triangles: $5000 < v_{hel} \leq 7000$; cyan open triangles: $7000 < v_{hel} < 9000$; red crosses: $v_{hel} > 9000$ km s^{-1}.

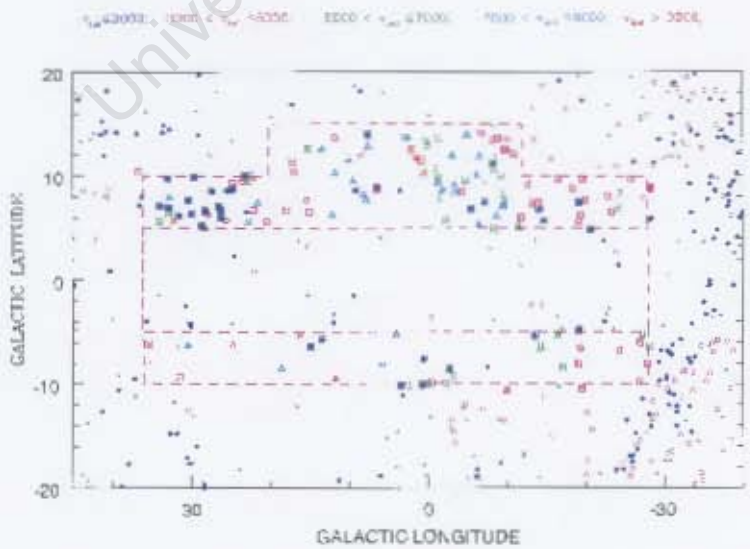

Figure 4.12: Distribution of GB detections (marked by square) and galaxies from HIPASS in Galactic coordinates. Blue filled circles: $v_{hel} \leq 3000$; magenta open circles: $3000 < v_{hel} \leq 5000$; green filled triangles: $5000 < v_{hel} \leq 7000$; cyan open triangles: $7000 < v_{hel} \leq 9000$; red crosses: $v_{hel} > 9000$ km s^{-1}.

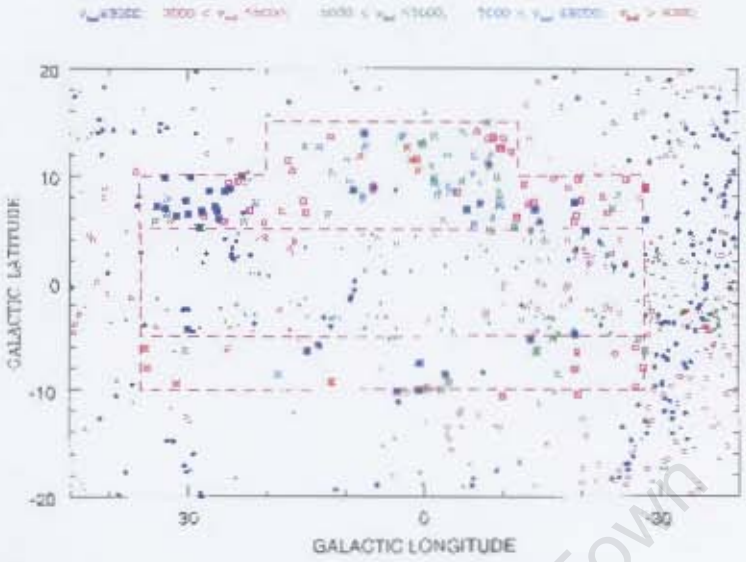

Figure 4.13: Distribution of GB detections (marked by square), galaxies from HIPASS, HIZOA and NE in Galactic coordinates. Blue filled circles: $v_{hel} < 3000$; magenta open circles: $3000 < v_{hel} \leq 5000$; green filled triangles: $5000 < v_{hel} \leq 7000$; cyan open triangles: $7000 < v_{hel} \leq 9000$; red crosses: $v_{hel} > 9000$ km s^{-1}.

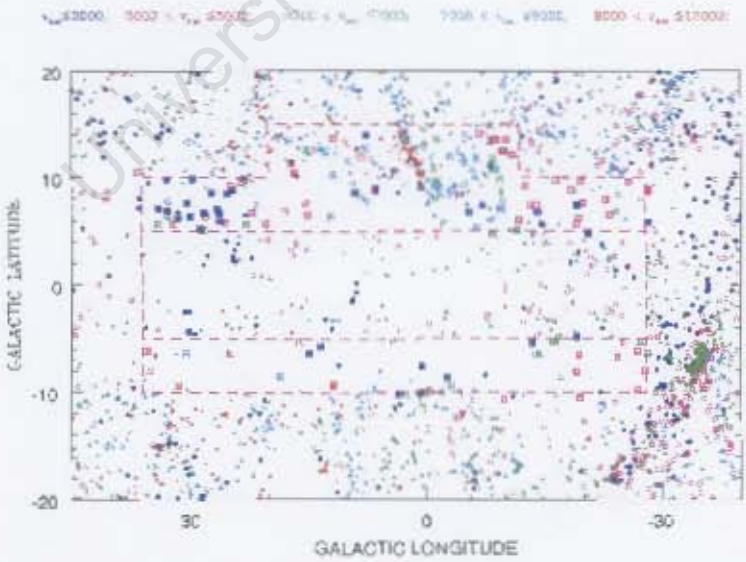

Figure 4.14: Distribution of GB detections (marked by square) in Galactic coordinates superimposed on galaxies from HIPASS, HIZOA and NE as well as galaxies from LEDA with known velocities. Blue filled circles: $v_{hel} \leq 3000$; magenta open circles: $3000 < v_{hel} \leq 5000$; green filled triangles: $5000 < v_{hel} \leq 7000$; cyan open triangles: $7000 < v_{hel} \leq 9000$; red crosses: $9000 < v_{hel} \leq 12000$ km s^{-1}.

4.2 Nearby Galaxies

The five galaxies (J1549-46, J1727-18A, J1814-35, J1828-33 and J1834-30) with the lowest HI masses have very low heliocentric velocities ($cz < 900$ km s^{-1}). Of these, four are detected for the first time. The newly detected galaxy J1727-18A ($l, b = 6°.38, 8°.95$) has a heliocentric velocity of 346 km s^{-1}, with a velocity width, $W_{20} = 62$ km s^{-1}, at a distance of 4.3 Mpc. This galaxy is the nearest galaxy detected in this search. If it were not for its compactness, which suggest it is a more likely nearby galaxy rather than a HVC, it could be considered as HVC. But confirmation is still needed, since it is found in the part of the survey which has not been searched by an independent group and no optical or NIR counterpart is found.

The second newly detected nearby galaxy is J1834-30 ($l, b = 3°.45, -10°.15$), with a heliocentric velocity of 440 km s^{-1} and W_{20}= 74 km s^{-1} at a distance of 6.8 Mpc. The other two newly detected nearby galaxies are J1828-33 ($l, b = 0°.69, -10°.08$) with $v_{hel} = 721$ kms^{-1} and $W_{20} = 87$ km s^{-1}, and J1814-35 ($l, b = 357°.32, -8°.56$), with $v_{hel} = 591$ km s^{-1} and $W_{20} = 71$ km s^{-1} at a distance of 7.6 Mpc and 9.8 Mpc respectively. A NIR counterpart has been found for the former one during our NIR follow-up observation which was made using the IRSF (see Section 3.4.3 for the image taken in J, H and K_s bands).

The previously known nearby galaxy was detected in HIPASS (HIPASS J1548-46; $l, b = 331°.72, 5°.85$). With a heliocentric velocity of 775 km s^{-1} and a distance of 6.8 Mpc, it is also the lowest mass galaxy detected in this survey ($M_{HI} = 2.32 \times 10^7$ M$_\odot$) . It is interesting to note that all of these very nearby galaxies lie in or close to the Local Void. Their narrow velocity width together with their environment suggests they could be nearby dwarf galaxies.

Table 4.1: The 5 nearest galaxies.

Source name	l deg	b deg	$E(B-V)$ mag	V$_{hel}$ km s^{-1}	W_{20} km s^{-1}	D Mpc	log M_{HI} ($M_\odot$)	Possible counterpart
J1549-46	331.72	5.85	0.62	775	62	6.8	7.37	HIPASS J1548-46
J1727-18A	6.38	8.95	0.76	346	156	4.3	7.41	...
J1814 -35	357.32	–8.56	0.22	591	71	9.8	7.66	...
J1828 -33	0.69	–10.08	0.19	721	87	7.6	7.53	...
J1834 -30	3.45	–10.15	0.18	440	74	6.8	7.61	...

4.3 Large-Scale Structures in the GB Extension Survey

The detections in this survey uncover various large-scale structures that lie behind the Galactic Bulge. In the following sections, the most prominent features will be discussed in sequence of increasing velocity.

4.3.1 The Local Void

As mentioned in Chapter 1 (Section 1.4) the Local Void located close to the Galactic Bulge is the dominant void in the nearby universe. Although several attempts have been made to

unambigously determine the size and distance of the Local Void, assessing its actual size and extent has been difficult mainly because the large fraction of the Local Void is located behind the Milky Way.

Tully & Fisher (1987) claimed that the Local Void extends from $l = 0°$ to $90°$ and from $b = -30°$ to $+30°$ within $cz < 3000$ km s^{-1} from their study on the sky distribution of galaxies within $cz = 3000$ km s^{-1}. Saunders et al. (1991) found the Local Void in the density field of the distribution of IRAS galaxies around $l = 40°, b = -17°$, and $cz = 2300$ km s^{-1}. Nakanishi et al. (1997) located the centre of the Local Void to be at $l = 60°, b = -15°$, and $cz \sim 2500$ km s^{-1}. Despite the difficulties in assessing the true dimensions of the Local Void, Fairall (1998) suggested a smaller size locating its centre at $l = 18°, b = 6°$ and $cz = 1500$ km s^{-1}. However, Koribalski et al. (2004) redefine the dimensions of the Local Void based on HIPASS data as approximately $l \sim -10°$ to $+20°, b \sim -20°$ to $+20°$ and $cz \lesssim 1700$ km s^{-1} showing a more extended appearance of the void up to $l = 30° - 40°$ for $b \sim -20°$ to $0°$. They also pointed out the smaller appearance of the void in HI sky compared to optical.

More recently Tully (2007) claims that the Local Void must be extremely empty and larger than previously thought to explain the large peculiar motion of the Milky Way away from the Local Void. This idea is supported by the large peculiar velocity they found for the lonely dwarf galaxy ESO 461-36 that sits inside the Local Void. The galaxy is being pushed out of the void with ~ 230 km s^{-1}. This suggests, according to the authors, a bigger and emptier void.

The distribution of galaxies detected in the GB extension (marked by squares), HIZOA and NE, HIPASS as well as galaxies from LEDA with known velocities in our velocity range is shown in Fig. 4.15 in three consecutive redshift slices of $\Delta v = 2000$ km s^{-1} from 0-6000 km s^{-1}. Figure 4.16 shows a redshift cone for the same redshift range, i.e., out to 6000 km s^{-1}, of galaxies in the deep HI surveys, GB extension, HIZOA and NE. In the subsequent Fig. 4.17 the same redshift cone, now also includes HIPASS and LEDA galaxies (with known velocities in our velocity coverage)in the region $-10° \leq b \leq 15°$.

In Fig. 4.15 we note a lower density of galaxies in the region $l \sim 330°$ to $45°$. However, it is not completely empty of galaxies. This is also seen in the redshift cone shown in Fig. 4.16. The overall underdensity of galaxies seems to extend up to $cz \sim 6000$ km s^{-1} supporting the larger void idea. However, a filamentary feature is visible around 3000 km s^{-1} (see middle panel of Fig. 4.15, also see Fig. 4.16) which seems to divide the void into two components: a nearer and distant void above and below the Galactic Plane. Nevertheless, neither of these two voids seem to be totally empty nor well defined. Six nearby and low mass galaxies and candidates have been detected within the nearest part ($cz \lesssim 1500$ km s^{-1}) of the Local Void in the GB extension survey. As shown in both Figs. 4.15 and 4.17 a structure juts out into the nearer Local Void around 1500 km s^{-1} and $(l, b) \sim 30°$ and $6°$. From the galaxy distribution shown in Figs. 4.15, 4.16 and 4.17 it can be said that the Local Void consists of a large under-dense region out to $cz \lesssim 6000$ km s^{-1} extending from $l \sim 345°$ to $45°$ and $b \sim -30°$ to $+45°$. Various sparsely populated filaments seem to be subdivide the Local Void into smaller spheres. Even the latter are not completely empty. Six very low mass galaxies (described in 4.2) are found in these regions. A systematic NIR followup of these galaxies

together with other HI detected galaxies is currently being pursued.

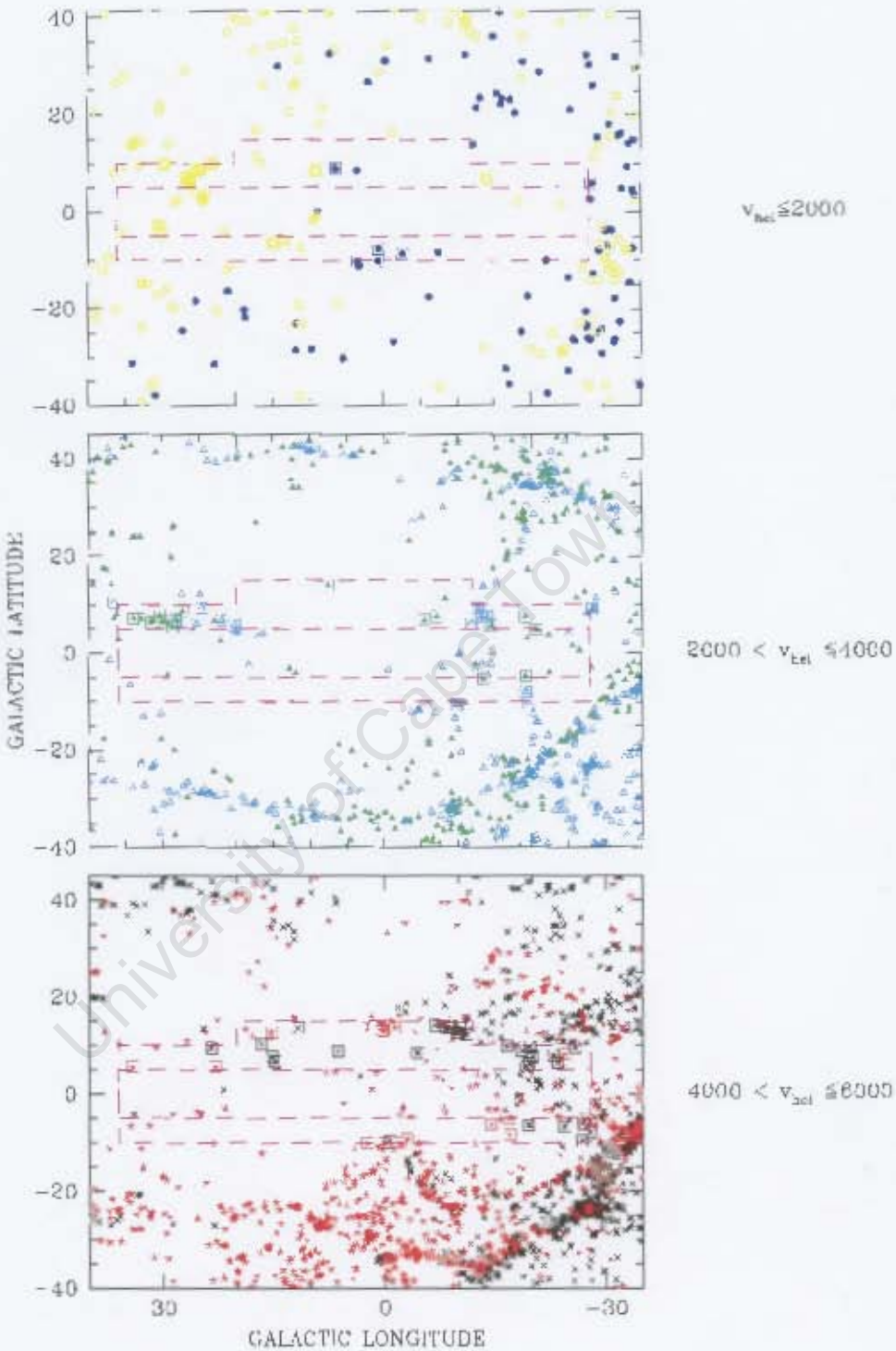

Figure 4.15: The three panels show the distribution in Galactic coordinates of the galaxies and candidates with $cz \leq 6000$ km s^{-1}, in intervals of 2000 km s^{-1}, detected in HIZOA and northern extension surveys, GB extension survey, HIPASS and includes galaxies from LEDA with known velocities. Within the panels the redshifts are subdivided and colour coded into intervals of $\Delta v = 1000$ km s^{-1}. Blue filled circles: $v_{hel} < 1000$; yellow open circles: $1000 < v_{hel} < 2000$; green filled triangles: $2000 < v_{hel} \leq 3000$; cyan open triangles: $3000 < v_{hel} \leq 4000$; black crosses: $4000 < v_{hel} \leq 5000$; red stars: $5000 < v_{hel} \leq 6000$.

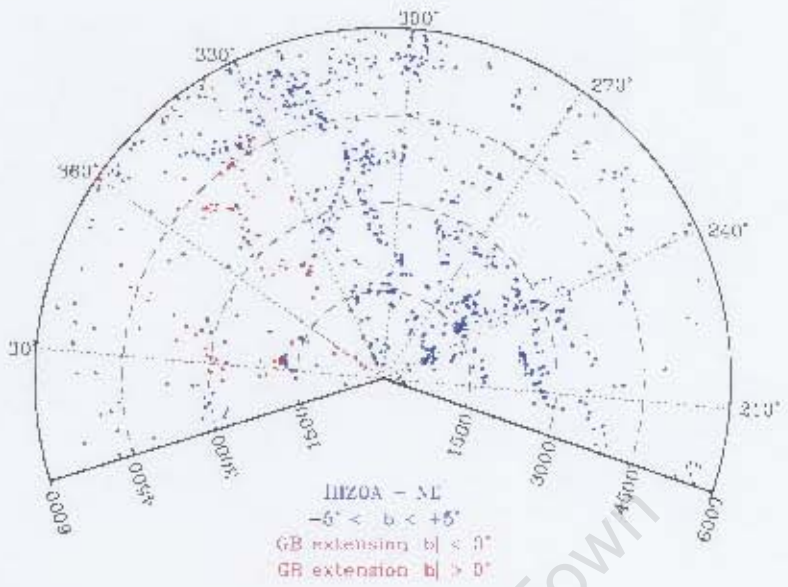

Figure 4.16: A redshift cone, out to 6000 km s^{-1}, of galaxies detected in the deep HI surveys, HIZOA and NE ($|b| \leq 5°$; blue) and the GB extension ($b| < 0°$; magenta, $b| > 0°$; red).

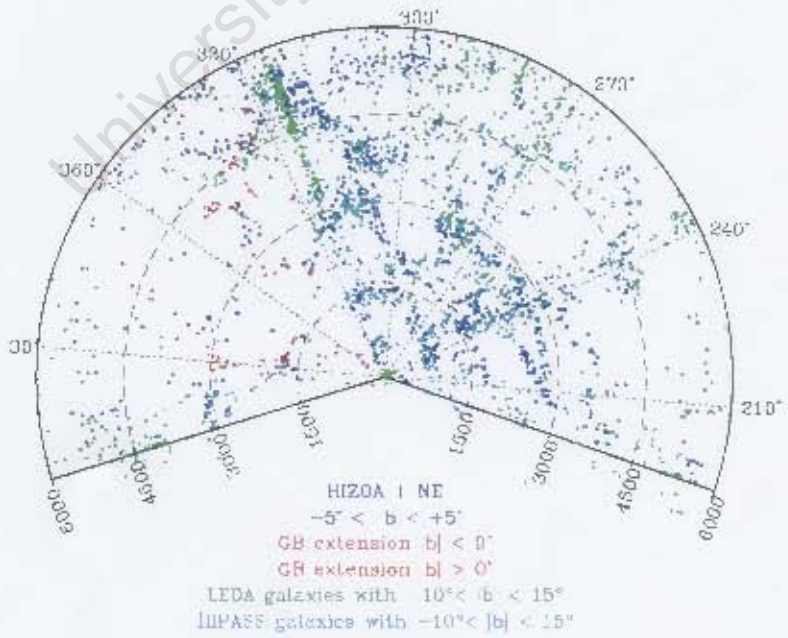

Figure 4.17: A redshift cone, out to 6000 km s^{-1}, of galaxies in HIZOA and NE ($|b \leq 5°$; blue), the GB extension ($b| < 0°$; magenta, $|b| > 0°$; red), **HIPASS** (for $-10° \leq b \leq 15°$; cyan and galaxies from LEDA (for $-10° < |b| < 15°$; green).

4.3.2 Structures around the GA

Figure 4.18 shows the distribution of GB extension galaxies(squares) and previously cataloged galaxies (HIZOA with NE, HIPASS and LEDA, with known velocities) in Galactic coordinates from 3000 to 7000 km s^{-1} in two interval of widths 2000 km s^{-1}. We see a very populated region on the right hand side of Fig. 4.18 due to the GA over-density. The massive cluster in the GA region, the Norma cluster A3627 lies at $(l, b, v = 325°, -7°, 4848$ km s^{-1}; Kraan-Korteweg et al., 1996). Part of the Centaurus-Wall, a wall of galaxies which cross a large part of the southern sky (Fairall, 1998), is also prominent as a filament of galaxies stretching down from the Norma cluster.

The most interesting new feature observed in Fig. 4.18 is the by Kraan-Korteweg (2005) suspected wall-like structure, parallel to the GA-Wall, running from the Centaurus cluster Abell 3526 $(l, b, = 322, +22)$ down to the GP towards higher longitudes crossing the GP at $l \sim 345°$. This feature could be a "second parallel arm" to the Norma supercluster. Erdogdu et al. (2006) applied a statistical reconstruction method, the Wiener Filter, which is developed for reconstruction of corrupt or incomplete data (Fisher et al., 1995) on Two MASS Redshift Survey (2MRS). Amazingly enough, they were able to identify a new overdensity around $(l, b) \sim 345°, 10°$ at 4000 km s^{-1} on their reconstructed density field maps. This density peak is found exactly where the above mentioned second wall-like structure parallel to the GA-Wall is seen in our survey. Hence the presence of this new structure is confirmed for the first time with the GB extension survey.

In addition to these prominent large-scale structures, there seems to exist continuous filamentary structure that intersects the GA-Wall at the location of the Norma supercluster and stretches into the distant Microscopium void (Fairall, 1998) at $(l, v) \sim 350°, 4500$ km s^{-1} and $340°, 5000$ km s^{-1} towards the Ophiuchus supercluster (it is noticable on Fig. 4.17 as well). This connection is only weakly seen and needs further observations to confirm this possible connection between the Norma supercluster and the Ophiuchus cluster.
If both these feature are real, i.e., the second parallel wall and the possible connection of the Norma supercluster and the Ophiuchus cluster, the mass contributing to the GA overdensity could be much larger than previously assumed based on the Norma supercluster, with .

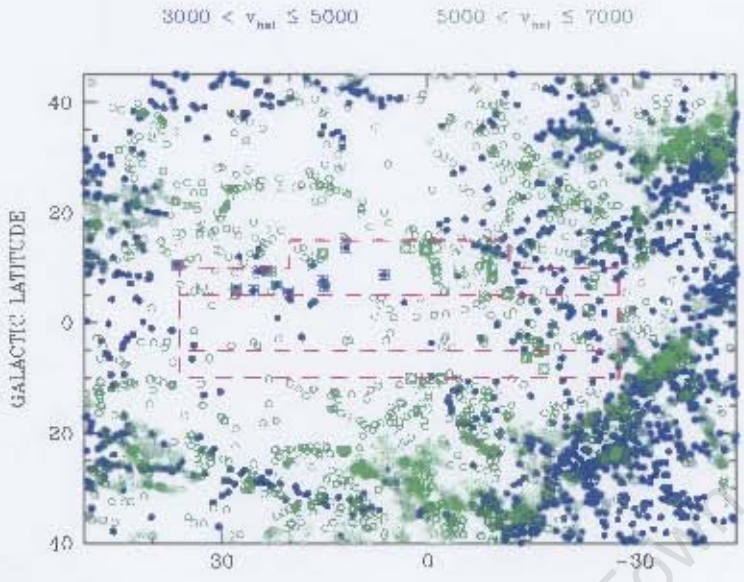

Figure 4.18: The distribution in Galactic coordinates of the galaxies $3000 \leq cz \leq 7000$ km s^{-1}, in intervals of 2000 km s^{-1}, detected in HIZOA, NE, GB extension (squares), HIPASS and galaxies from LEDA with known velocities in velocity coverage. Blue filled circles: $3000 < v_{hel} \leq 5000$; green open circles: $5000 < v_{hel} \leq 7000$.

4.3.3 Structures around the Ophiuchus Supercluster

As we go to higher velocity slices we find a prominent concentration of galaxies at velocities between 8000 and 9000 km s^{-1} (see also the velocity histogram in Fig. 4.5). These are related to the Ophiuchus supercluster at $l = 0.56°, b = +9.27°, cz = 8500$ km s^{-1} (Wakamatsu et al., 2000). The Ophiuchus cluster was serendipitously found by Johnston et al. (1981) during their optical identifications of 4U X-ray sources. The cluster was also independently discovered by Wakamatsu & Malkan (1981) during their hidden globular cluster survey on Palomar IV-N Schmidt plates. However, since the cluster is highly obscured due to its location close to the Galactic Centre, a detailed follow up of Ophiuchus has been difficult. Nevertheless, Wakamatsu et al. (2000), motivated by their discovery, performed a deep systematic galaxy survey around Ophiuchus on existing sky survey plates. They identified clumps on the distribution of galaxies around it revealing two more clusters with highest peak density at 8500 - 9000 km s^{-1} which was enough to classify Ophiuchus as a supercluster. Using FLAIR, the multi-fibre spectroscopy system on the UK Schmidt telescope, they also uncovered a wall-like structure connecting the Ophiuchus and Hercules superclusters, the Ophiuchus-Hercules Wall which is orthogonal to the Great Wall (Fairall, 1998). In addition, Wakamatsu et al. (2005) recently speculated that there may be a contribution of the Ophiuchus supercluster to the general overdensity of the GA region as it is located close to the position of the GA, giving emphasis to the need of disclosing the entire structure around the Ophiuchus supercluster.

This is very much in agreement with our finding discussed in the previous section 4.3.2 which revealed a possible connecting feature or wall between the Norma supercluster and the

Ophiuchus cluster. Moreover, from the detections of the GB extension we are able to identify a new clump of galaxies in the vicinity of the Ophiuchus supercluster. Figure 4.19 shows the distribution of galaxies with velocities greater than 5000 km s $^{-1}$, the GB extension detections are marked by squares. A higher density of galaxies is visible above the GP in the velocity range of 8000 and 11000 km s $^{-1}$ and $l \sim 350^{\circ} - 10^{\circ}$. This seems to give a more extended feature to the Ophiuchus supercluster. The GB extension detections around the Ophiuchus region can be seen more easily in the redshift cone shown in Fig.4.20 which is the same as Fig. 4.17 but extends out to 12000 km s^{-1}. The Ophiuchus supercluster stands out clearly around 9000 km s^{-1}.

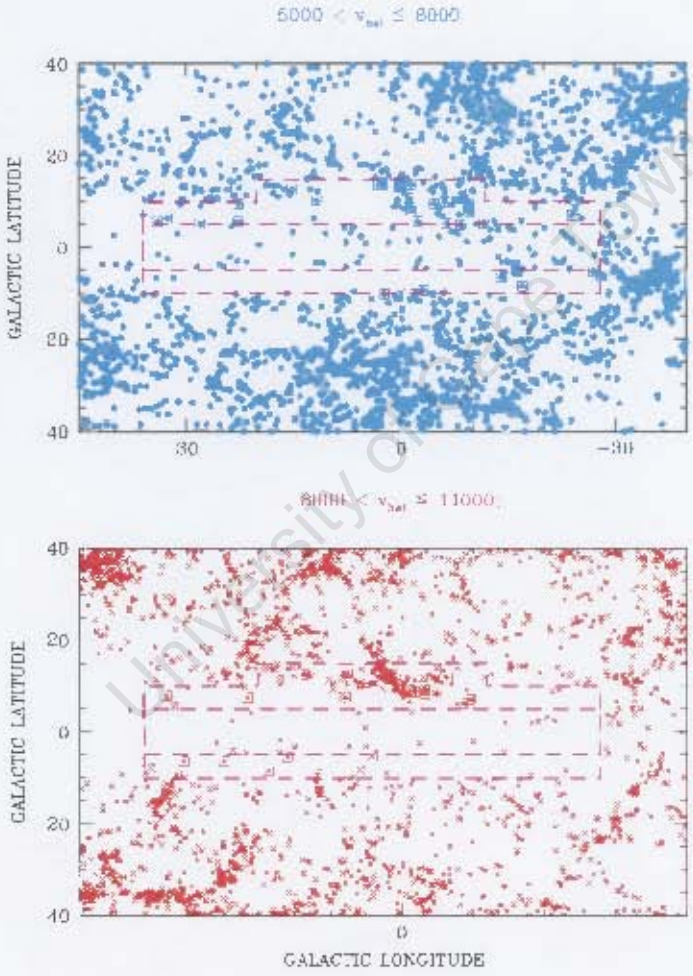

Figure 4.19: The two panels show the distribution in Galactic coordinates of the galaxies between $5000 \leq cz \leq 11000$ km s^{-1}, within intervals of 3000 km s^{-1}, detected in HIZOA, NE, GB extension and HIPASS as well as galaxies from LEDA with known velocities. The Ophiuchus supercluster is observed as clumps of galaxies around $l \sim 0^{\circ}$ and $b \sim 10^{\circ}$.

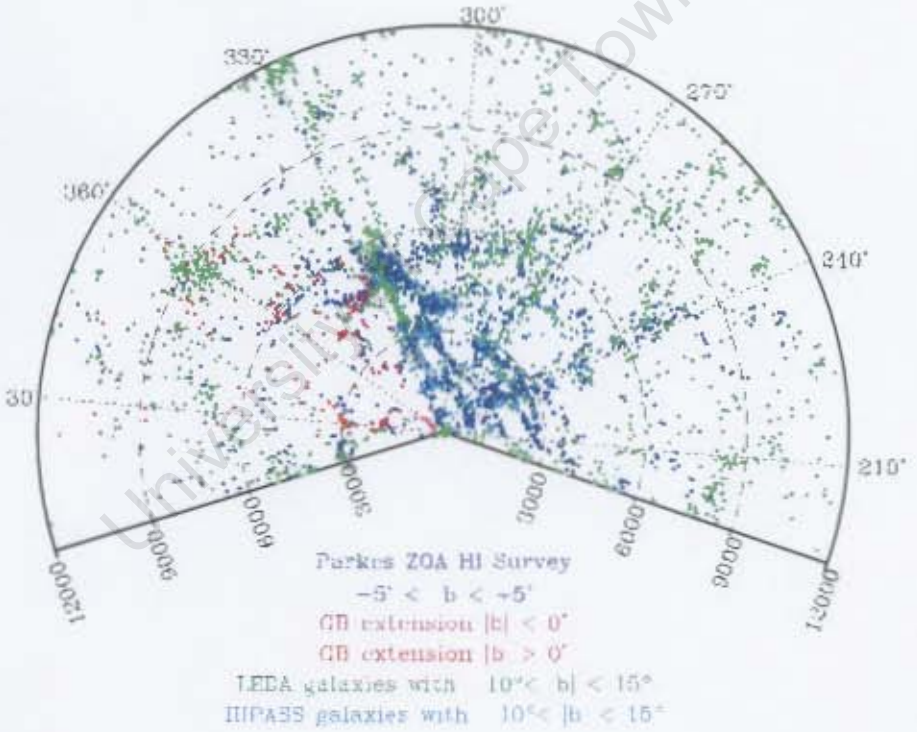

Figure 4.20: A redshift cone, out to 12000 km s^{-1}, of galaxies and candidates detected in HIZOA and northern extention surveys ($|b| \leq 5°$; blue), the GB extension ($|b| < 0°$; magenta, $|b| > 0°$; red), HIPASS (for $10° \leq b \leq 15°$; cyan and galaxies from LEDA (for $-10° < |b| < 15°$; green).

Chapter 5

Discussion and Conclusions

5.1 Summary

Because of the heavy extinction around the Galactic Bulge ($5° \leq |b| \leq 10°$), optical galaxy surveys became quite incomplete. Although NIR surveys have significantly reduced the optical ZOA, the confusion problem due to the enormous star density close to the Galactic Bulge is too severe for these surveys to remain succesful. In this region of high obscuration and confusion only systematic HI surveys have been powereful at identifiying galaxies. The Parkes Multibeam deep HI ZOA survey has been very effective in tracing large-scale structures at lower latitudes $|b| \leq 5°$ (Henning et al., 2005; Donley et al., 2005). Due to the success, and the fact that various interesting large-scale structures are partly hidden by the Galactic Bulge, the HI ZOA survey has been extended to the Bulge.

The GB extension survey has a rms of noise of ~ 6 mJy beam^{-1}, and an effective area of 800 deg^2. In this thesis, the search and HI parametrization of the galaxies found in this survey has been presented. The searching was done by visual inspection of the three-dimensional HI data cubes using the KVIS visualization tool in KARMA (Gooch, 1996), revealing 158 galaxies, 5 of which are classified as probable galaxies. The HI parameters of the galaxies were determined in a semi-automatic manner using MBSPECT task in the MIRIAD (Sault et al., 1995). Of the 158 galaxies and candidates detected here, 93 (51%) are new detections, the rest have catalogued multiwavelength counterparts (see Table 3.5).
The spatial and velocity distribution of the GB extension galaxies have been analyzed in this thesis. The distribution of these galaxies in combination with previously catalogued HI and optical galaxies a number of large-scale structures became apparent. The results are summerized as follows:

- The distribution of the nearby GB extension galaxies in the region $l \sim 330° - 45°$ provided a broader delineation of the Local Void. The Local Void has been observed as underdense region extending up to $cz \sim 6000$ km s^{-1}. But a filamentary feature is found at ~ 3000 km s^{-1} which seems to divide the void into two components. Neither of these voids are completely empty of galaxies though. Some very low mass galaxies have been found in these regions.

- In the distribution of galaxies between 4000 and 6000 km s^{-1}, the GB extension data revealed for the first time the presence of a new "second arm" to the Norma supercluster. This wall-like structure, parallel to the GA-Wall, stretches from the Centaurus cluster down to higher longitudes crossing the Galactic Plane at $l \sim 345°$. This new feature contribute to the mass of the GA overdensity.

- A filamentary structure that crosses into the GA-Wall at the location of the Norma supercluster has been identified in this data. This filamentary feature seems to stretch into the distant Microscopium void at $(l, v) \sim 350°, 4500$ km s^{-1} and $340°, 5000$ km s^{-1} towards the Ophiuchus supercluster. Since this connection is only weakly seen, further observations are require to confirm this possible connection between the Norma supercluster and the Ophiuchus cluster.

- At larger distances, between 8000 and 10000 km s^{-1} and $l \sim 350° - 10°$, $b \sim 10°$ we observed a high concentration of galaxies around the Ophiuchus supercluster. This concentration seem to extend out 11000 km s^{-1}.

Based on the GB extension survey and this study, it can be concluded that (1) the Local Void consists of a large underdense region out to $cz \lesssim 6000$ km s^{-1} extending from $l \sim 345°$ to 45° and $b \sim -30°$ to +45° which is larger than previously thought and it is not entirely empty–few extremely low mass galaxies have been found in the void (2) with the new second parallel wall and the possible connection of the Norma supercluster and the Ophiuchus cluster, the mass contributing to the GA overdensity could be much larger than previously assumed.

5.2 Work ongoing

Although the HI content of our galaxies has been studied, no information is available at other wavebands. A NIR follow up of the characterstics of HI detected galaxies in the ZOA is currently being pursued. A systematic study of the global properties of these galaxies is important to determine their morphology and luminosity. The dependence of density on the surrounding environment can be verified by studying the characterstics of the galaxies found around and within the Local Void. This work is currently proceeding using IRSF.

Appendix A

Automatic Galaxy Search in the GB extension Data

As a test of the recently released automatic source finder software, DUCHAMP (Whiting, 2007), galaxy search was done in 4 GB extension data cubes (Z008N, Z016N, Z024N and Z032N) that have been trimmed to remove edge noise. The algorithm, DUCHAMP, is named after the cubist and one of the first artists to work with "found objects", Marcel Duchamp. DUCHAMP is designed to search for relatively small objects found in the region of high noise. Duchamp detects signal above a certain flux cutoff over two or more connected pixels.

Choosing a peak flux density cut-off 24 Jy beam^{-1}, DUCHAMP was run over the 4 cubes. The resulting detections were then compared with a search result obtained from visual inspection of the data cubes. DUCHAMP produced a very large number of detections in each cube. For instance, for cube Z032N the number of detections in DUCHAMP was about 3 times that of the result obtained by human searching. In Fig. A.1 examples of DUCHAMP detections in this cube is shown. Although the number of detections is larger, there were a number of visual detections that were not picked up by Duchamp. From the detections shown in Fig. A.1, only J181921+011011 (#004), J182635+01330 (#006), J182459-012106 (#007), J182324+001835 (#009) and J182639+030320 (#010) are considered as real galaxies.

The efficiency of DUCHAMP detecting the GB extension galaxies in the 4 cubes is shown in Fig. A.2. From this plot we can say that about half of the detections with signal-to-noise, $S/N_{\max} \gtrsim 5$, are real detections. The others are spurious noise peaks, or interference. The latter could be due to the high S/N objects.

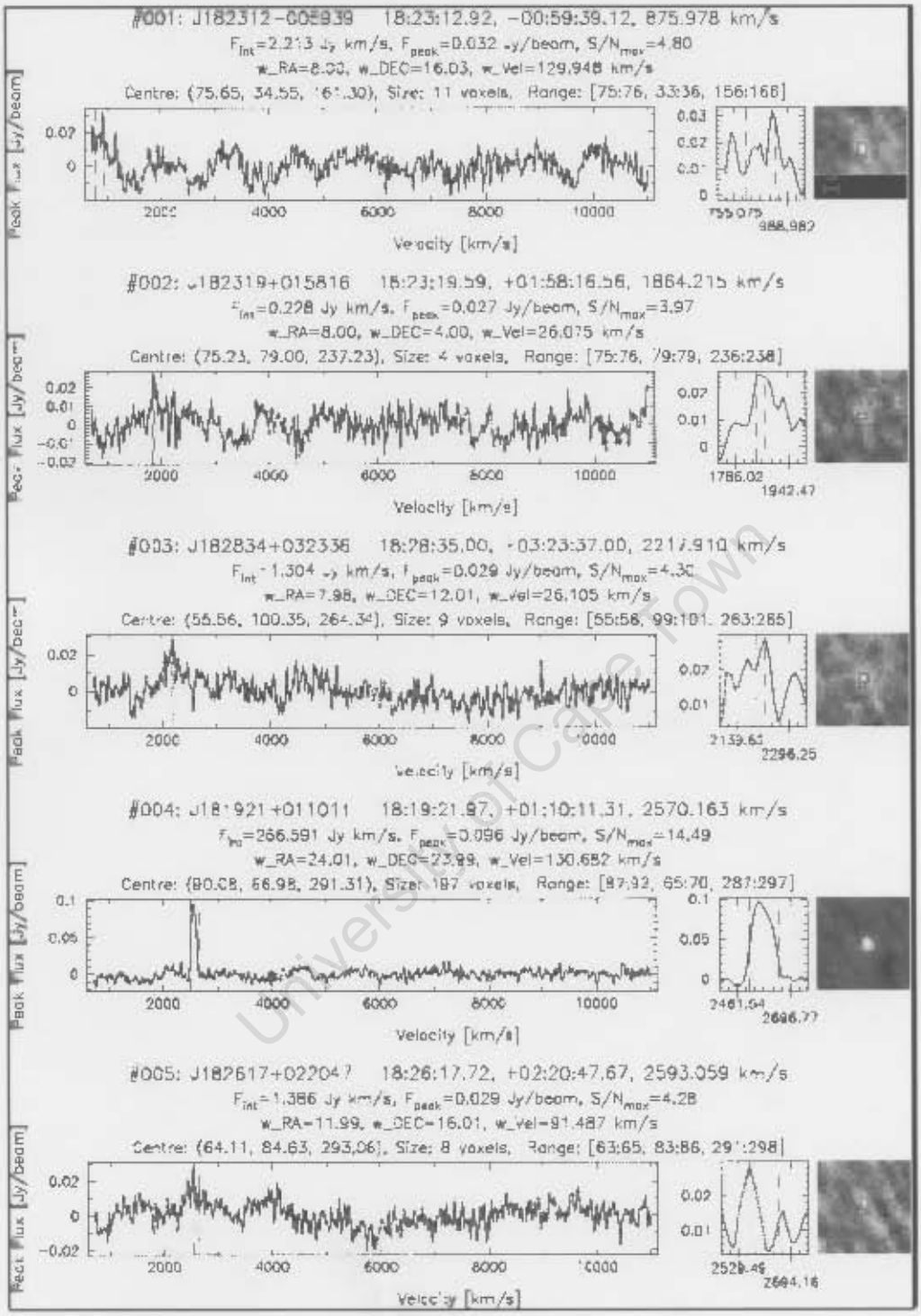

Figure A.1: Examples of DUCHAMP detections from the GB extension Z032N data cube

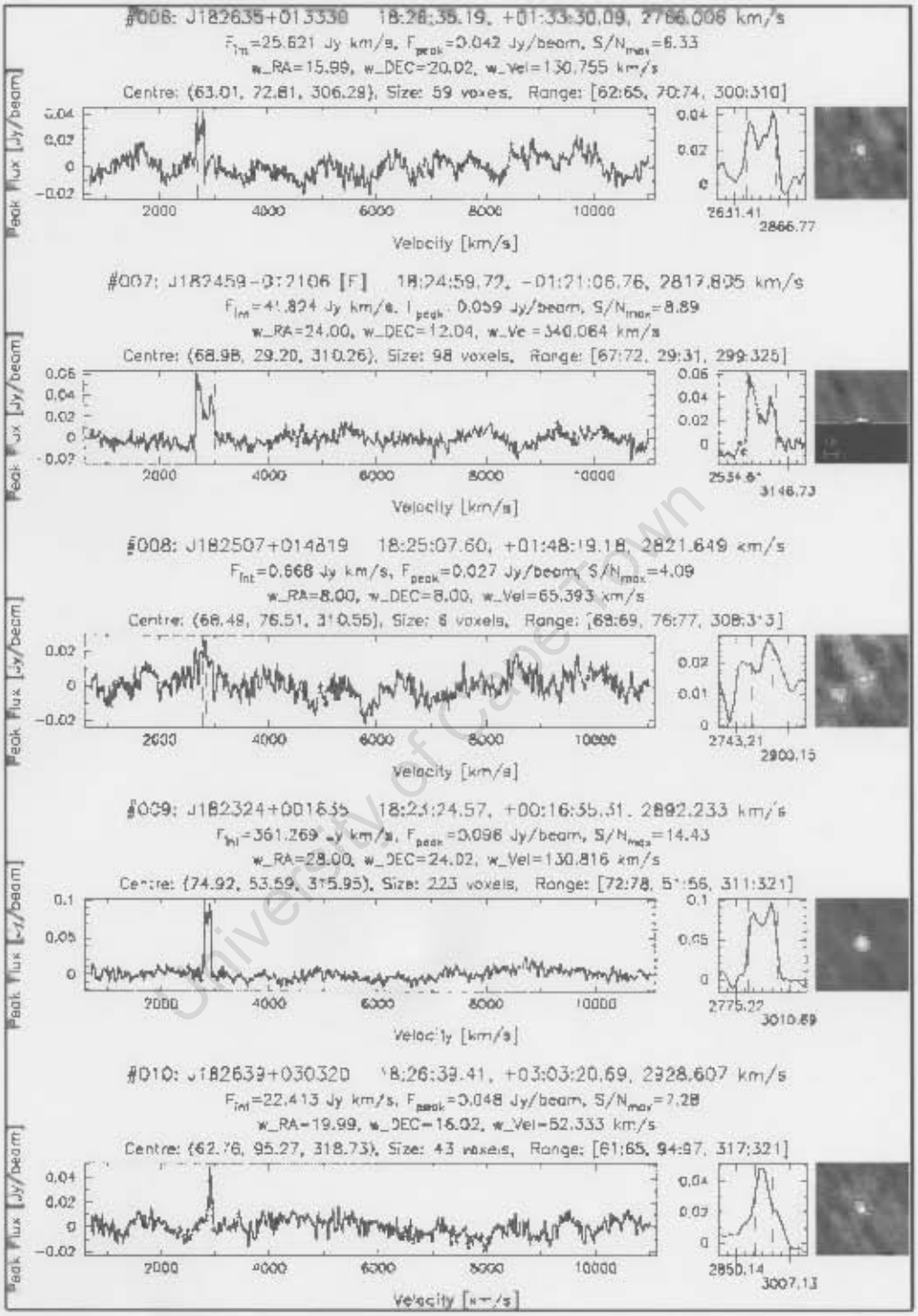

Figure A.1: Continued

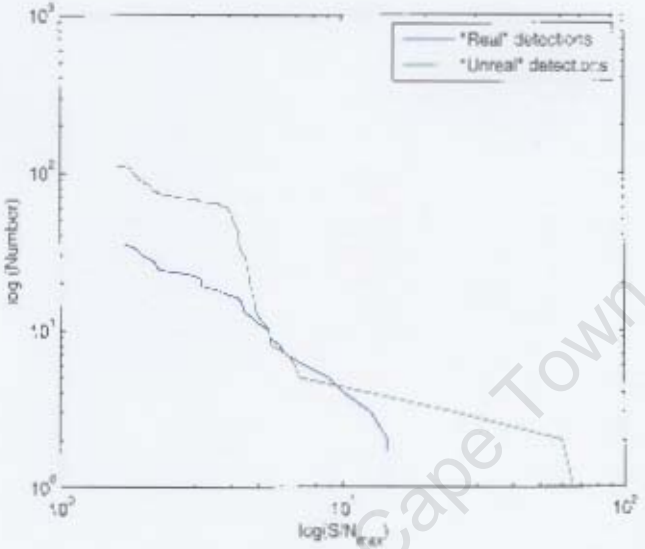

Figure A.2: The efficiency of DUCHAMP in 4 cubes of the GB extension, $S/N_{\rm max} \gtrsim 5$ are real detections.

Appendix B

Possible counterparts with no Measured Velocities

The J-H-K_s composite images of galaxies in the 2MASS Extended Source Catalog (2MASX; Jarrett et.al, 2000a,b) that are found within $4'$ radius of the HI position and which have no redshift measurement are presented in the following Figs. B.2 - B.6. Since insufficient information was available to decide whether they are real counterparts of the HI detected galaxies, a rough morphological argument was used to consider them as possible counterparts. The HI parameters, with extinction $E(B-V)$ (Schlegel et.al, 1998) at the the position, and profiles of the GB extension galaxis' are shown for comparison of the galaxies morphology.

Source name	RA (J2000)	Dec (J2000)	$E(B-V)$	V_{hel} (km s^{-1})	W_{20} (km s^{-1})	S (Jy km s^{-1}	log M_{HI} ($M_\odot$)
J1644-55	16 44 27.04	–55 29 49.7	0.35	5114	482	23.62	10.37

The 2MASS galaxy, 2MASX J16441750-5529172, is found at a separation, $r = 1'.4$ from the HI J1644-55 detected galaxy. We see a massive edge-on spiral galaxy on the 2MASS composite image (upper right panel of Fig. B.1). The HI spectrum profile of J1644-55 (lower panel of Fig. B.1) shows a double-horn profile of a typical edge-on spiral galaxy. The large W_{20} and large HI mass of the galaxy also confirm its extensive mass. An optical counterpart, ESO 179- G 012, (Lauberts, 1982) with a matching redshift has also been found within the $4'$ search radius. The DSS2 red image of this galaxy is shown (upper left panel of Fig. B.1) to strengthen the morphological type agreement. This morphological type agreement between the 2MASS galaxy and the HI detected galaxy put the 2MASX J16441750-5529172 as a possible counterpart.

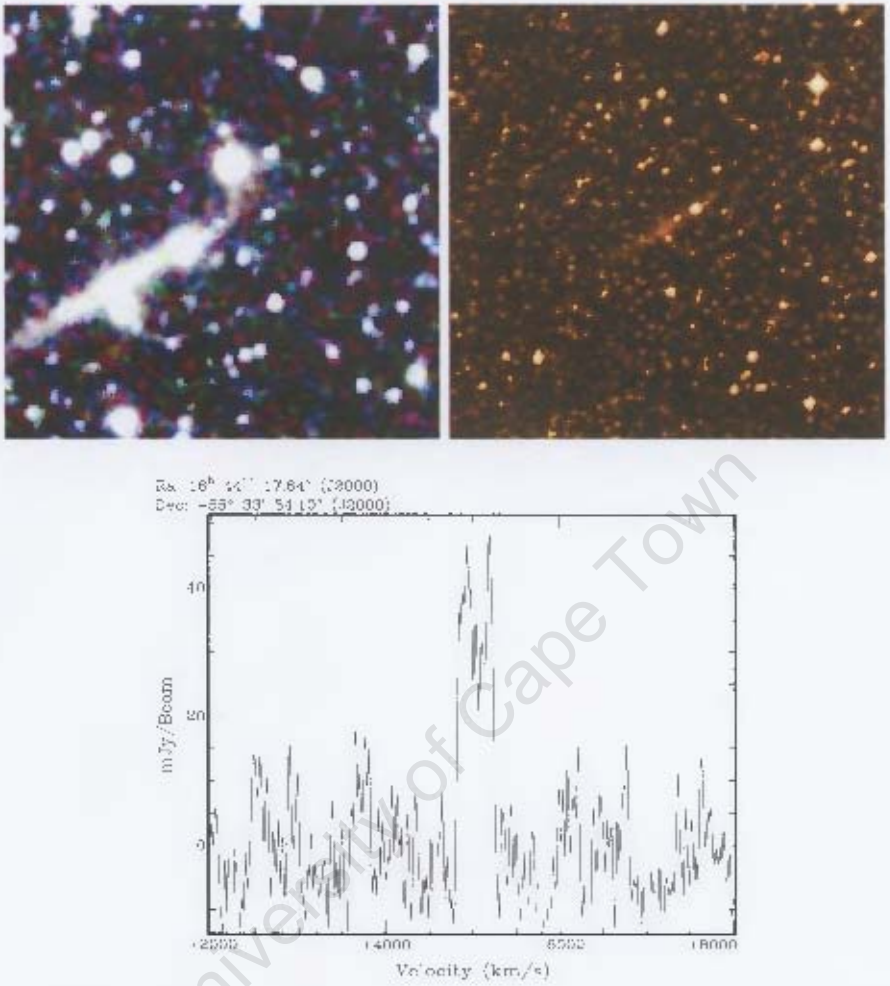

Figure B.1: Image of 2MASX J16441750-5529172 (left panel) [$1'.2 \times 1'.2$] and ESO 179- G 012 (right panel). The bottom panel shows the HI profile of J1644-55.

Source name	RA (J2000)	Dec (J2000)	$E(B-V)$	V_{hel} (km s^{-1})	W_{20} (km s^{-1})	S (Jy km s^{-1}	log M_{HI} ($M_{\odot}$)
J1556-42	15 56 37.62	42 34 10.8	0.87	5755	120	5.56	9.88

The 2MASS galaxy, 2MASX J15565765-4234517, has been found at $r = 0'.7$ from the HI position of J1556-42. The J-H-K_s composite of this galaxy and the HI spectrum of profile of J1556-42 are shown in Fig. B.2. 2MASX J15565765-4234517 has been classified as Irs on NED. The Gaussian spectrum profile of J1556-42 shown in Fig. B.2 (bottom right) also shows a typical irregular galaxy spectrum profile. This is very much in agreement with the given morphology of 2MASX J15565765-4234517.

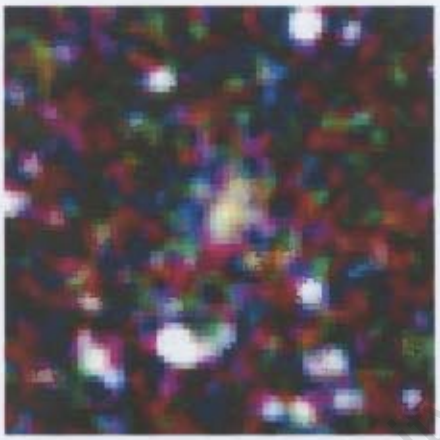

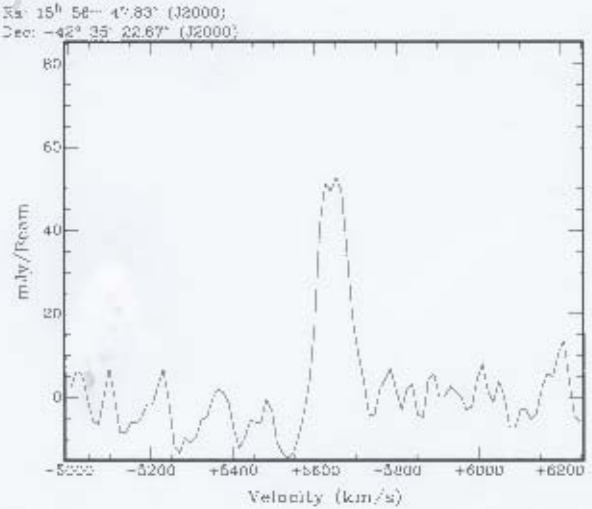

Figure B.2: Image of 2MASX J15565765-4234517 [$2'.3 \times 2'.3$] and the HI profile of J1556-42.

Source name	RA (J2000)	Dec (J2000)	$E(B-V)$	V_{hel} (km s^{-1})	W_{20} (km s^{-1})	S (Jy km s^{-1}	log M_{HI} ($M_\odot$)
J1616-40	16 16 07.96	-40 02 04.3	0.99	1438	378	15.71	10.12

J1616-40 has a possible 2MASS counterpart within a 4′ radius of the HI position. The image of the 2MASS galaxy, 2MASX J16161676-4003142 is shown in Fig. B.3 (upper). The HI spectrum profile of J1616-40 (lower panel of Fig. B.3) shows a double-horn profile of a typical edge-on spiral galaxy.

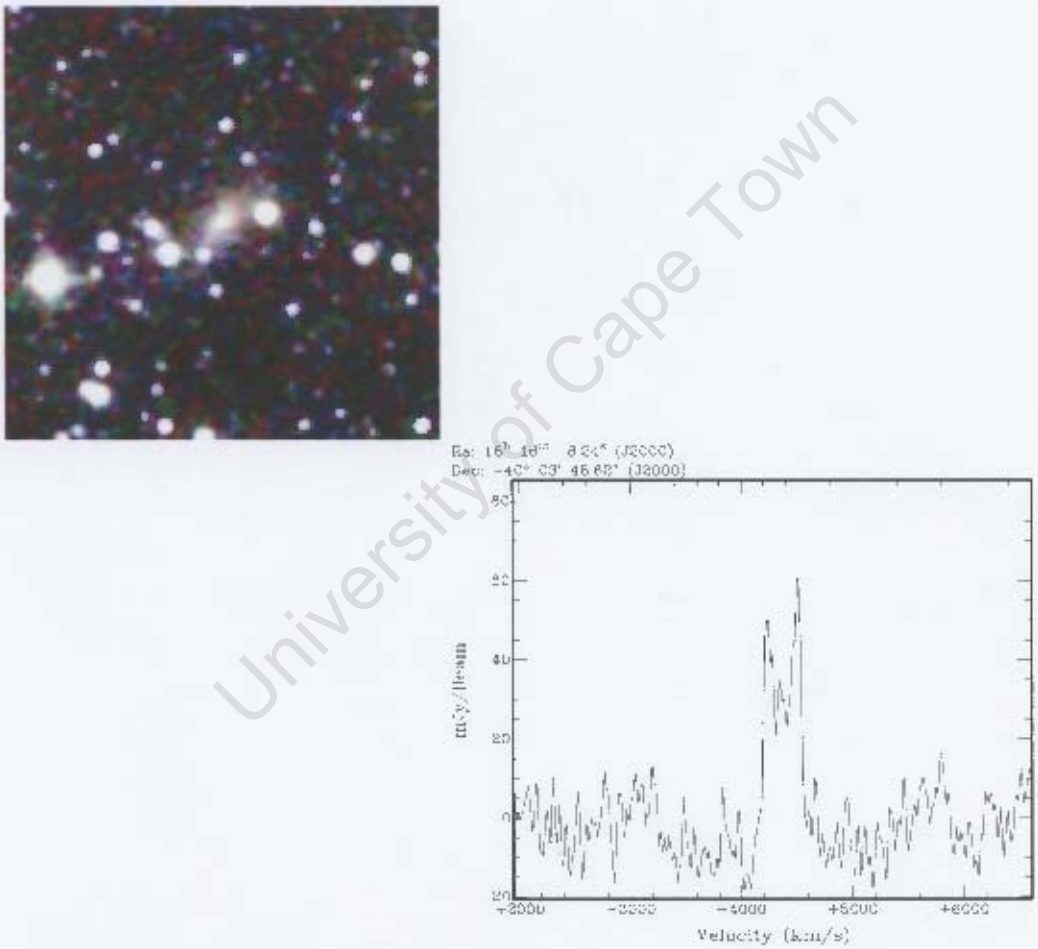

Figure B.3: Three color mage of 2MASX J16161676-4003142 [0′.6 × 0′.6] and the HI profile of J1616-40.

Source name	RA (J2000)	Dec (J2000)	$E(B-V)$	V_{hel} (km s^{-1})	W_{20} (km s^{-1})	S (Jy km s^{-1}	log M_{HI} ($M_\odot$)
J1702-27	17 02 25.98	−27 50 11.7	0.33	4546	141	3.78	9.53

Fig. B.4 (top right) shows the 2MASS galaxy, 2MASX J17023181-2750389 found at $r = 1'.4$ from the HI galaxy J1702-27. This galaxy was classified as Irs on NED. The HI spectrum profile of J1702-27 is also shown Fig. B.4 (bottom left). The Gaussian spectrum profile and the narrow velocity width of J1702-27 show that it is a tipcal irregular galaxy. This agrees very well with the morpological type of 2MASX J17023181-2750389.
J1702-27

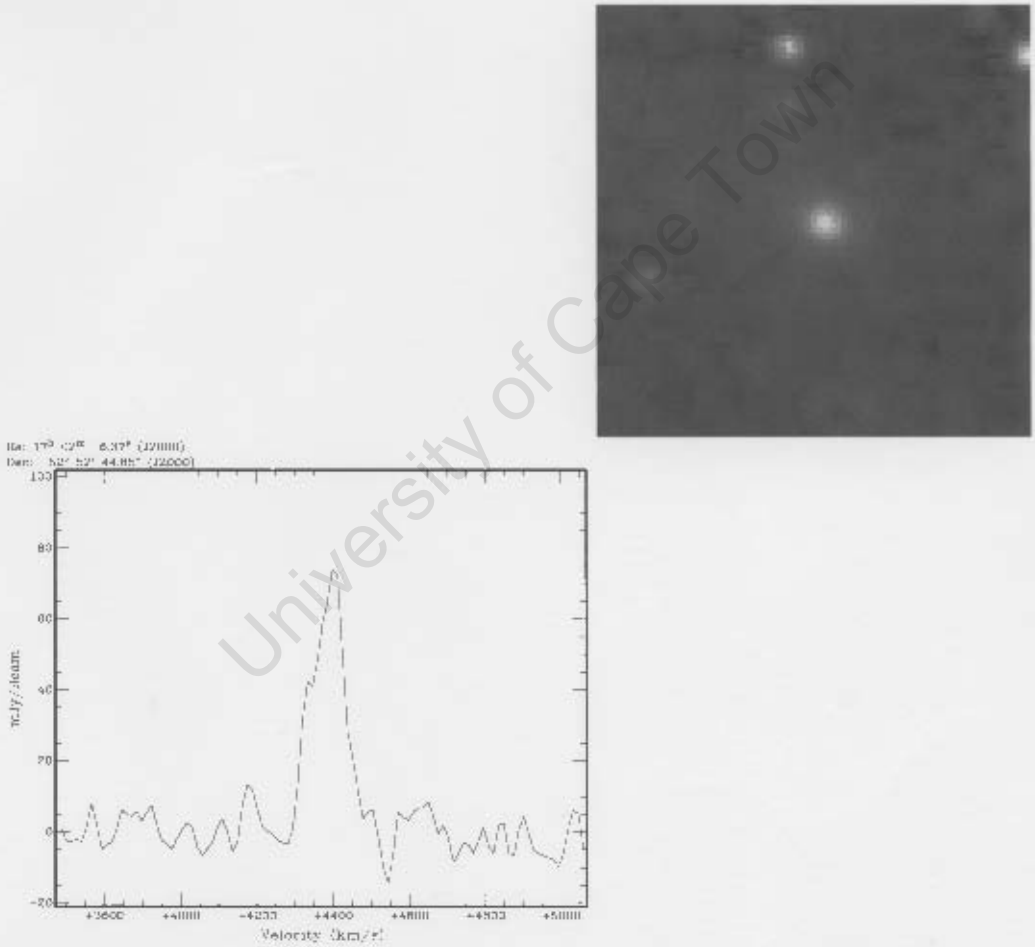

Figure B.4: Three color image of 2MASX J17023181-2750389[$0'.8 \times 0'.8$] and the HI profile of J1702-27.

Source name	RA (J2000)	Dec (J2000)	$E(B-V)$	V_{hel} (km s^{-1})	W_{20} (km s^{-1})	S (Jy km s^{-1})	log M_{HI} ($M_\odot$)
J1708-25	17 08 25.54	-25 45 16.2	0.468726	550	7.94	10.41	

On the composite image of 2MASX J17082540-2543541 (the upper right panel of Fig.B.5) we see more than one object. The HI spectrum profile of J1708-25 B.5 (bottom left) also indicates the detection of possibley two spiral galaxies. The large W_{20} and large mass also support the possible detection two galaxies.

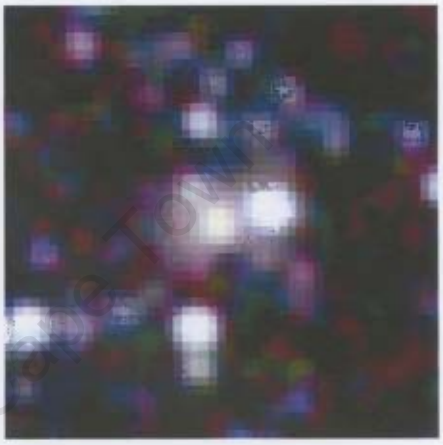

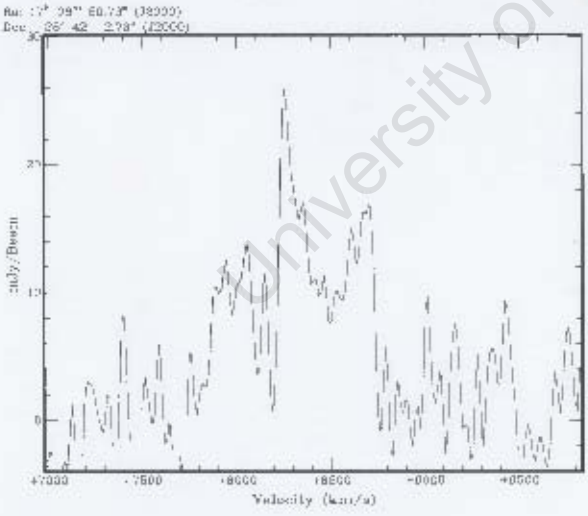

Figure B.5: Three color image of 2MASX J17082540-2543541 [1′.5 × 1′.5] and the HI profile of J1708-25.

Source name	RA (J2000)	Dec (J2000)	$E(B-V)$	V_{hel} (km s^{-1})	W_{20} (km s^{-1})	S (Jy km s^{-1}	log M_{HI} ($M_\odot$)
J1744-09	17 44 6.62	09 21 15.3	0.87	4245	260	5.87	9.68

The 2MASS galaxy 2MASX J17440232-0921440 is shown in Fig. B.6 (upper right). A faint spiral galaxy is visible on this image. The HI spectrum profile of J1744-09 B.6 (bottom left) also shows a double-horn profile of a typical edge-on spiral galaxiy.

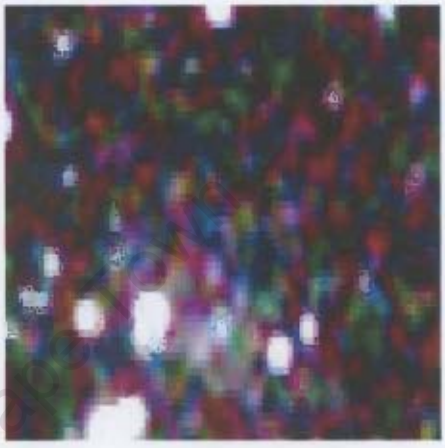

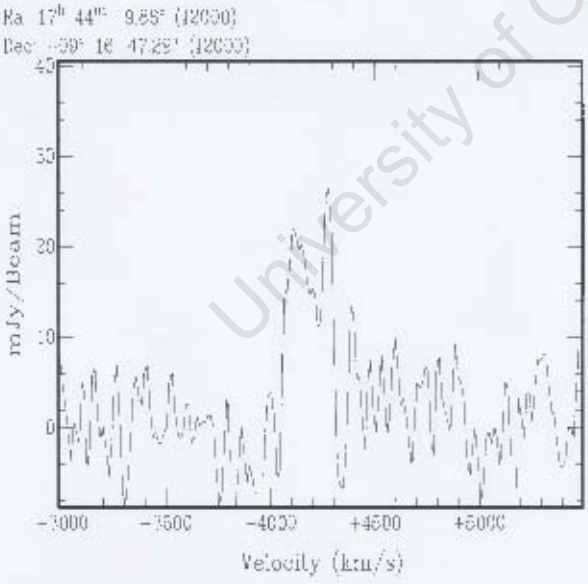

Figure B.6: Three color image of 2MASX J17440232-0921440 [$1'.5 \times 1'.5$] and the HI profile of J1744-09.

Appendix C

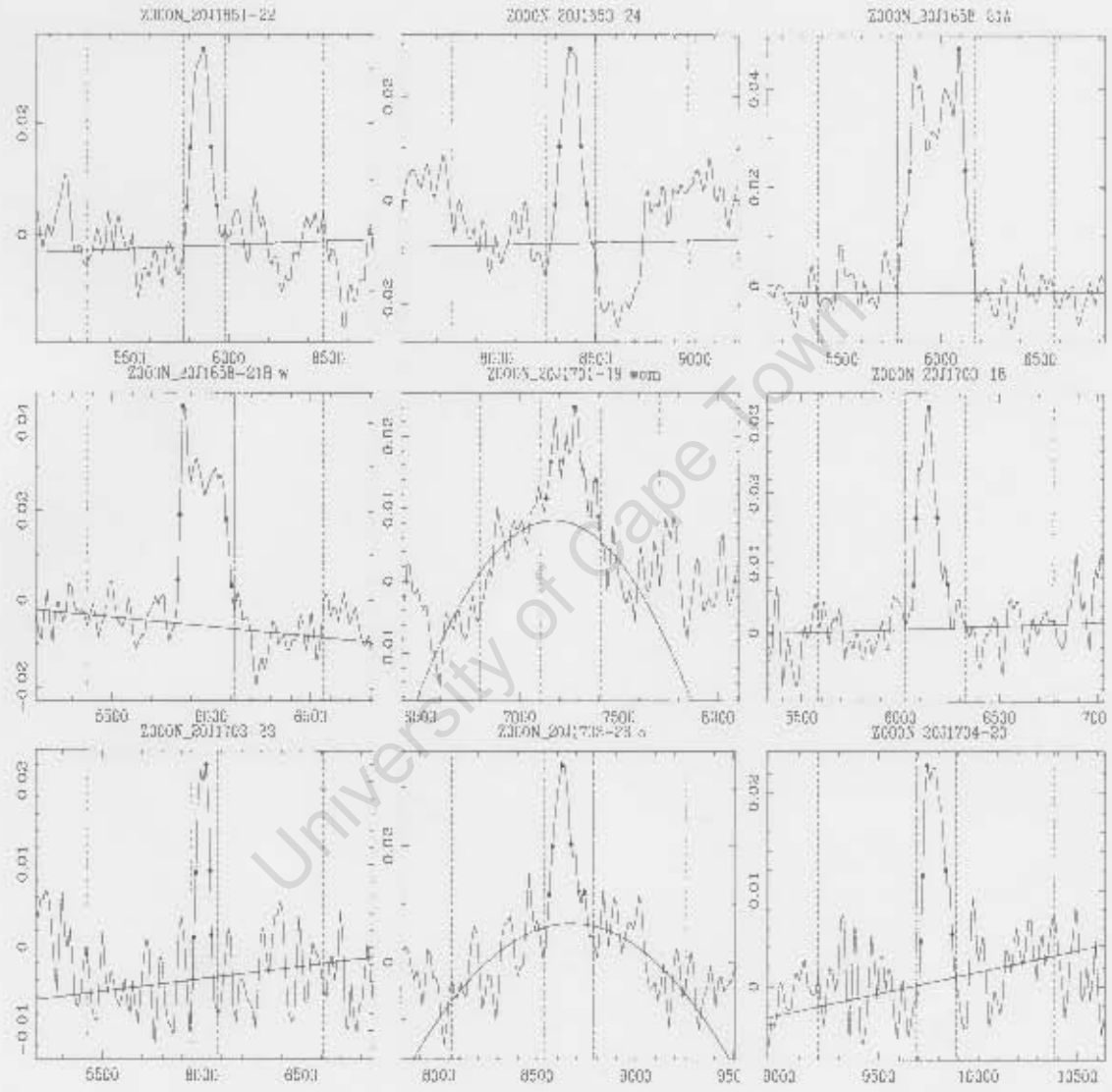

Figure C.1: HI spectra of the GB extension galaxies shown as Flux density (Jy) against Velocity (km s^{-1}). The inner dotted lines indicate the velocity range over which the candidate profile was measured, whereas the outer dotted lines indicate the region over which the baseline was fitted.

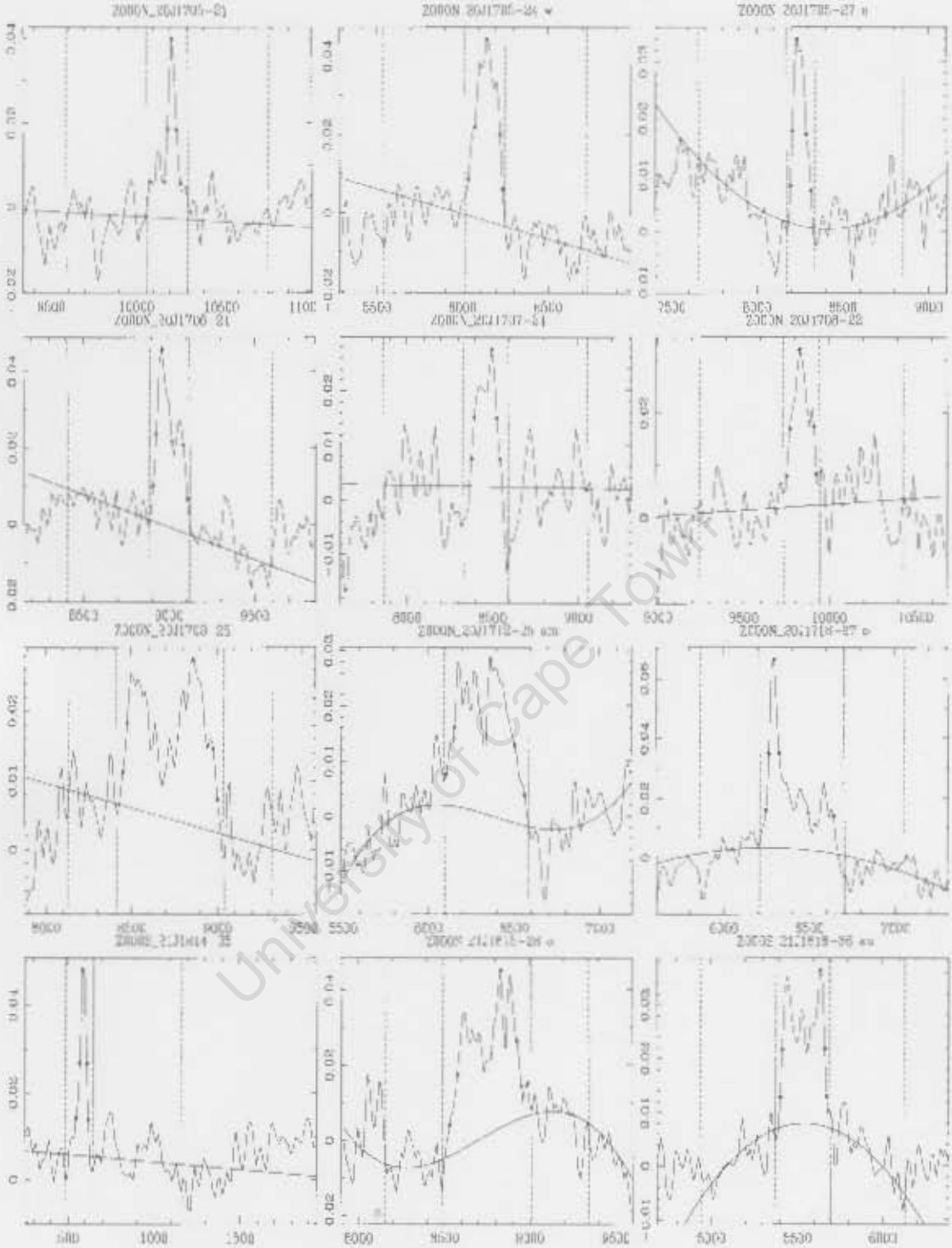

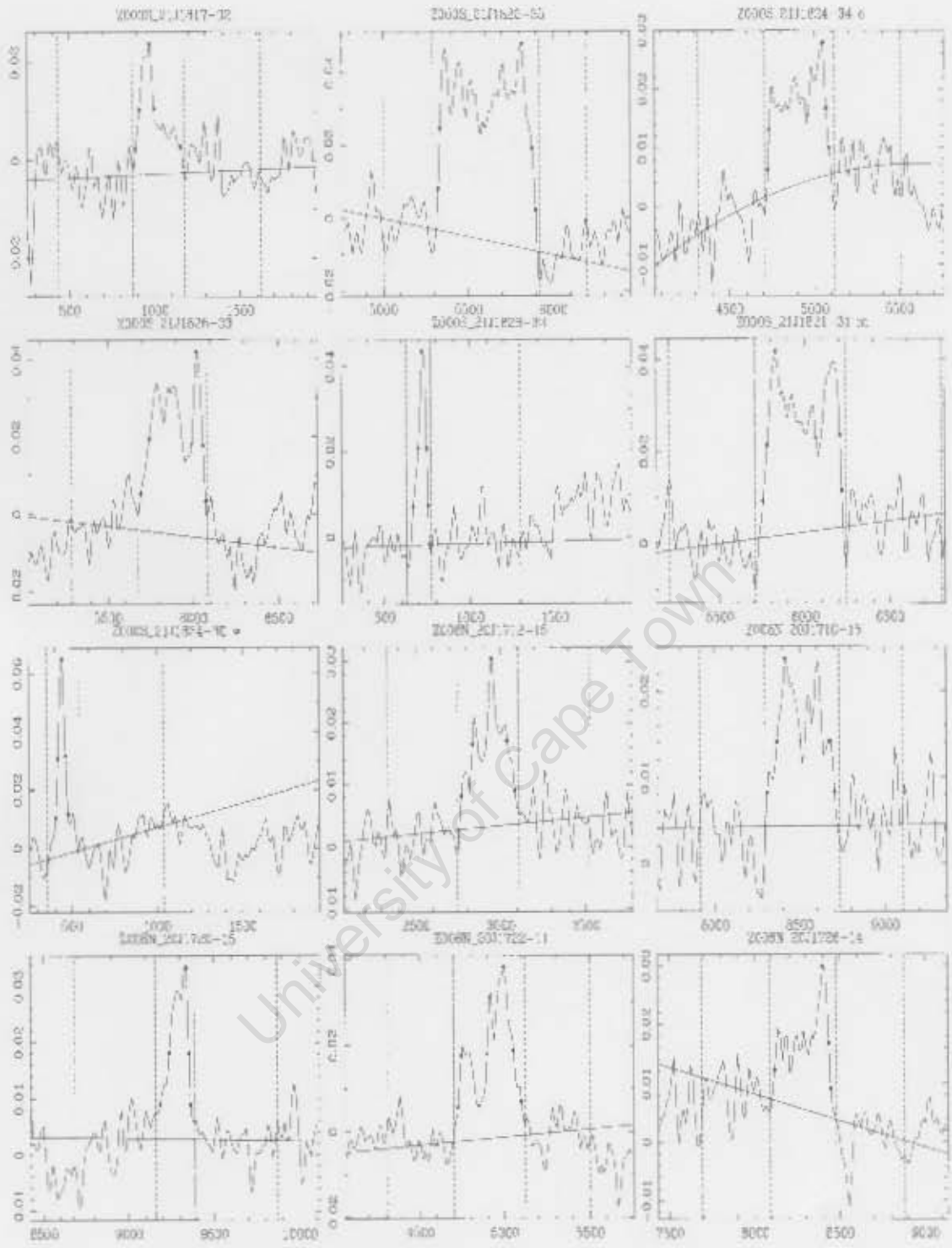

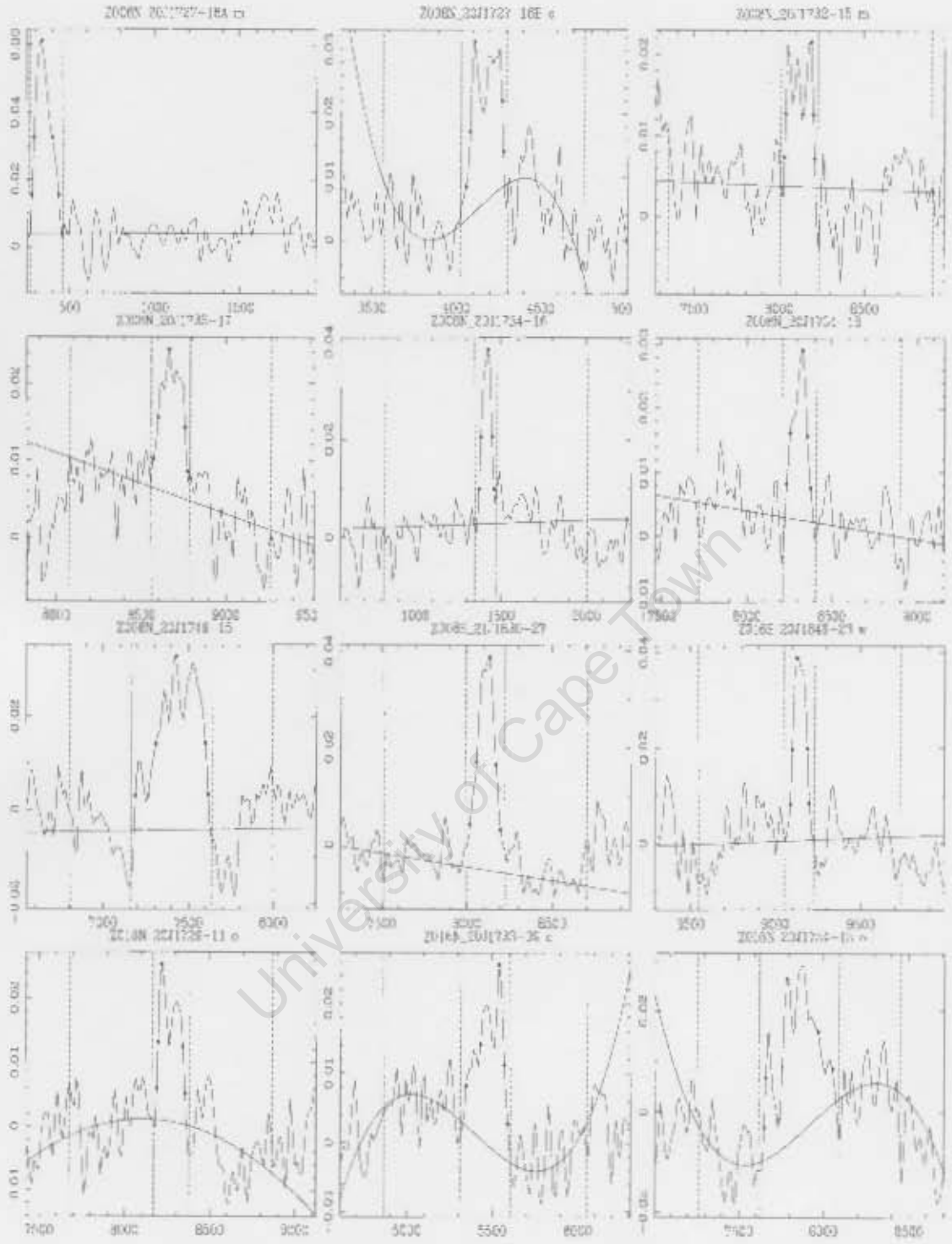

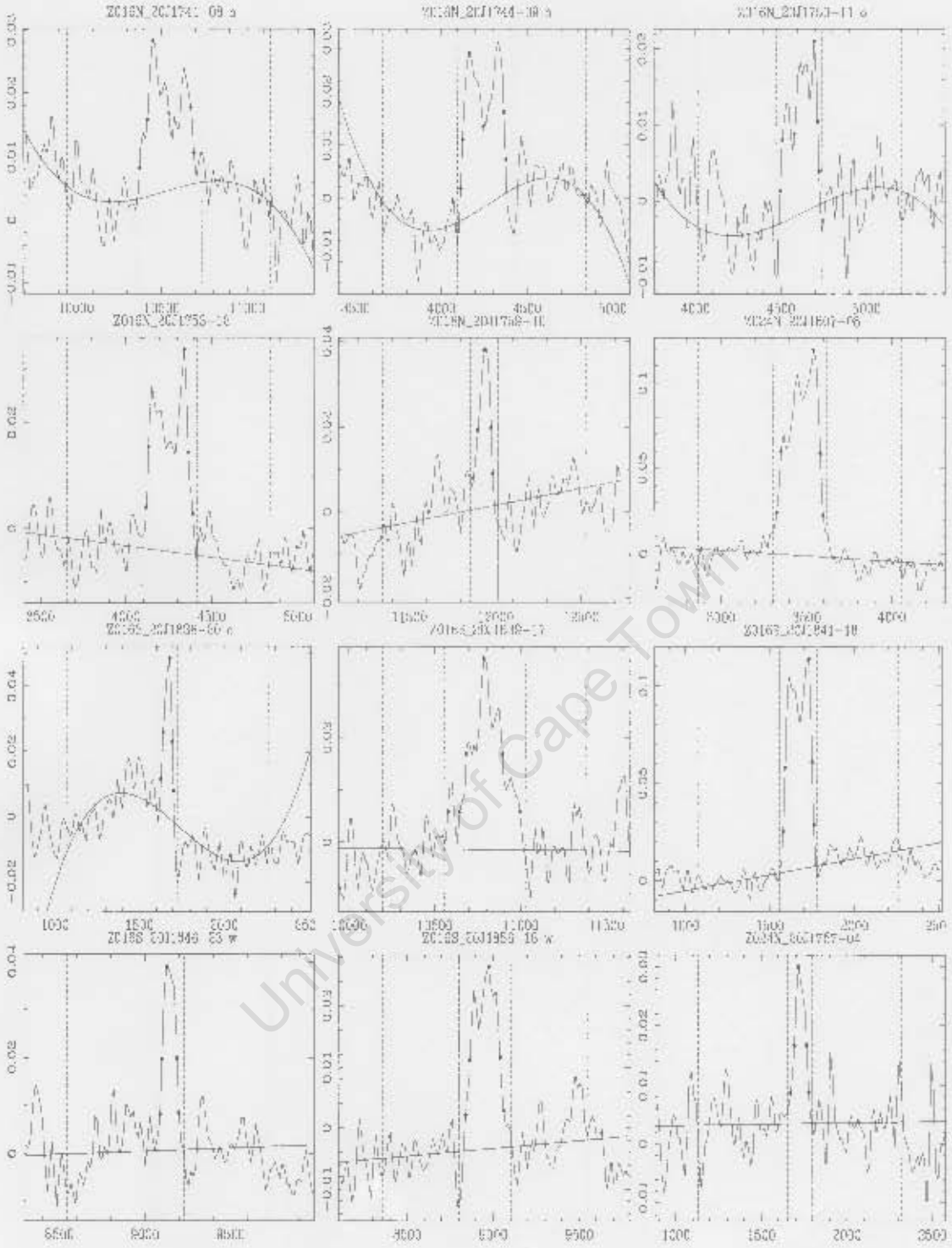

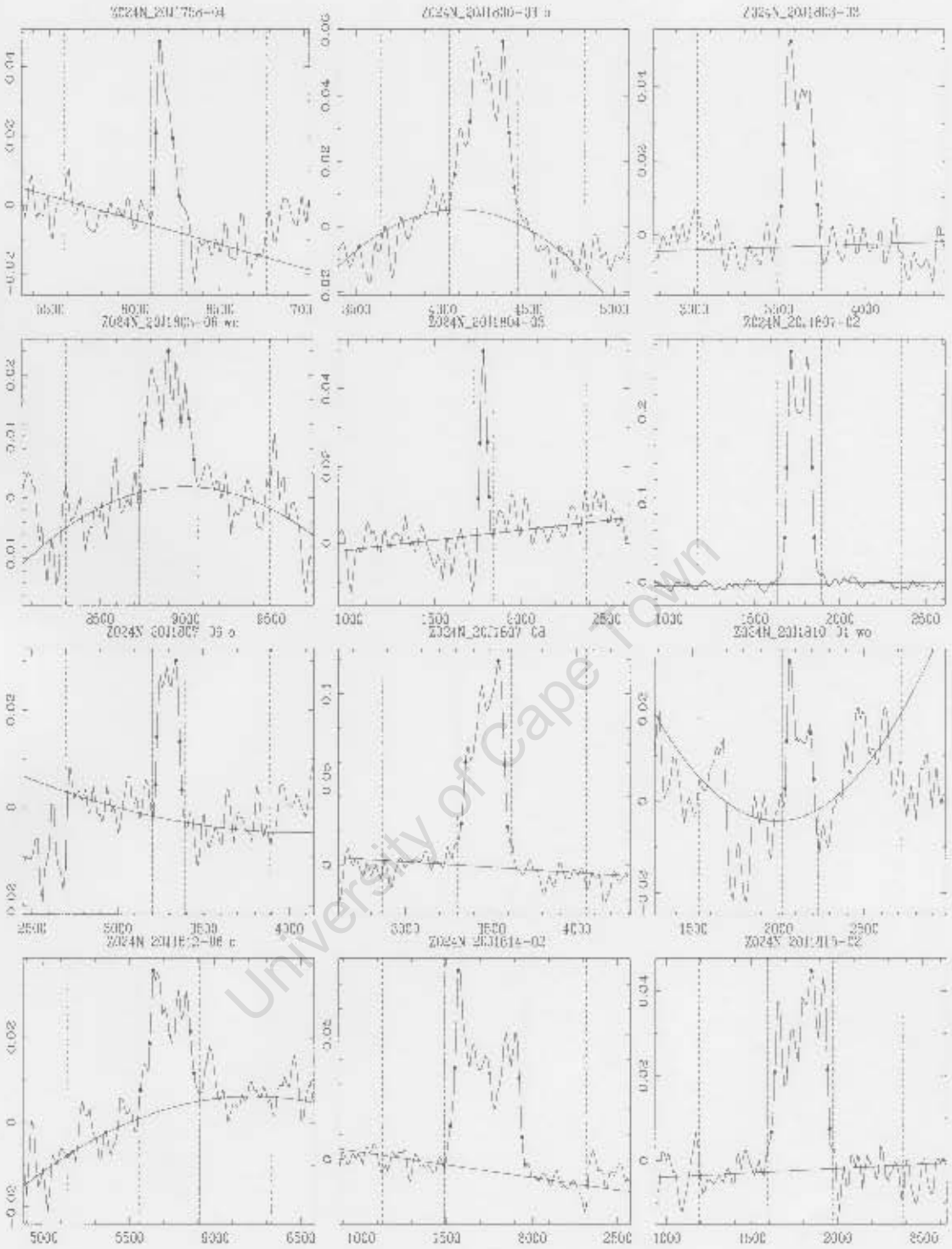

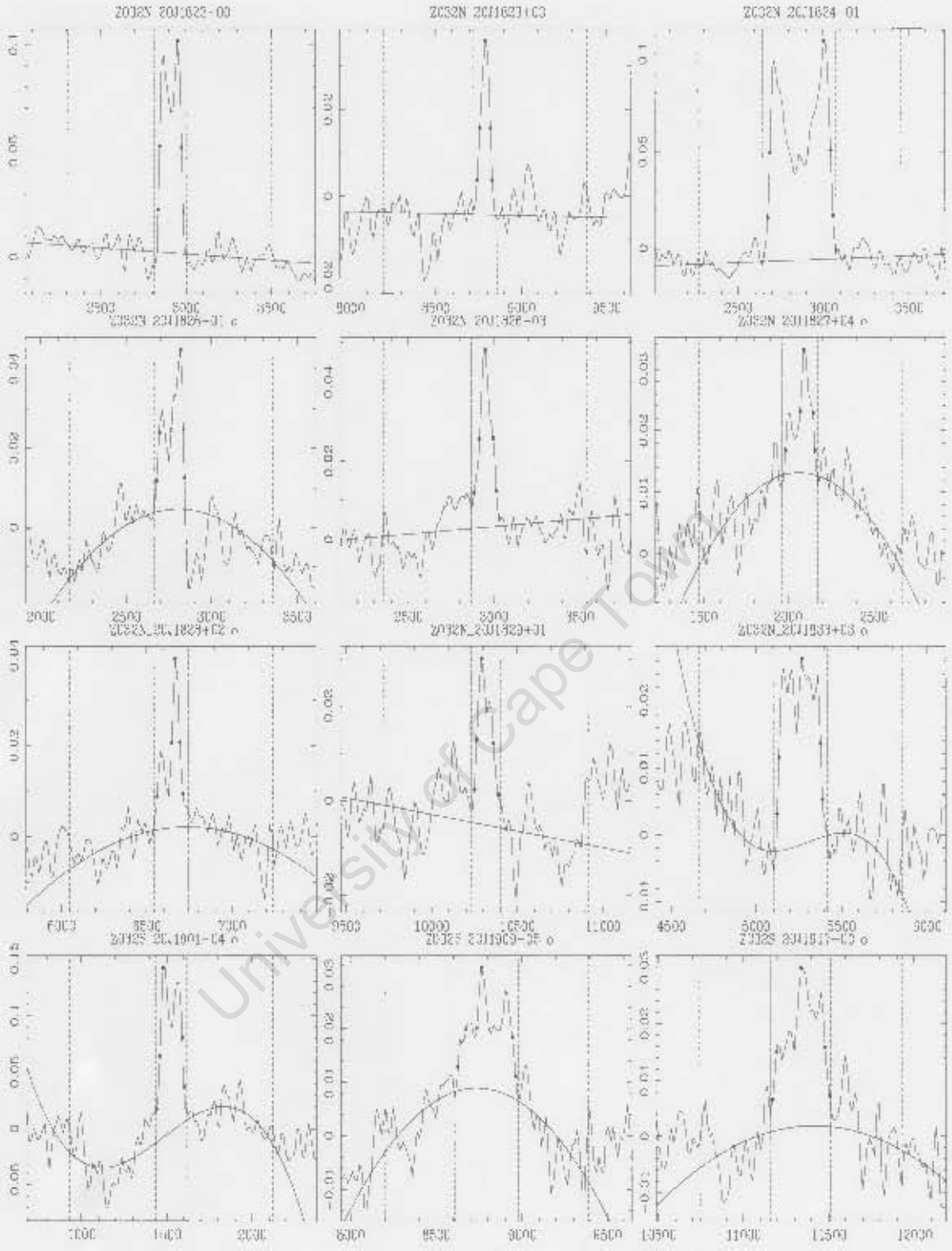

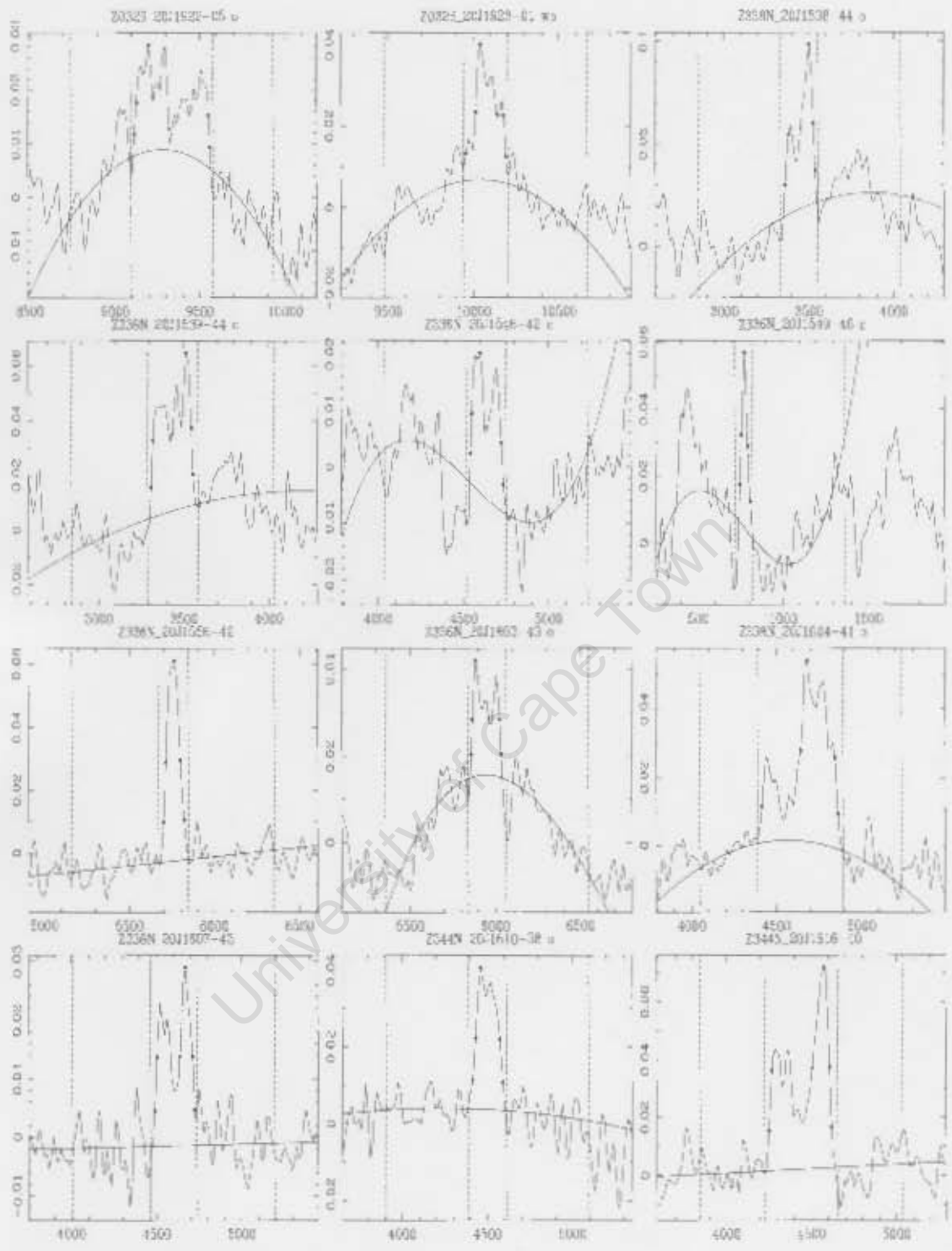

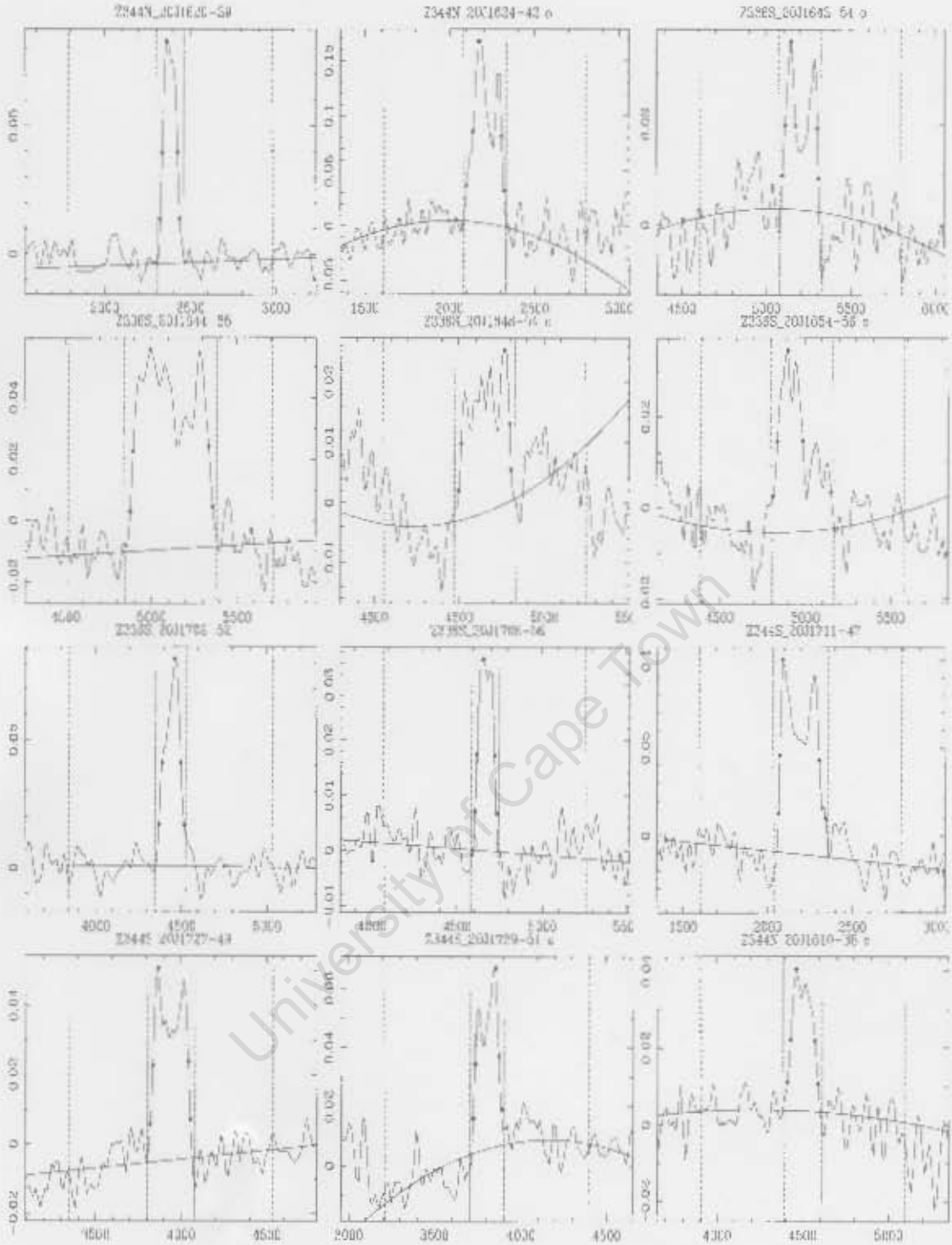

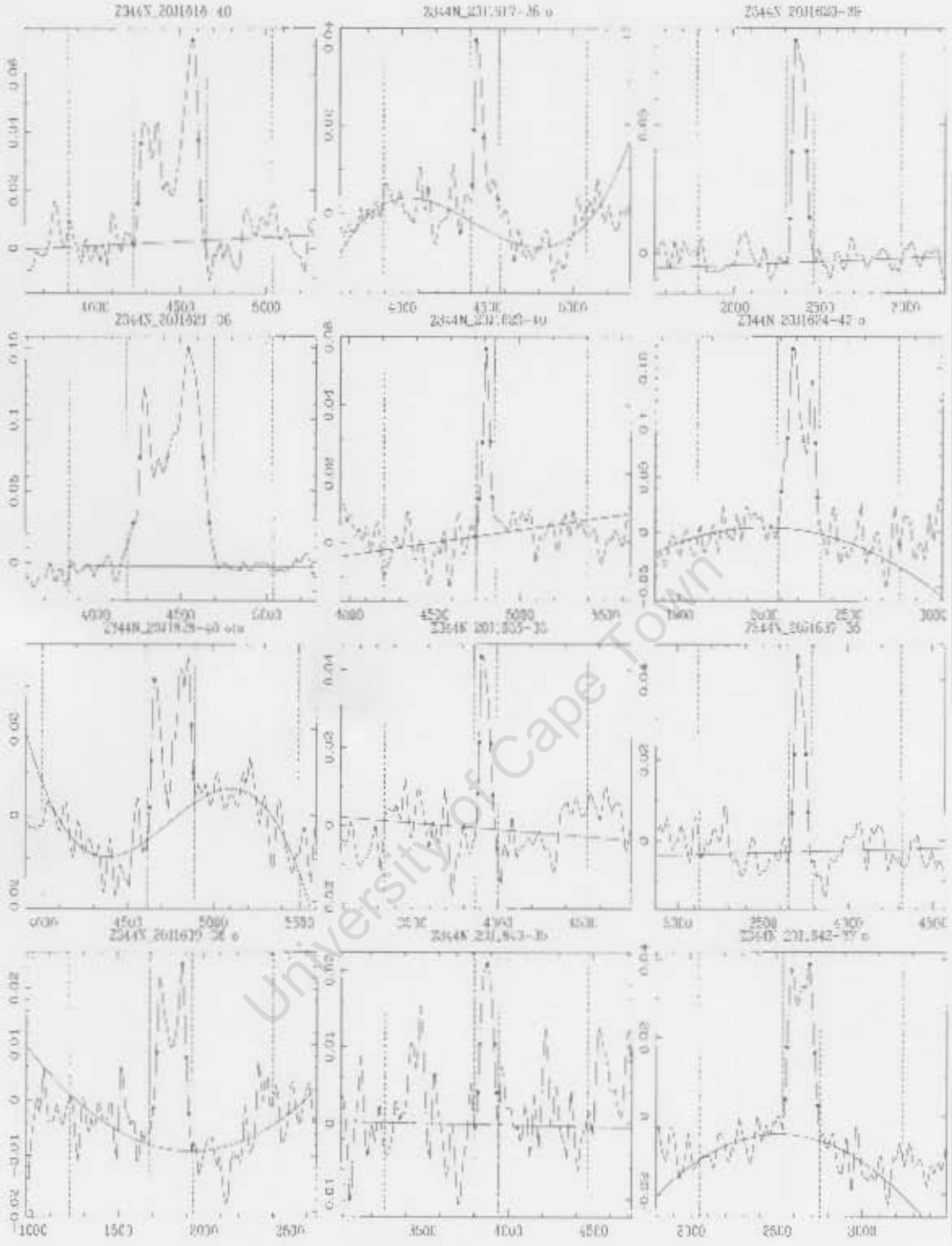

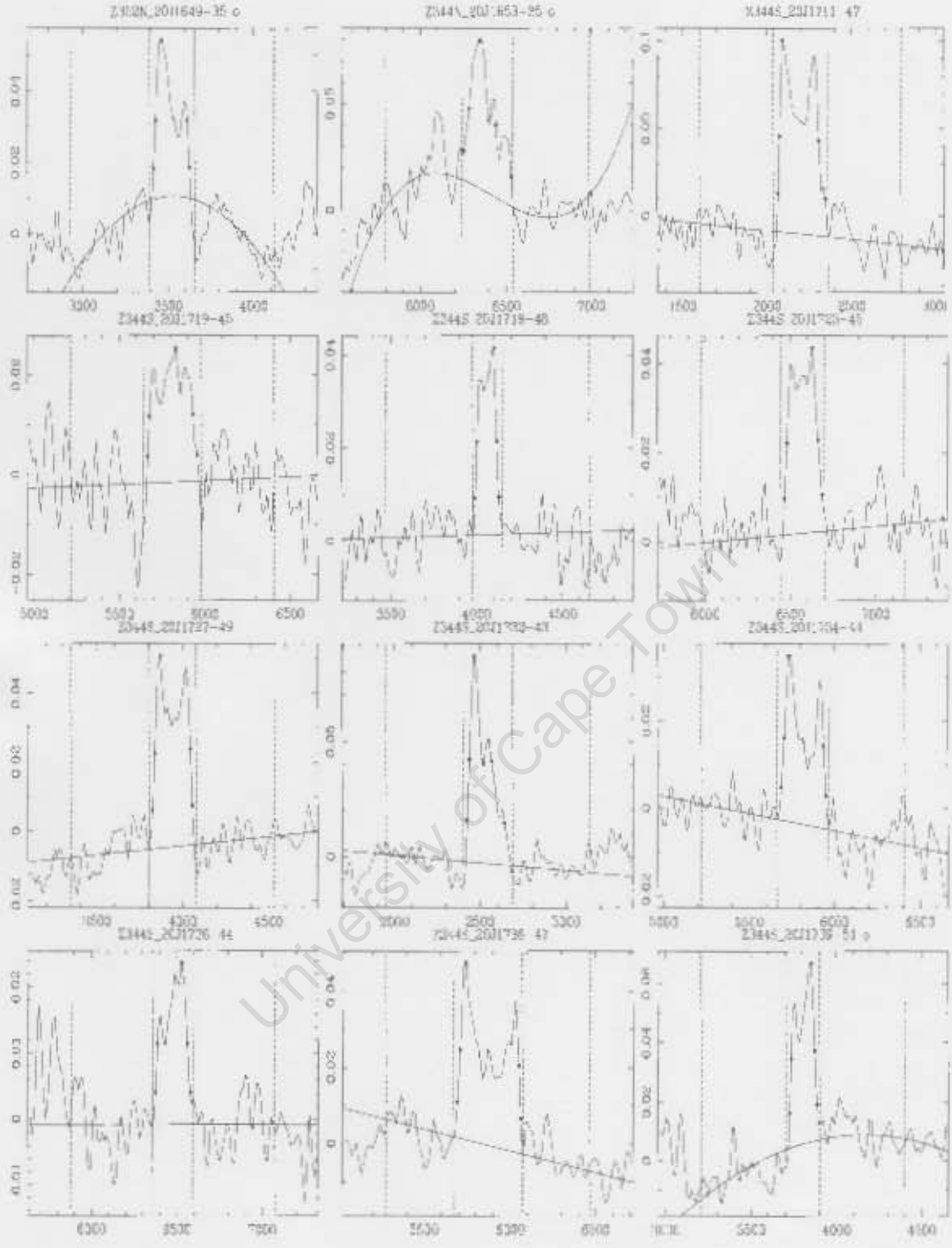

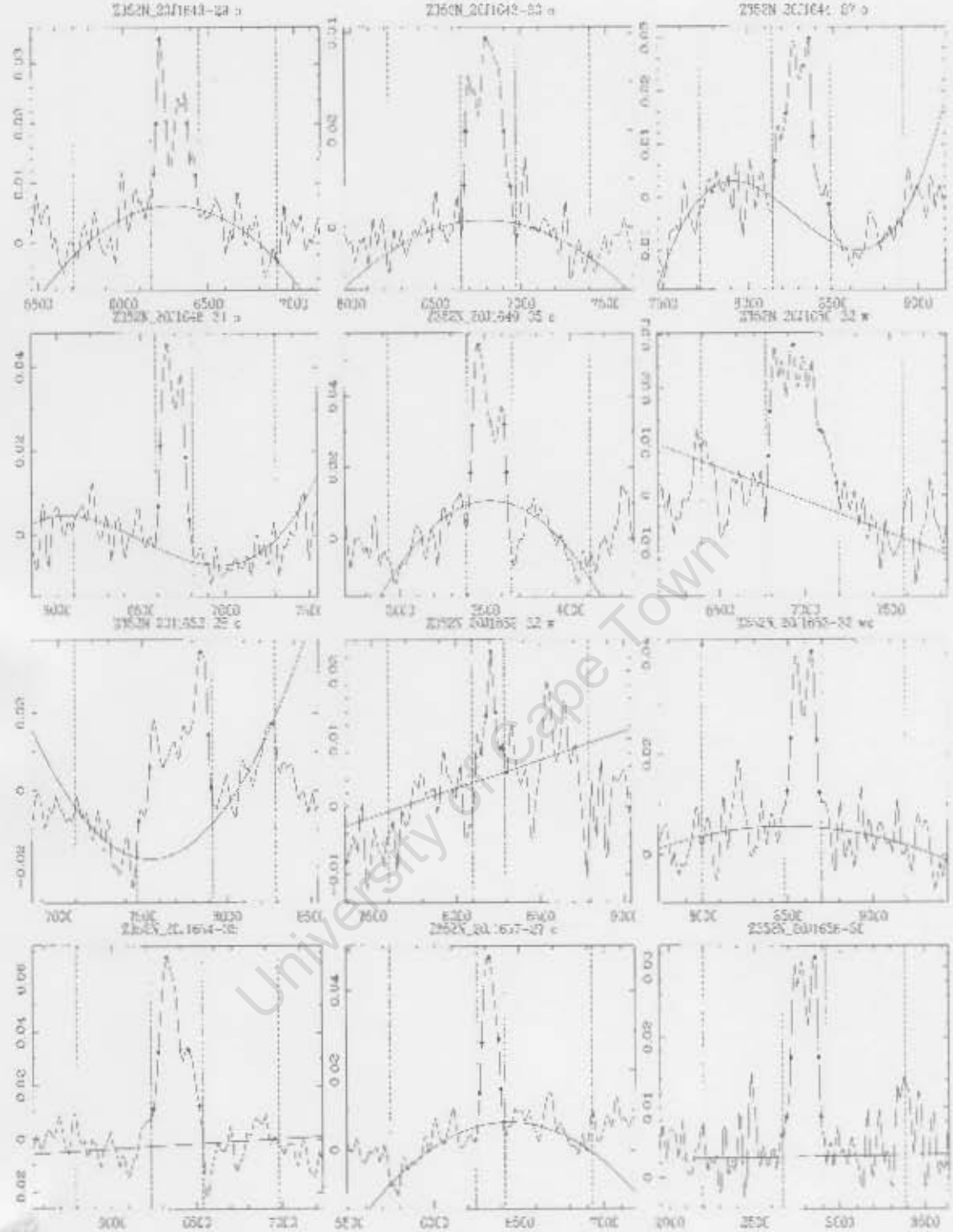

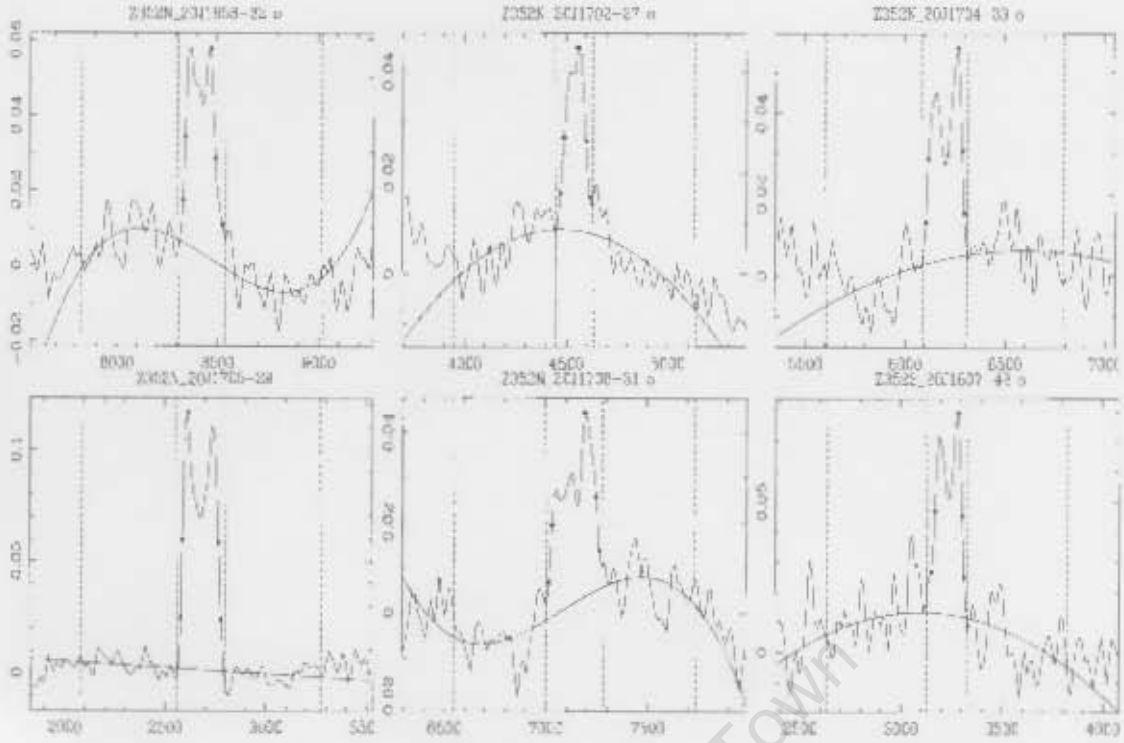

Bibliography

Barnes, D., Staveley-Smith, L., de Blok, W., Oosterloo, T., et al. 2001, MNRAS, 322, 486

Bennett, C. L., Halpern, M., Hinshaw, G., Jarosik, N., et al. 2003, ApJ, 148

Böhringer, H., Schuecker, P., Guzzo, L., Collins, C. A., et al. 2001, A&A, 369, 826

Böhringer, H., Schuecker, P., Komossa, S., Retzlaff, J., et al. 2000, ApJS, 129, 435

Carignan, C. 1999, PASA, 16, 18

Chamaraux, P., Cayatte, V., Balkowski, C., & Fontanelli, P. 1990, A&A, 229, 340

Donley, J., Staveley-Smith, L., Kraan-Korteweg, R., Islas-Islas, J., et al. 2005, AJ, 129, 220

Dressler, A., Faber, S., Burstein, D., Davis, R., et al. 1987, ApJ, 313, 37

Ebeling, H., Edge, A., Allen, S., Crawford, C., et al. 2000, MNRAS, 318, 333

Ebeling, H., Mullis, C. R., & Tully, R. B. 2002, ApJ, 580, 774

Epchtein, N. 1997, in The Impact of Large Scale Near-Infrared Surveys, ed. F. Garzon, N. Epchtein, A. Omont, B. Burton, & P. Persi, Dordrecht: Kluwer, 15

Erdogdu, P., Lahav, O., Huchra, J. P., & Colless, M. Cutri, R. 2006, MNRAS, 373

Ewen, H., & Purcell, E. 1951, Nature, 168, 356

Faber, S., & Burstein, D. 1988, Large-Scale Motions in the Universe, ed. V. Rubin & G. Coyane (Princeton: Princeton Univ), 15

Fairall, A. 1998, Large-Scale Structures in the Universe (New York, Wiley)

Fisher, K., Lahav, O., Hoffman, Y., Lynden-Bell, D., & Zaroubi, S. 1995, MNRAS, 272, 885

Gooch, R. 1996, in Astronomical Data Analysis Software and Systems V, ed. G. Jacoby & J. Barnes, ASP Conf. Ser. 101, 80

Henning, P., Kraan-Korteweg, R., Rivers, A., Loan, A., et al. 1998, AJ, 115, 584

Henning, P., Kraan-Korteweg, R., & Staveley-Smith, L. 2005, in ASP Conf. Ser., Vol. 329, Nearby Large-Scale Structures and the Zone of Avoidance, ed. A. Fairall & P. Woudt, 199

Herschel, J. 1864, ADS, 151

Hey, J. 1971, The Radio Universe (Pergamon: Oxford . Newyork)

Hodapp, K.-W., Hora, J., Hall, D., Cowie, L., et al. 1996, New Astronomy, 1

Hubble, E. 1936, The Realm of Nebulae (New Haven: Yale Univ. Press)

Hundson, M., Smith, R., Lucey, J., & Branchini, E. 2004, MNRAS, 352, 61

Jarrett, T. 2004, PASA, 21, 396

Jarrett, T.-H., Chester, T., Cutri, R., Schneider, S., et al. 2000a, AJ, 120, 298

. 2000b, AJ, 119, 2498

Johnston, M. D., Bradt, H. V., Doxsey, R. E., Margon, B., et al. 1981, ApJ, 45, 799

Kerr, F., & Henning, P. 1987, ApJ, 320, 99

Kerr, F., & Hindman, J. 1953, AJ, 58, 218

Kilborn, V. 2001, PhD thesis, University of Melbourne

Kocevski, D., & Ebeling, H. 2006, ApJ, 645

Kogut, A., Banday, A., Bennett, C. L., Goerski, K. M., et al. 1996, ApJ, 464, 29

Kogut, A., Lineweaver, C., Smoot, G., Bennett, C. L., & Banday, A. 1993, ApJ, 419, 1

Kolatt, T., Dekel, A., Ganon, G., & Willick, J. 1996, ApJ, 458, 419

Koribalski, B., Staveley-Smith, L., Kilborn, V., et al. 2004, AJ, 128, 16

Kraan-Korteweg, R. 2005, ArXiv Astrophysics e-prints

Kraan-Korteweg, R., Cayatte, V., Fairall, A., et al. 1994a, in ASP Conf. Ser. 67, 99

Kraan-Korteweg, R., & Jarrett, T. 2005, in Nearby large-scale structures and the Zone of Avoidance, ed. A. Fairall & P. Woudt, ASP Conf.Ser. 329, 119

Kraan-Korteweg, R., & Lahav, O. 2000, A&ARv, 10, 211

Kraan-Korteweg, R., Loan, A., Burton, W., Lahav, O., et al. 1994b, Nature, 372, 77

- . 1994b, Nature, 72, 77

Kraan-Korteweg, R., Schröder, A., Mamon, G., & Ruphy, S. 1998, in The Impact of Near-Infrared Surveys on Galactic and Extragalactic Astronomy, ed. N. Epchtein, 205

Kraan-Korteweg, R. C. 2000, A&ASS, 141, 123

Kraan-Korteweg, R. C., Woudt, P. A., Cayatte, V., Fairall, A. P., et al. 1996, Nature, 379, 519

Lahav, O. 1994, in Unveiling Large-Scale Structure behind the Milky Way, ed. C. Balkowski & R. Kraan-Koretewg, ASP Conf. Ser. 67, 7

Lauberts, A. 1982, ESO/Uppsala survey of the ESO(B) atlas (Garching: European Southern Observatory (ESO))

Lynden-Bell, D., Faber, S. M., Burstein, D., Davies, R. L., et al. 1988, ApJ, 326, 19

Meyer, M., Zwaan, M., Webster, R., et al. 2004, MNRAS, 350, 1195

Mitronova, S., Karachentsev, I., Karachentseva, V., Jarrett, T., & Kudrya, Y. N. 2004, Bull. Spec. Astrophys. Obs., 57, 5

Nagayama, T., Nagashima, C., & Nakajima, Y. 2003, SPIE, 4841, 459

Nakanishi, K., Takata, T., Yamada, T., Takeuchi, T., et al. 1997, ApJS, 112, 245

Putman, M., de Heij, V., Staveley-Smith, L., et al. 2002, AJ, 123, 873

Raychaudhury, S. 1989, Nat, 342

Rivers, A. 2000, PhD thesis, University of New Mexico

Roman, A. T., Nakanishi, K., & Saito, M. 1998, PASJ, 50, 37

Sault, R., Teuben, P., & Wright, M. 1995, in Astronomical Data Analysis Software and Systems IV, ed. R. Shaw, H. Payne, & J. Hayes, ASP Conf. Ser. 77, 433

Saunders, W., D'Mellow, K., Valentine, H., Tully, R., et al. 2000a, in Mapping the Hidden Universe: The Universe behind the Mily Way - The Universe in HI, ed. R. Kraan-Korteweg, P. Henning, & H. Andernach, ASP Conf. Ser. 218, 141

Schlegel, D., Finkbeiner, D., & Davis, M. 1998, ApJ, 500, 525

Schröder, A., Kraan-Korteweg, R., Mamon, G., & Ruphy, S. 1997, in XVIIth Moriond Astrophysics Meeting on Extragalactic Astronomy in the Infrared, ed. G. Mamon, T. Thuan, & T. T. Van., 381

Shostak, G. 1978, A&A, 68, 321

Staveley-Smith, L., Juraszek, S., Koribalski, B., Ekers, R. D., et al. 1998, AJ, 116, 2717

Strauss, M., Huchra, J., Davis, M., Yahil, A., et al. 1992, ApJS, 82, 29

Strauss, M., Sutherland, W., Maddox, S., Keeble, O., et al. 2000b, MNRAS, 317

Takata, T., Yamada, T., & Saito, M. 1996, ApJ, 457, 693

Tonry, J., Blakeslee, J., Ajhar, E., & Dressler, A. 2000, ApJ, 530, 625

Tully, R. B.and Shaya, E. J., & Pierce, M. J. 1992, ApJS, 80, 479

Tully, R. 2007, astro-ph/0708.2449

Tully, R., & Fisher, J. 1987, Nearby Galaxies Atlas (Cambridge Univ.Press)

Wakamatsu, K., Hasegawa, T., & Karoji, H. 1994, in Unveiling Large-Scale Structures behind the Milky Way, ASP Conf. Ser. 67, 131

Wakamatsu, K., Malkan, M., Nishida, M., & Pareker, Q. . o. 2005, in ASP Conf. Ser., Vol. 329, Nearby large-scale structures and the Zone of Avoidance, ed. A. Fairall & P. Woudt, 189

Wakamatsu, K., Malkan, M., Parcker, Q., & Karoji, H. 2000, in Mapping the Hidden Universe, ed. R. Kraan-Korteweg, P. Henning, & H. Andernach, ASP Conf. Ser. 218, 187

Wakamatsu, K., & Malkan, M. A. 1981, PASJ, 33, 57

Watanabe, M., Yamashita, K., Furuzawa, A., Kunieda, H., & Tawara, Y. 2001, PASJ, 53, 605

Weinberger, R., Gajdosik, M., & Zanin, C. 1999, A&ASS, 137, 293

Whiting, M. 2007, Source Detection with Duchamp, Australia Telescope National Facility

Wong, O. I., Ryan-Weber, E. V., Garcia-Appadoo, D. A., Webster, R. L., et al. 2006, MNRAS, 371, 1855

Woudt, P. 1998, PhD thesis, University of Cape Town